DESIGN OF A MINIATURE OPTICAL-BASED VELOCITY PROBE

by

Jacob Butterworth

A thesis submitted to the faculty of
The University of Utah
in partial fulfillment of the requirements for the degree of

Master of Science

Department of Mechanical Engineering

The University of Utah

May 2011

The University of Utah Graduate School

STATEMENT OF THESIS APPROVAL

The thesis of **Jacob Butterworth**

has been approved by the following supervisory committee members:

Meredith Metzger	, Chair	**12/2/2010** Date Approved
Robert Stoll	, Member	**12/2/2010** Date Approved
Patrick McMurtry	, Member	**12/2/2010** Date Approved

and by **Timothy Ameel**, Chair of the Department of **Mechanical Engineering**

and by Charles A. Wight, Dean of The Graduate School.

ABSTRACT

Anemometry is the measurement of wind force and velocity. Though anemometry technology is fairly well developed, many velocity measurement devices are expensive, large, and/or fragile. Due to these limitations, deploying large numbers of anemometers is difficult, and often unrealistic. The miniature optical-based velocity probe is a new instrument that offers advantages over current state-of-the-art anemometers in terms of lower expense, lower power consumption and lighter weight. The probe consists of a high performance plastic optical fiber, a vertical-cavity surface-emitting laser (VCSEL), and a position sensitive detector (PSD). Light transmitted by the VCSEL shines through the free end of the optical fiber illuminating the surface of the PSD. A drag force, induced by an approach flow, causes the optical fiber to deflect. The PSD measures the deflection of the optical fiber and outputs an analog voltage, which can be directly related to velocity through a calibration curve. Equations for the deflection and natural frequency of the optical fiber, along with numerical simulations in FLUENT were used to make key design decisions in order to optimize the probe to meet the target specifications for atmospheric research. Preliminary calibration experiments show that the velocity probe has the potential to be a viable replacement for other research-quality anemometers.

CONTENTS

APPENDICES

LIST OF FIGURES

NOMENCLATURE

ℓ	distance along longitudinal axis of fiber
y	deflection of fiber from static equilibrium
y_c	deflection as output from the PSD
t	time
ω_n	natural frequency in rad s^{-1}
f_n	natural frequency in Hz
d	diameter of fiber
d_b	diameter of the hypodermic tubing
L	length of fiber
L_b	length of the hypodermic tubing
g	gap size between free-end of fiber and face of PSD chip
m	mass of exposed fiber
k	stiffness characteristic of fiber
E	modulus of elasticity of fiber
I	area moment of inertia of fiber, $I = \frac{1}{4}\pi\,(d/2)^4$
A	cross-sectional area of fiber, $A = \pi\,(d/2)^2$
ρ	density of fiber
ρ_a	density of air
μ	absolute viscosity of air
U_∞	approach flow speed
U_j	velocity at slot jet calibration facility exit
f	force per unit length acting on fiber
f_s	vortex shedding frequency
C_d	drag coefficient, $C_d = F_d/(1/2\,\rho_a\,U_\infty^2\,d\,\ell)$
Re	Reynolds number for cylinder, $Re = \rho_a\,U_\infty\,d/\mu$
Re_x	Reynolds number for flat plate, $Re = \rho_a\,U_\infty\,x/\mu$
St	Strouhal Number, $St = f_s\,d/U_\infty$
δ	logarithmic decrement
δ_{BL}	Blasius boundary layer thickness, $\delta_{BL} = 0.382\,x\,Re_x^{-1/5}$

ACKNOWLEDGEMENTS

Financial support for this work was provided by the University of Utah Research Foundation through the Technology Commericialization Project program. The author would like to thank Dr. Andras Pungor who designed the electronics circuit board for the sensor.

A special thanks to Prof. Metzger for being my advisor for the project and providing invaluable insight and direction. Also thanks to my wife Stefeni for her patience and support as I worked on this project.

CHAPTER 1

INTRODUCTION

Anemometry is the measurement of wind force and velocity. An anemometer is an instrument used to measure one or more components of wind velocity at a single point in the flow. Though anemometry technology is fairly well developed, many velocity measurement devices are expensive, large and fragile. Due to these limitations, deploying large numbers of anemometers in field campaigns to study atmospheric turbulence is difficult, expensive and often unrealistic. The velocity probe presented in this paper is designed to overcome these limitations, while maintaining relatively high spatiotemporal resolution. Table 1.1 shows three readily available anemometers in the market today. The miniature optical-based velocity probe described herein is a new instrument specifically designed to bridge the gap between the sonic and hot-wire anemometers in terms of measurement volume (spatial resolution) and frequency response. Importantly, the velocity probe will also be inexpensive, lightweight, energy efficient and easily deployable in larger numbers. Being especially designed for atmospheric turbulence measurements, the probe can be used in many different environmental scenarios. For example, it can be suspended from pilot balloons, mounted on unmanned aerial vehicles, placed on

Table 1.1. Comparison between a few different anemometers

Type	Measurement Volume (cm^3)	Frequency Response (Hz)
Pitot-static[1]	0.64×0.64×2.54	10
Sonic[2]	10.3×6.0×6.0	10–50
Hot-wire[3]	0.1×0.1×0.0005	10000

[1] Dwyer 167–6 tube with MKS Baratron 698 Pressure Transducer
[2] Campbell Scientific, CSAT3
[3] Dantec Dynamics, CTA system with 55P01 probe

towers, or any other stable platform. Note, the ideas underlying the principle of operation of the velocity probe and its intended utilities have already been patented (Metzger & King, 2010). A patent search was a necessary part of that patent application process, the results of which are discussed in the next section.

1.1 US Patent Search

Many sensors and devices have been developed to measure fluid flow parameters and conditions. The methods used are varied and have different advantages depending on the particular fluid flows. Table 1.2 lists the most relevant devices as found during a recent patent search. A brief description of each device is given below.

The *clear air turbulence detector* (Hara, 1980) detects clear air turbulence through the collection and analyses of back-scattered laser light from a region where clear air turbulence may exist. The interference pattern is determined through an ultra high-resolution spectroscope and analyzed with an image dissector. The spectrum of back-scattered light is correlated with a spectrum representing the absence of clear air turbulence. This instrument detects distance, direction and intensity of clear air turbulence.

The *gas velocity meter* (Hartmann & Siersch, 1980) measures the mean flow velocity inside a duct. The meter generates two light beams in the form of shallow wide bands, which traverse the duct across two transverse planes arranged at right angles to the mean flow direction. The two light beams emerge from the duct and are received on respective photoelectric detectors. The output signals of the photoelectric detectors have a small difference due to the time required for the gas to flow between the two planes. The difference in time is correlated through a circuit and an output proportional to the mean flow velocity of the gas is generated.

In a *laser-doppler-anemometer* (John & Olldag, 1986) two frequency-displaced partial beams are transmitted to a measuring probe. The probe is fixed at a distance away from the laser source. The two beams are focused on each other and the probe detects the light. As particles pass through the light beams they reflect scattered

Table 1.2. List of reviewed patents

Issue Date	Patent Number	U.S. Patent Title	Inventor Name
04/01/1980	4195931	Clear air turbulence detector	Small
05/06/1980	4201467	Gas velocity meter	Hartmann, et al.
05/11/1986	4575238	Laser-doppler anemometer	Knuhsten, et al.
11/11/1986	4621929	Fiber optic thermal anemometer	Phillips
12/30/1986	4631958	Force-balance drag anemometer	Van Cauwenberghe, et, al.
01/20/1987	4637716	Fiber-optical Doppler anemometer	Auweter, et al.
05/05/1987	4662749	Fiber optic probe and system for particle size and velocity measurement	Hatton, et al.
04/04/1989	4818071	Fiber optic doppler anemometer	Dyott
04/02/1991	500493	Remote measurement of physical variables with fiber optic systems - methods, materials and devices	Kleinerman
06/11/1991	5023845	Embedded fiber optic beam displacemnt sensor	Crane, et al.
05/19/1992	5115127	Optical fiber sensor for measuring physical properties of fluids	Bobb, et al.
06/09/1992	5120951	Optoelectronic motion and fluid sensor with resilient member deflected by fluid flow	Small
01/30/1996	5488224	System for characterizeing flow pattern, pressure and movement of a fluid	Fagan, et al.
06/10/1997	5638174	Fluid sensing apparatus with a rotatable member utilizing different length light pipes for alternately transmitting a light beam	Henderson
02/02/1999	5865871	Laser-based forward scatter liquid flow meter	Simundich
12/26/2000	6166806	Fiber optic catheter for accurate flow measurements	Tjin
01/28/2003 04/05/2005	6510842 6874480	Flow meter	Ismailov
01/25/2005	6847437	Laser anemometer	Bruel, et al.

light into the photo detector. The Doppler frequency shift of the scattered light is then used to calculate the velocity of the particles in the fluid, which corresponds to the velocity of the fluid.

A *fiber optic thermal anemometer* (Phillips, 1986) can be used to measure the heat transfer coefficient of a fluid sample. An element with temperature sensitive optical properties is placed in contact with a fluid sample. The element is heated or cooled to an equilibrium temperature. The rate of heating or cooling and the temperature difference between the element and the fluid sample indicate the heat transfer coefficient. The heat transfer coefficient of the fluid sample is also a product of its composition and other physical properties. This optical method can detect the composition of gasses, liquids, fluid levels, and the presence of bubbles in a liquid. It can also detect the pressure and flow rates of the fluid.

The *force-balance drag anemometer* (Cauwenberghe & Motycka, 1986) can be used to measure two orthogonal velocity components of a fluid. The anemometer consists of a sphere attached to a shaft. The drag force acting on the sphere causes the shaft to deflect from its neutral position. The deflection can be measured using optical or electrical sensors. The sensors control an electromagnetic actuator, which generates a force opposing the drag force. The actuator returns the shaft to its neutral position. The force is measured and related to the velocity of the fluid using a coefficient of drag versus Reynolds number curve.

The *fiber-optical Doppler anemometer* (Auweter *et al.*, 1987) uses moving particles to reflect incident light into a configuration of two optical fibers. Reflected light, with a frequency different from the incident beam, is coupled with incident light and received by a photoelectric transducer. The photoelectric transducer records the scatter and the Doppler shift is used to determine the flow velocity.

The *fiber optic probe and system for a particle size and velocity measurement* (Hatton & Plawsky, 1987) is a system that measures the size and velocity of bubbles or drops in a multiphase process environment. The probe consists of a transmitting coherent fiber bundle, a lens for projecting the transferred fringe image into a measurement zone within the fluid, and receiving fiber optic bundles that have a

distal end lens for collecting the light reflected or refracted from the bubbles or drops. The probe then transfers received light to a signal processing apparatus and converts the light into an electrical signal corresponding to the phase and amplitude components of the received light The velocity or size of the bubbles or drops are then determined from the data received.

The *fiber optic Doppler anemometer* (Dyott, 1989) uses coherent light, a directional coupler formed by the combination of a pair of single-mode optical fibers and a photoelectric transducer. A light source provides the first optical fiber with an incident beam. The second end of the optical fiber is located adjacent to a body of moving particles. The moving particles reflect a portion of the incident light back into the first fiber with a different frequency than the incident light. The light is directed back through the directional coupler, which directs the light toward the second optical fiber and converts it into electrical signals. Using the Doppler effect the system can measure the velocity of moving particles.

Remote measurement of physical variable with fiber optic systems-methods materials and devices (Kleinerman, 1991) uses a light source to generate a signal beam and a reference beam. The transmission of both beams through a single multi-mode optical fiber to a single photo detector produces photoelectric signals. These signals can sense variations in the magnitude of a physical parameter. Properties such as forces applied to the optical fiber, measurement changes in light intensity and velocity can be measured with these methods.

The *embedded fiber optic beam displacement sensor* (Crane & Fischer, 1991) measures two-dimensional displacements of a sample material. Embedding an optical fiber into an object allows for detection of its displacement with a photo-detector grid array. Light is transmitted through the optical fiber and emerges from an open end. The photo-detector will detect object's movement. Forces acting on the object can be determined by how much it moves or deflects.

The *optical fiber sensor for measuring physical properties of fluids* (Bobb *et al.*, 1992) uses a fiber optic cable coated in a conductive material, usually gold, which is placed into a fluid. Electrical energy is applied to the conductive material to heat

a region of the fiber. Heating the optical fiber changes the path of the light inside the fiber. A physical property is determined from the changes in the optical path length or phase of the light received at the end of the optical fiber. Measuring the phase change and applied electrical energy from heating a fiber to an equilibrium temperature provides a means of finding the flow rate of a fluid.

The *optoelectronic motion and fluid flow sensor* (Small, 1992) uses a light source and a photo-sensor placed on opposite sides of a fluid flow passageway. A resilient or elastic member is placed in the flow, which varies the amount of light incident on the photo-sensor from the light source. The member can be any number of things, including an optical fiber. As the fluid flows past the member, viscous and pressure forces act on it, causing it to deflect or move. This change causes the light incident on the photo-sensor to change. The change can then be related to the velocity or flow rate of the fluid.

The *system for characterizing flow pattern, pressure and movement of a fluid* (Fagan *et al.*, 1996) characterizes properties of the fluid under high pressure in a test cell. Adjustable rock facings line the interior of the test cell. Pressure is measured using a device with pressure-distortable optical fibers. The fluids velocity including direction is measured with laser Doppler velocimetry. The flow pattern is also viewed using arrays of optical fibers.

The *fluid sensing apparatus with a rotatable member* (Henderson, 1997) is capable of determining fluid flow rates, density, particulate content, light transmittance, spectral attributes and other fluid characteristics. The apparatus alternates two different light beams emerging from light pipes of two different lengths. The fluid flows into the rotating member. As the member rotates, due to the moving fluid, the light pipes will alternately align with the emitter and detector. The frequency at which the lights change can be related to the flow rate. Because the two light pipes are different lengths, other fluid properties can be determined as well. The change in the gap between the end of the light pipe and the detector allow for the detection of other properties such as density or particulate content.

The *laser-based forward scatter liquid flow meter* (Simundich, 1999) measures

the effect of a flow on a laser beam traveling through the flow to a detector. The flow interferes with the laser causing the laser beam to refract. These refractions cause variations in the lasers energy strength at audio and super audio frequencies. The flow rate is proportional to the audio frequency correlated with known flow rates for the particular fluid.

The *fiber optic catheter for accurate flow measurements* (Tjin, 2000) can perform accurate measurements of fluids flowing within pipes, veins, or arteries. The catheter uses two optical fibers. A reflective surface intercepts light transmitted by the first fiber and reflects the light through an optically transparent window and into the fluid. Some of the light returns as backscatter and is reflected into the terminal ends of the second fiber. The scattered light is collected and transmitted to an anemometer. The velocity of the fluid is determined by analyzing the Doppler shift between the transmitted light and the scattered light.

The *flow meters* (Ismailov, 2003, 2005) use a laser Doppler anemometer to measure the instantaneous centerline velocity of fluid flow in a pipe. It also uses the velocity to compute the volumetric flow rate, mass rate and other flow characteristics. The electronic processing method is used to obtain an exact solution to the Navier-Stokes equations for periodically oscillating flow. These flow meters are specifically designed to measure flow characteristics of high-pressure automotive fuel injection systems. A laser light source is split in to two beams, which intersect the fluid flow. A photo detector is used to detect forward scatter caused by the light's interaction with the fluid. The Doppler frequency shift is converted into instantaneous velocity.

A *laser anemometer* (Bruel & Combe, 2005) measures the relative velocity between the anemometer and a fluid medium. A laser beam is focused in a measurement zone containing particles. The particles create backscattered radiation from the laser, which is collected by an optical mixer that measures the Doppler shift between the emitted laser and the backscatter from the particles. The shift is related to the relative velocity between the laser anemometer and the particles in the fluid.

1.2 Outline of Thesis

The miniature optical-based velocity probe (MOBV) is a small, inexpensive sensor for measuring wind speed and small-scale turbulence. It operates on the principle of drag-force (DeLucia & Manfrida, 1989; Fralick, 1980; Krause & Fralick, 1982). A small cantilever beam protrudes into the flow. The protruding beam deflects due to the drag force induced by the approach flow. The drag force is determined through the measurement of the deflection of the beam. The approach flow velocity can then be determined through a calibration curve. Much like the embedded fiber optic beam displacement sensor described above, the velocity probe uses optical fiber technology to measure the beam deflection. In this case, the cantilever beam is the fiber optic cable. The fiber deflects due to drag forces created by an approach flow and transmits its position to a position sensitive detector (PSD).

The current design has several limitations. Because a one-dimensional PSD is used to measure the deflection of the optical fiber, the velocity probe can only measure the velocity and its fluctuations in one direction. In addition, the frequency response of the probe largely depends on the choice of optical fiber characteristics. The current design has a frequency response of about 210 Hz, meaning that this particular sensor will not detect turbulent motions with frequencies higher than 210 Hz.

The previous thesis of Swope (2009) described the initial concept underlying of the present velocity probe and characterized several early-generation prototypes. However, Swope utilized an ad hoc design process. The contribution of this thesis lies in its focus on a theory-based design approach. In addition, a battery-powered working prototype was successfully built. The outline of this thesis is as follows. First, the target design specifications and principle of operation are stated. The design methodology, including design equations, sensitivity, and uncertainty analysis, optical fiber selection is presented. Results from numerical simulations of the flow around the aerodynamic shell, velocity profiles in the region of the optical fiber, and basic fluid-structure interaction behavior are discussed. All simulations were

performed in FLUENT. Calibration results are presented, indicating consistency and repeatability of the velocity measurements. Finally, the spectral response of the velocity probe and its ability to accurately capture turbulence is compared to that of a hot-wire anemometer through bench top experiments using a slotted jet.

CHAPTER 2

VELOCITY PROBE DESIGN

2.1 Target Design Specifications

The current-generation velocity sensor has been designed according to the target specifications listed in Table 2.1. Note, successfully achieving these target specifications would yield a velocity sensor that bridges the gap between commercially available sonic and hot-wire anemometers in terms of spatiotemporal resolution, thus fulfilling a need in the atmospheric sciences community allowing for more cost-affordable, yet sophisticated, large-scale field campaigns. Note, the specified velocity range is typical of rear-surface atmospheric wind conditions and is also within the operating range of the test facility used to calibrate the velocity probe. Limitations in the state-of-the-art PSD technology precluded the current-generation velocity sensor from attaining all of the desired characteristics, as listed in Table 2.1. Nevertheless, very good progress was made in this direction in all categories. Specific design strategies, constraints and outcomes are discussed in detail below.

Table 2.1. Target specifications for the velocity probe

Characteristic	Desired Value
Frequency Response	500 – 1000 (Hz)
Velocity Range	0.5 – 12 (m/s)
Uncertainty	±5 cm/s
Spatial Resolution	10 mm
Power Consumption	5 mW
Weight (with battery)	100 g
Package Size	Hand-held

2.2 Principle of Operation

The velocity probe operates upon the principles of simple cantilever beam deflection and aerodynamic drag over a cylinder. Figure 2.1 shows a representative schematic, including relevant geometric parameters, of the application of these principles. Aerodynamic drag from the incoming fluid flow causes the free-end of a cantilevered optical fiber (diameter d, length L) to deflect. A light source illuminates the anchored end of the fiber and shines through to its free-end. A one-dimensional position sensitive detector (PSD), mounted on a post opposite the optical fiber, detects the position (y_c) of a spotlight created by the light shining out of the free-end of the fiber. A small gap (length g) separates the PSD from the free-end of the fiber. As the optical fiber deflects due to changes in the fluid flow velocity, the PSD outputs the spotlight's change in position. Applying a characteristic mathematical model to the output of the PSD allows for a fast and accurate calculation of the velocity of the incoming fluid flow.

2.3 Design Methodology

The design strategy described below outlines the rationale used in selecting the fiber (type, diameter, length), PSD chip (model S4583–04), and light source.

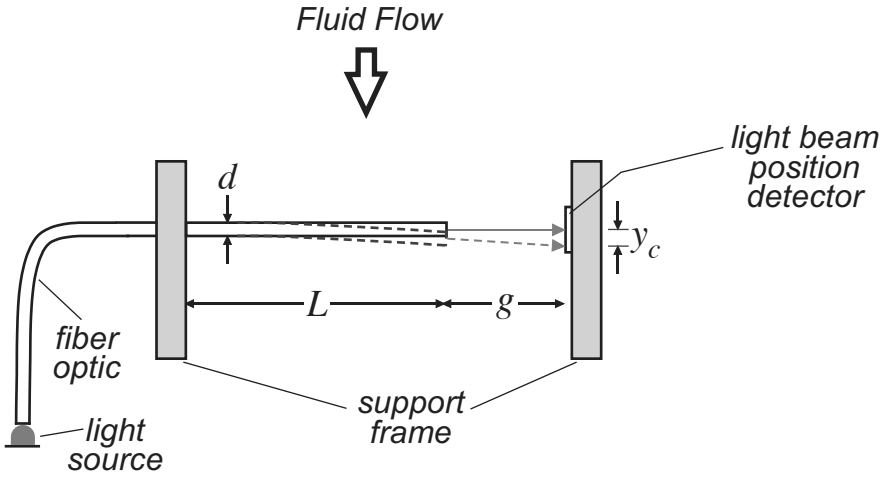

Figure 2.1. Schematic displaying the basic principle operation of the velocity probe. The dashed lines represent the deformed position created by the incoming fluid flow.

The most critical of these is the fiber, since it governs the overall response of the sensor to changes in the approach flow. Selection of the PSD chip depends on the fiber used, because the fiber determines the expected maximum deflection, which sets the required full-scale range of the PSD. In addition, the PSD dictates the overall uncertainty in the subsequent velocity measurements acquired from the probe. Finally, the selection of the light source depends on the type of fiber selected as well as the radiant energy requirements of the incident spotlight on the PSD chip.

2.3.1 PSD Chip

One of the primary constraints in the sensor design is the PSD chip itself. A low profile, compact PSD chip was necessary in order to reduce the overall size of the velocity sensor, thus guaranteeing the desired spatial resolution. The two most important characteristics of the PSD are the range (specified by the active area of the chip) and the uncertainty. The current-generation velocity sensor utilizes a one-dimensional PSD (Hamamatsue* S4583–04) with a range of 3 mm (in the flow direction) and uncertainty of $\pm$ 10 μm. This effectively yields an uncertainty of 0.67% at full-scale, which arguably for research purposes is only marginally acceptable. The rise time of the PSD, i.e., the time required for the output to change from 10% to 90% of the steady output value for a step-input measures 10 μs, which is high enough to allow the sensor to respond to even the fastest turbulent fluctuations expected in the atmosphere. The PSD outputs an analog voltage signal proportional to the centroid of the spotlight.

There are several other viable options of one-dimensional PSDs, besides the model S4583-04 selected here, with ranges between 2 mm and 6 mm. Importantly though, the 3mm PSD selected has the best compromise between range and absolute uncertainty. In fact, at present, there are no other PSDs available on the market to the author's knowledge, with an uncertainty less than $\pm$ 10 μm. The PSDs with a range lower than 3 mm have an equivalent uncertainty; while those with higher ranges have larger uncertainty. Alternatively, a two-dimensional PSD would

*The leading manufacturer of PSD technology in terms of quality and variety, is Hamamatsu

provide measurements of two velocity components with out any additional change in the aerodynamic shell of the velocity probe. However, the absolute error of two-dimensional PSDs remains twice that of one-dimensional PSDs. Because a twofold decrease in accuracy was deemed unacceptable for the target research application, the present velocity probe was designed for a single, one-dimensional PSD. The spectral response range of the PSD lies between 760 nm to 1100 nm with a peak sensitivity wavelength of 960 nm.

2.3.2 Light Source

As it turns out, the PSD chip used in the present application produces accurate position data independent of incident light intensity. Swope (2009) performed a light intensity test revealing that changes in intensity had little affect on the PSD output. The only exception that yielded a large change in the PSD output occurred when the intensity became too high causing the PSD to saturate. One goal of the present velocity probe, compared to earlier design of Swope (2009), was to avoid the need for a costly optical coupler between the fiber and the light source. After investigating several options including various LEDs and laser diodes, a vertical cavity surface emitting laser (VCSEL) was chosen (Optek model OPV322). The VCSEL is specifically designed for noncontact position sensing, making it ideal for this application. The VCSEL also has a wavelength (850 nm) well within the spectral range of the PSD. The three main attractive features, through, are: (i) low power consumption (ii) small size, 3.5 mm long and 1.6 mm diameter, and (iii) narrow light beam, 6° divergence angle. The latter is achieved by a dome lens incorporated into the packaging of the VCSEL. The narrow beam angle combined with the small diameter of the emitted light beam, eliminate the necessity of an optical coupler. Simply butting the clamped end of the fiber against the dome lens of the VCSEL was sufficient enough for purposes of this application.

2.3.3 Mathematical Models

A mathematic model of the system shown in Figure 2.1, along with previous experimental data provided by Swope (2009), was used to design the fiber for the

current-generation velocity probe using a theory-based approach. In essence, the model provides predictions of the beam position, y_c and the natural frequency, ω_n as a function of both the geometric and material properties of the fiber. Derivations based on simple cantilever beam deflection model are outlined in the Appendix. The resultant equations are,

$$y_c = \frac{C_d\,\rho_a\,d\,U_\infty^2\,L^4}{16\,E\,I}\left[1+\frac{4\,g}{3\,L}\right], \tag{2.1}$$

and

$$\omega_n = \frac{1.875^2}{L^2}\sqrt{\frac{E\,I}{\rho\,A}}, \tag{2.2}$$

where C_d is the coefficient of drag, ρ_a is the density of the air, U_∞ is the approach flow velocity, E is Youngs Modulus of the fiber, I is the area moment of Inertia, and A is the cross sectional area of the fiber. In order to evaluate y_c over a range of input parameters, an empirical relationship between C_d and Re is necessary.

Prior experimental data in the form of y_c versus U_∞, used for this purpose, is displayed in Figure 2.2. Equation 2.1 may be rearranged to give

$$C_d = \frac{16\,E\,I\,y_c}{\rho_a\,d\,U_\infty^2\,L^4}\left[1+\frac{4\,g}{3\,L}\right]^{-1}. \tag{2.3}$$

Substituting the experimental data of Figure 2.2 into (2.3) along with the appropriate parameter values for Swope's sensor, allowed C_d to be plotted versus Re, as displayed in Figure 2.2. Also shown for comparison are data for flow over an infinite cylinder. Data from the sensor are generally two to three times higher than that for an infinite cylinder. MATLAB was used to determine equations for a best fit line through the data points. C_d versus Re obeys the empirical relationship $C_d = 10.495(Re^{-0.3371})$. This regression line was then used to calculate C_d over a range of 1 m/s to 8 m/s for different parameter values in the present design. Values for y_c and ω_n were found for combinations of the three design variables: L, d, and E. This method allowed fast, direct comparison between different optical fiber types, and sizes.

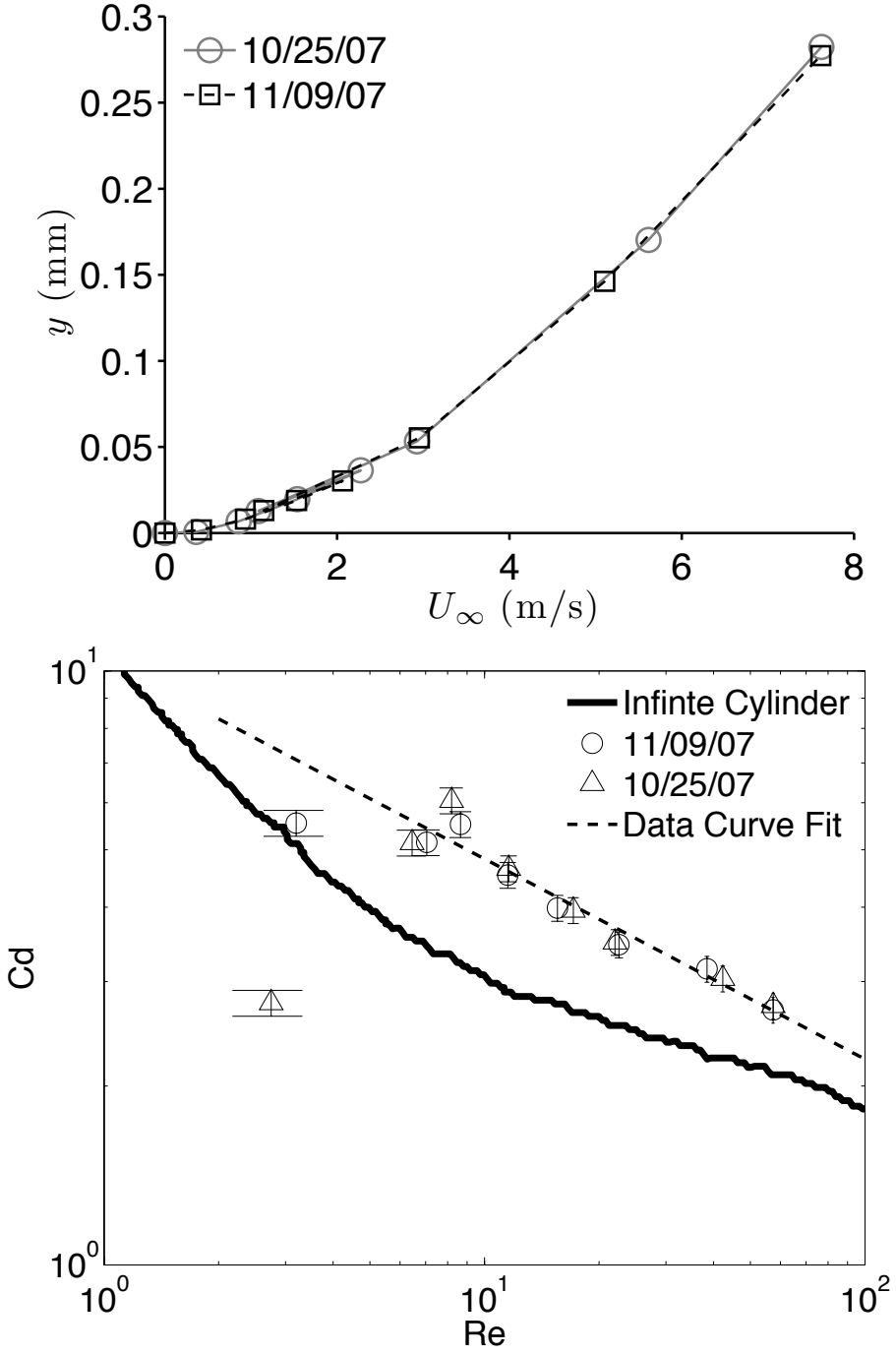

Figure 2.2. Experimental data provided by Swope (2009) (top) and the drag coefficient of an optical fiber compared to the drag coefficient of a circular cylinder as functions of Reynolds number (bottom). The solid line is data taken from Schlichting (1979).

2.3.4 Sensitivity Analysis

Using equations (2.1) and (2.2) to both make design decisions and analyze data requires an understanding of the how sensitive y_c and ω_n are to the various parameters, and how uncertainty in the values of the parameters propagates through the equations. Sensitivity analysis quantifies the effect of small perturbations in the design parameters on the subsequent value of the output. A Taylor series approximation of equation (2.1) (details of which are provided in the Appendix) was used to calculate the sensitivity of y_c, denoted by Δ_{y_c}. The resultant expression is

$$\Delta_{y_c} = \frac{y_c}{C_d}\,\Delta_{C_d} + \frac{y_c}{\rho_a}\,\Delta_{\rho_a} - 3\frac{y_c}{d}\,\Delta_d + 2\frac{y_c}{U_\infty}\,\Delta_{U_\infty} + \left(12\frac{L+g}{3L+4g}\right)\frac{y_c}{L}\,\Delta_L + \left(4\frac{g}{3L+4g}\right)\frac{y_c}{g}\,\Delta_g - \frac{y_c}{E}\Delta_E. \quad (2.4)$$

The coefficient in front of each variable is proportional to the sensitivity of the output to that particular variable, i.e., the higher the coefficient, the more sensitive y_c is to that variable. A close examination of equation (2.4) reveals that the variables with the highest coefficients are: length L, diameter d, and velocity U_∞. The values of the coefficients are 16, 9, and 4, respectively (assuming $g \approx 0$). Being sensitive to small changes in velocity makes it possible to detect turbulence in the flow, and thus is a desirable feature. On the other hand, high sensitivity of y_c to L and d means that care must be taken in the design, manufacture and assembly processes, because small variations in L could dramatically impact the expected performance of the probe. In addition the negative signs in (2.4) indicate that an increase in d or E translates into a corresponding decrease in y_c; whereas an increase in all the res of the parameters leasds to an increase in y_c.

A similar analysis was performed on equation (2.2) (details given in the Appendix), to obtain the sensitively of ω_n, denoted by Δ_{ω_n}, and given as

$$\Delta_{\omega_n} = -2\frac{\omega_n}{L}\,\Delta_L + \frac{1}{2}\frac{\omega_n}{E}\,\Delta_E + \frac{\omega_n}{d}\Delta_d + -\frac{1}{2}\frac{\omega_n}{\rho}\,\Delta_\rho. \quad (2.5)$$

As before, the geometric properties of the fiber (i.e., L and d) have the largest coefficients, while the material properties of the fiber (E and ρ) have the smallest

coefficients. Thus, ω_n is highly sensitive to changes in L, and moderately sensitive to changes in d. Again the negative sign reveals that an increase in L leads to a decrease in ω_n and an increase in d leads to an increase in ω_n.

2.3.5 Fiber Selection

The general parameters characterizing optical fibers that can be varied in the present application include: diameter size, material type, and modes. As indicated by the analysis in section 2.3.4, the performance of the velocity probe depends heavily on the geometric properties of the optical fiber, and to a lesser extent the material properties.

As stated earlier, the primary constraints in the sensor design are the range and uncertainty of the PSD chip. The PSD chip possesses a range of 3 mm. However, since the fiber is initially placed in the middle of the chip, under conditions of static equilibrium (no flow), an overall deflection limit of 1.5 mm exists. Therefore, the fiber needs to be designed such that $y_c \leq 1.5$ mm at the highest expected flow speed. In addition, because the PSD possess an absolute uncertainty of ± 0.01 mm, the fiber must also be designed so that $yc \geq 0.01$ mm at the lowest expected flow speed. These criteria set an important design constraint, namely that the fiber should be selected to guarantee 0.01 mm $\leq y_c \leq$1.5 mm over the target velocity range, which is specified as $0.5 - 12$ m/s. The challenge, however, lies in trying to simultaneously achieve the target natural frequency of 1000 rad$\cdot s^{-1}$ The present design approach was to select several different types of commercially available fibers, and then calculate their response, i.e., y_c and ω_n using equations (2.1) and (2.2) for a range of L and U_∞.

Table 2.2 displays a subset of the results generated; a more complete set of design tables can be found in the Appendix. Note, the listed material properties of the fibers such as density ρ and modulus of elasticity E are based on published values from the manufacturer; the listed fiber diameter is that of the core plus the cladding with the insulation stripped. Optimizing both deflection and natural frequency proved to be very difficult. Ideally, the fiber would have a relatively large deflection (y_c) and a large natural frequency (ω_n). However, as mentioned

Table 2.2. Optical fiber options

Fiber Type	Modulus (GPa)	Length (mm)	Diameter (mm)	y_c (mm) U_∞= 1 m/s	y_c (mm) U_∞= 8 m/s	ω_n (rad/s)
Silicone	70	15	0.125	3.11e-3	9.87e-2	2.53e3
Silicone	70	17.5	0.125	5.63e-2	1.69e-1	1.86e3
Silicone	70	20	0.125	9.45e-3	3.00e-1	1.43e3
Silicone	70	17.5	0.245	5.96e-4	1.89e-2	1.43e3
Silicone	70	20	0.245	1.00e-3	3.18e-2	2.79e3
SuperEska	4	15	0.25	5.38e-3	1.71e-1	1.81e3
SuperEska	4	17.5	0.25	9.76e-3	3.10e-1	1.33e3
SuperEska	4	20	0.25	1.64e-2	5.20e-1	1.02e3
SuperEska	4	15	0.5	5.33e-4	1.69e-2	3.61e3
SuperEska	**4**	**17.5**	**0.5**	**9.66e-4**	**3.07e-2**	**2.56e3**
SuperEska	4	20	0.5	1.62e-3	5.14e-2	2.03e3

in Section 2.3.4, both of the design equations are especially sensitive to changes in optical fiber length (L). In fact, an increase in L tends to increase y_c but simultaneously lowers ω_n. Similarly a decrease in diameter (d) will result in an increase in ω_n but a decrease in y_c.

Table 2.2 shows that the SuperEska fiber with a diameter of 0.25mm and a length of $L = 17.5$ mm offers the best compromise. For this fiber, the expected natural frequency is $\omega_n = 1333$ Hz, while the expected deflection is $y_c = 0.00097$ mm at $U_\infty = 1$ m/s and $y_c = 0.31$ mm at $U_\infty = 8$ m/s. Because the uncertainty of the PSD is 0.01mm, additional calculations were performed to refine the fiber length so that y_c at $U_\infty = 1$ m/s at least matched the uncertainty of the PSD. The results from theses calculations are shown in Table 2.3. The final selected fiber length

Table 2.3. Design table used to dertmine optimal length of the SuperEska fiber.

Length (mm)	y_c (mm) at $U_\infty = 1$ m/s	ω_n (rad/s)
17.4	9.54e-3	1.34e3
17.5	9.76e-3	1.33e3
17.6	9.97e-3	1.31e3
17.7	**1.02e-2**	**1.30e3**
17.8	1.04e-2	1.28e3

is $L = 17.7$ mm which yields a natural frequency of $\omega_n = 1300$ rad$\cdot s^{-1}$. Based on the y_c calculations relative to the specified uncertainty of the PSD the selected fiber will only be able to measure velocities greater than 1 m/s. Furthermore, because $\omega_n = 1300$ Hz, the selected fiber will only be capable of responding to turbulent fluctuations with frequencies less than 207 Hz. Clearly the selected fiber falls slightly short of meeting the target frequency response and velocity range specifications given in Table 2.1; however, for this work, the selected fiber is deemed suitable as far as demonstration purposes.

From Table 2.2, one can see that for a given length and diameter the silicone and SuperEska fibers perform similarly. From a practical standpoint, the SuperEska fiber is also much easier to use than the silicone fiber. The diameter of the plastic optical fiber is twice the diameter of the silicone fiber making it easier to line up with the VSCEL laser. The plastic fiber is also easier to handle than the silicone fiber because the silicone fiber is very brittle. There is little to no risk of breaking or damaging the plastic optical fiber while assembling the probe.

In summary, The SuperEska high-performance plastic optical fiber with a cladding diameter of 0.25 mm, a core diameter of 0.24 mm and a length of 17.7 mm was chosen for this velocity probe. It is not brittle, deflects sufficiently over a reasonable velocity range, and effectively transmits the light from the VCSEL. The geometric and physical properties of the optical fiber are displayed in Table 2.4.

Vortex shedding caused by flow over the cylinder could lead to resonance if it coincides with the natural frequency. Resonance causes the fiber to vibrate

Table 2.4. Geometric and material properties of the optical fiber

Quantity	Value	Units
E^*	4 $\pm$0.2	GPa
ρ^*	1.182 $\pm$0.05	g/cm^3
d	250 $\pm$20	μm
L	15 $\pm$1	mm
g	2 $\pm$1	mm
ρ_a	1 $\pm$.01	kg/m^3

*based on the material properties of Polymethyl - Methacrylate Resin

erratically, potentially leading to erroneous data. Experimental data derived from Roshko (1954) shows that the Strouhal number, St versus Re obeys the empirical relationship $St = 0.212(1 - 21.2/Re)$ between $46 < Re < 180$. Figure 2.3 shows the equivalent dimensional relationship between the actual shedding frequency f_s, and the approach flow speed, U_∞, obtained by assuming a fiber diameter of 0.25 mm along with standard properties of air. Note below $U_\infty = 3$ m/s, vortex shedding ceases to exist. At the onset of vortex shedding, $f_s \approx 1250$ Hz. This value increases proportionally with increasing U_∞. Since the range of calculated f_s lies well above the natural frequency of the current fiber, vortex shedding is not expected to cause resonance in the present design.

2.4 Shell Geometry

Table 2.5 lists the three basic components described in the previous section. These components along with the required circuitry are packaged into a single plastic aerodynamic shell. Figure 2.4 and Figure 2.5 show the dimensional schematics and isometric views of the final shell. The shell is constructed of plastic and formed using a rapid prototyping method.

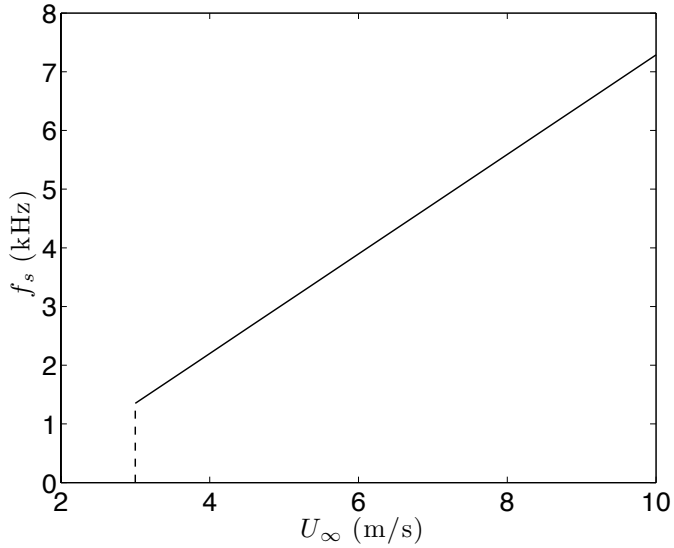

Figure 2.3. Expected vortex shedding frequency as a function of flow speed over the current optical fiber.

Table 2.5. Hardware components of velocity probe

Position Sensitive Diode	Hamamatsu S4583-04	• Active Area: 3.0 x 1.0 mm^2 • Spectral Range: 760–1100 nm • Detection Error: $\pm$ 10 μm • Rise Time: 10 μs
Vertical Cavity Surface Emmitting Laser	TT electronics Optek OPV322	• Output Wavelength: 850 nm • Minimum Output Power: 1.5 mW • Package Size: $\emptyset$ 1.57 mm • Operating Voltage: 2.2 V
High-Perfomance Plastic Optical Fiber	Mitsubishi Rayon Co. SuperESKA SK-10	• Single Mode Type • Design Wavelength: 600–1000 nm • Youngs Modulus: 4 GPa • Cladding Diameter: 250 μm • Core Diameter: 240 μm

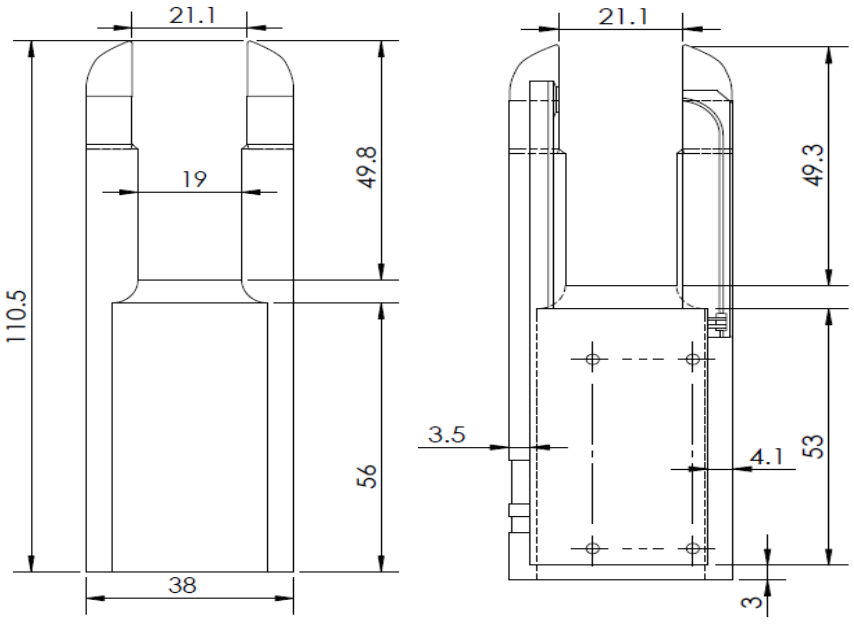

Figure 2.4. Outer (left) and inner (right) dimensioned schematics of the sensor shell. The units are in mm.

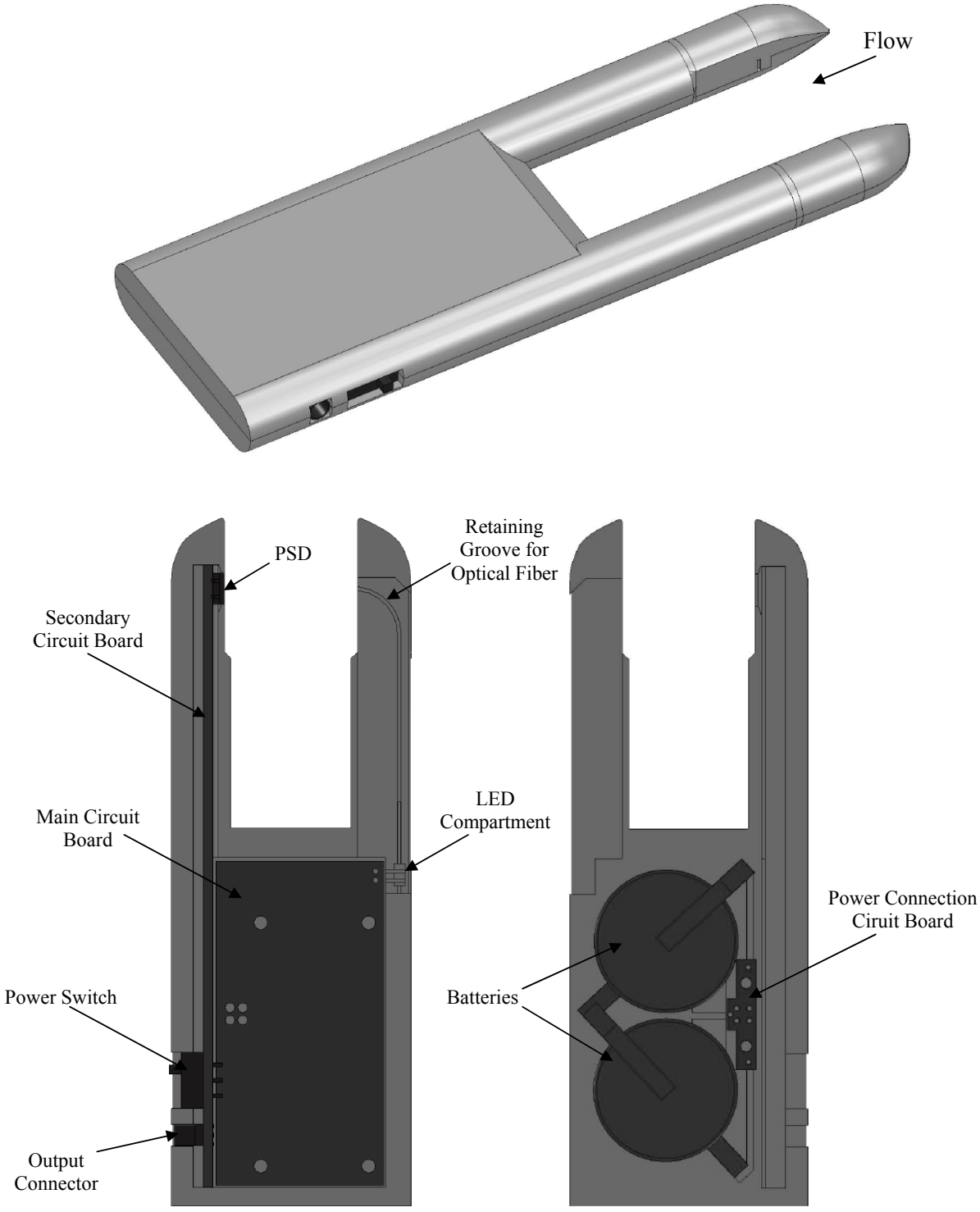

Figure 2.5. Isometric view (top) and inside view (bottom) of final CAD drawings. The nominal flow direction is labeled in the isometric view.

The length of the sensor body from the tip to the trailing edge is 110.5 mm and the width and height of the probe are 38 mm and 12.24 mm, respectively. A hollow cavity inside the aerodynamic shell provides housing for the electronic circuit boards, batteries, VSCEL, optical fiber and PSD. Each inner component fits securely into a hollow compartment designed specifically to hold it. The rest of the shell is made solid to iprove durability and reduce flexure. Two posts protruding out of the main shell cavity house the PSD, a circuit board and the optical fiber. The tips of the posts have been desinged in attempt to minimize the flow disturbance close to the optical fiber. The cylindrical posts have a diameter of 12.24 mm. The distance between the two faces flat faces on the posts is 21.1 mm.

2.4.1 Numerical Simulations

Numerical simulations performed in FLUENT were used to examine possible flow disturbance of the aerodynamic shell on the fiber, and observe the fluid-structure interaction between the optical fiber and the air. Two different sets of simulations were performed to investigate these effects. The first set focuses on the flow over the aerodynamic shell and thus does not specifically include the fiber. In contrast, the second set of simulations focuses only on the flow over the fiber and therefore does not specifically include the aerodynamic shell.

2.4.1.1 Flow Disturbance

The flow field around the entire velocity probe body was simulated using the implicit, second order, steady state solver with the Spalart-Allmaras one-dimensional turbulence model (Spalart & Allmaras, 1992) option in FLUENT. The computational domain was a rectangular box measuring 600 x 200 x 1000 mm^3 containing 725,477nodes. The leading edge of the velocity probe was placed in the domain 300 mm from the inlet face as shown in Figure 2.6. A triangular mesh was applied to all of the velocity probe surfaces and a tetrahedral mesh was applied to the inner domain. The meshing around the tips of the velocity probe had fine spacing of 0.1 mm. The inlet boundary condition was specified with a constant uniform velocity of 8 m/s in the z direction. The outlet boundary condition was defined

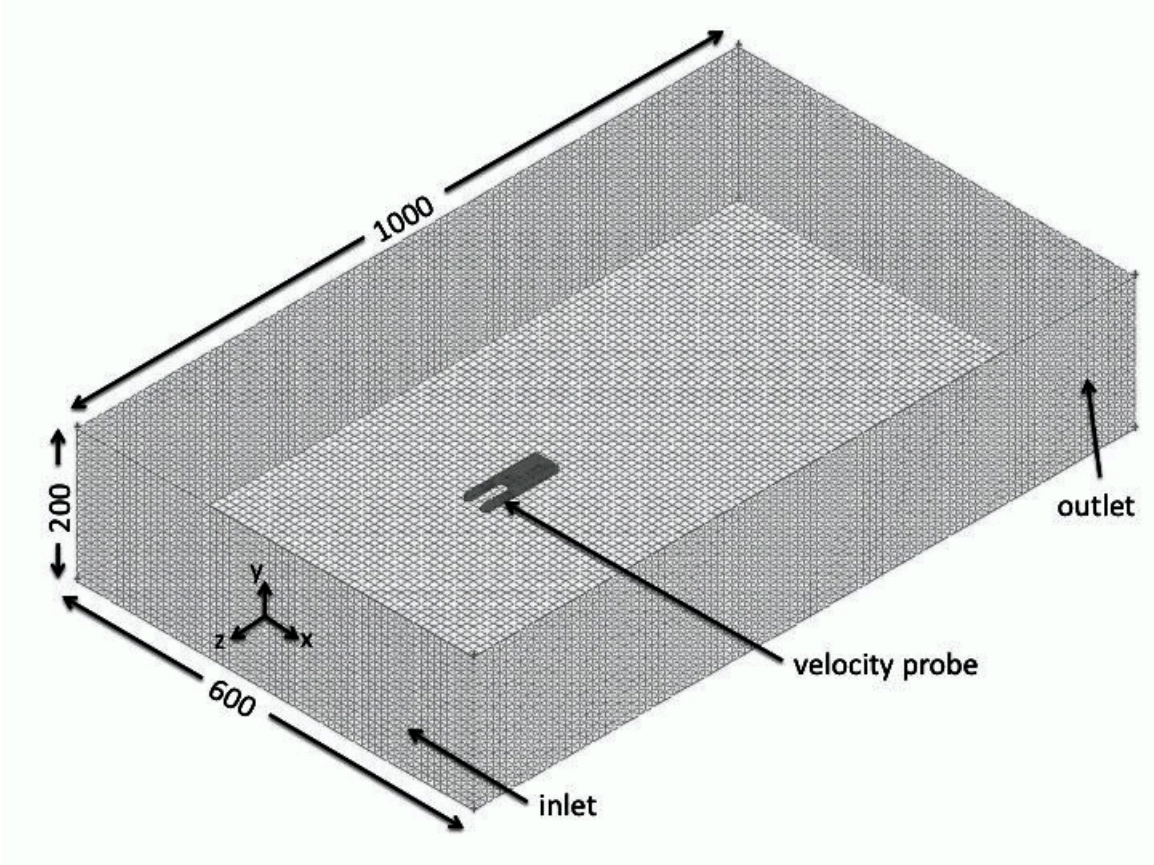

Figure 2.6. Scaled schematic of the compuational mesh used in the numerical simulations. All numerical values have units of mm.

as a pressure outlet boundary with zero gauge pressure. Because the size of the computational domain was much larger than the velocity probe, the four remaining sides were assigned symmetry boundary conditions. A constant air density of 1.225 kg/m^3 and a constant viscosity of 1.7894e-5 kg/(m s) were used in the analysis.

Figure 2.7 shows the velocity contours of the medial plane of the velocity probe for the case of $U_\infty = 8$ m/s. The velocity contours reveal the flow disturbance, caused mainly by the tips, lies mainly in front of the probe. Boundary layers forming along the posts are also visible in the contour plot. These boundary layers vary with flow speed.

Of particular interest in terms of the present design is the flow field in the region around the optical fiber. Figure 2.8 shows the velocity profile between the posts

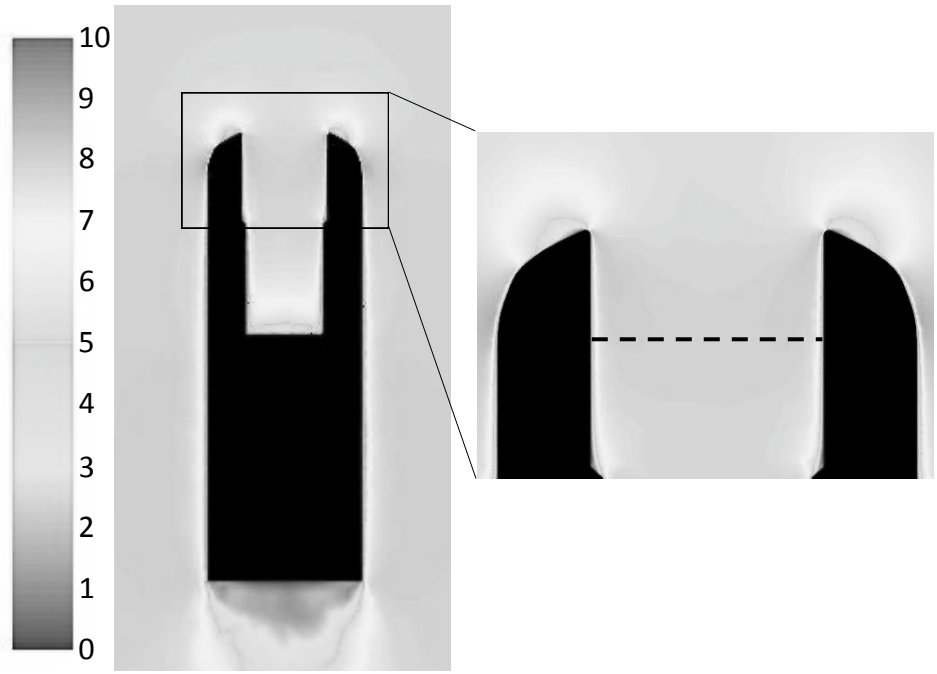

Figure 2.7. Velocity contour plot of the flow through the medial plane of the velocity probe. The colorbar represents the velocity magnitude in m/s. The expanded view shows the region near the optical fiber, and the dashed line indicates the location of the fiber.

at the location of the optical fiber for the case of $U_\infty = 8$ m/s. Boundary layers form equally along both posts. As shown in the figure the boundary layers extend about 2mm away from the edge of each post. Outside the boundary layers, the velocity profile remains uniform across the span between the posts with an average to within 1% of the inlet flow speed. This provides critical information in terms of selecting the gap size. If the free end of the optical fiber were to extend into the boundary layer, the distributed force along the optical fiber would not be uniform. The boundary layer thickness increases at the flow speed increases. Figure 2.8 also displays numerical simulation results observing the change in the boundary layer thickness as the inlet velocity increases. To ensure that the free end of the optical fiber does not penetrate into the boundary layeralong the opposite post, at least

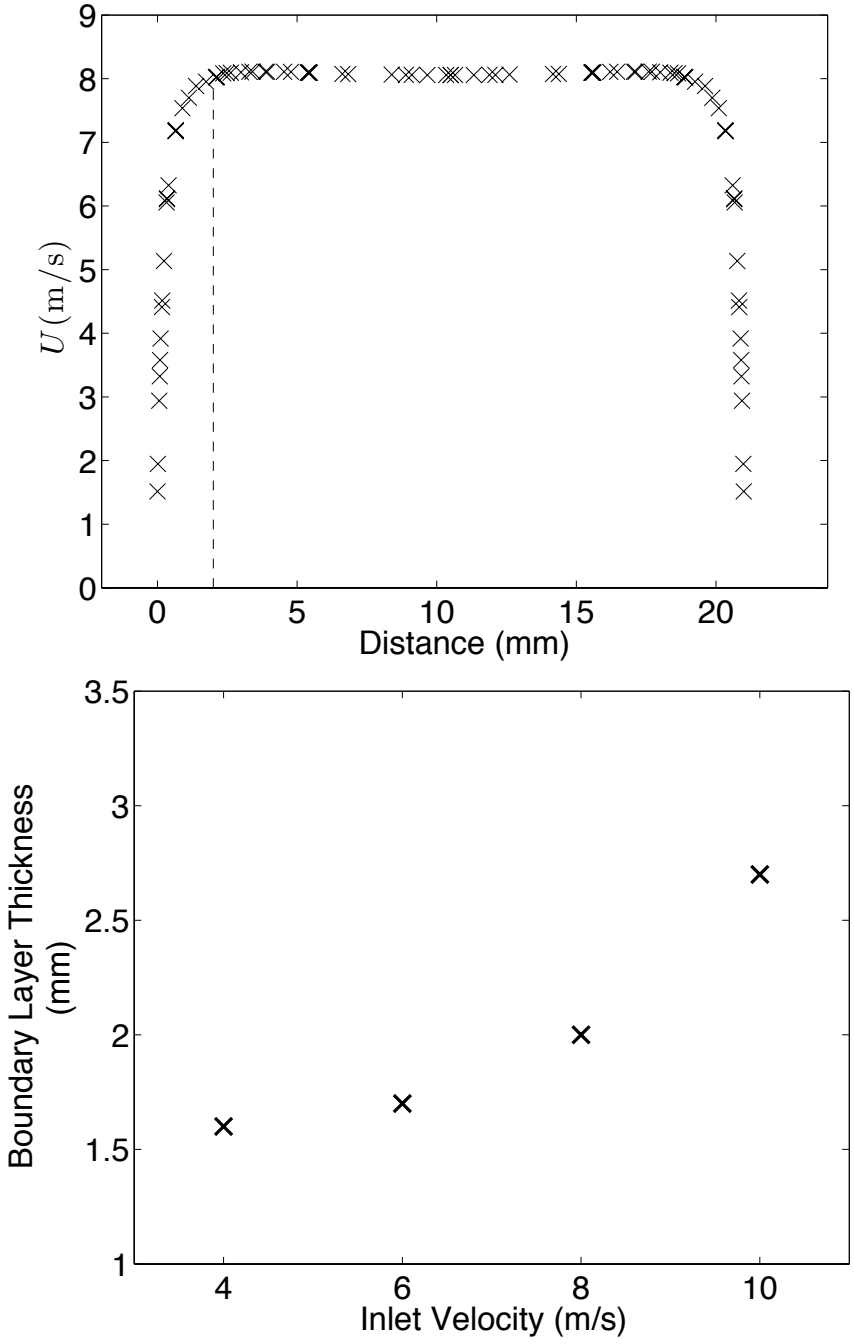

Figure 2.8. (Top)Velocity profile between the two posts of the aerodynamic shell at the location of the fiber. The dashed line indicates the edge of the 2 mm boundary layer.(Bottom) Numerical simulation data displaying the boundary layer thickness as the inlet velocity increases

for approach flow velocities less than $U_\infty = 8$ m/s, the gap length was set at $g = 2$ mm.

In order to investigate how changes in post spacing alters the observed flow in the vicinity of the fiber, additional simulations were done for the three cases listed in Table 2.6. Note, the third case with a post spacing of 21.23 mm matches that previously shown in Figures 2.7 and 2.8. The three different velocity profiles versus normalized distance across the posts are compared in Figure 2.9. Although, little difference appears to exist between the three cases, the flow does accelerate more in

Table 2.6. Flow disturbance comparison for different distances between the velocity robe posts. The percent difference is for an 8 m/s inlet flow velocity.

Post Spacing (mm)	U_∞ (m/s)	Percent Difference
17.5	8.12	1.48
19.7	8.09	1.10
21.23	8.08	0.99

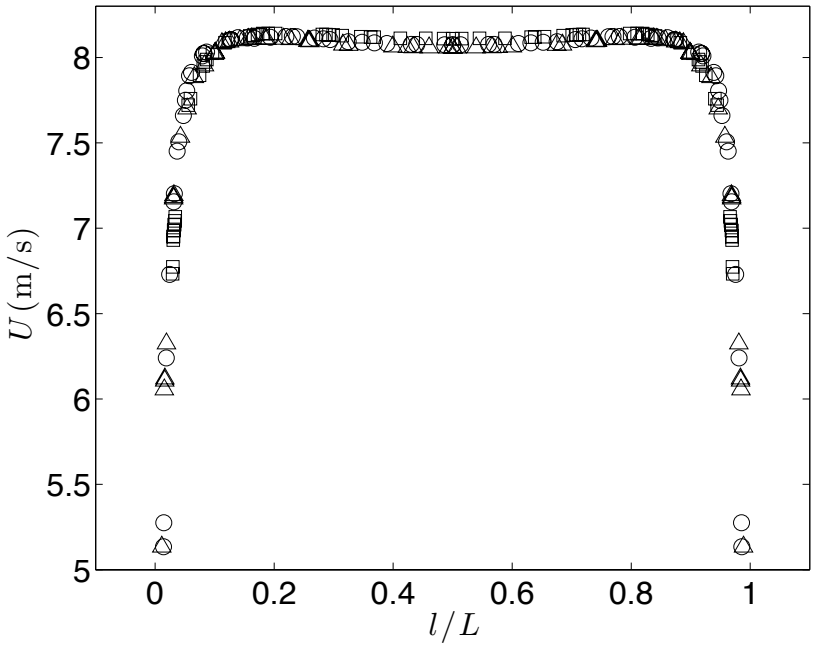

Figure 2.9. Velocity profiles for 3 different distances between the posts: □ 17.5mm, ○ 19.7mm, △ 21.13mm deg (corresponds to data in Figure 2.8). The distance between the posts was normalized for easier comparison.

the vicinity of the fiber as the post spacing decreases. Therefore, in order to achieve less than 1% difference due flow disturbance effects, the analysis indicates that the post spacing should remain at 20 mm or larger. Therefore, the aerodynamic shell based on the previous generation designs of Swope (2009) which had a post spacing of 21.3 mm, was continued to be used for the current velocity probe. This posed a minor problem because the length of the selected fiber, $L = 17.7$ mm plus the desired gap, $g = 2$ mm, measured less than the recommended post spacing.

To overcome this the clamped-end of the optical fiber was extended out of the post using hypodermic tubing, as shown in Figure 2.10. The hypodermic tubing is made of stainless steel and has a modulus of elasticity of 190 GPa. Because it is almost fifty times more rigid than the optical fiber, it does not significantly deflect due to the aerodynamic drag caused by the approach flow.

As discussed previously, the boundary layers along the two posts are about 2 mm thick. By using the hypodermic tubing to extend the clamped-end of the optical fiber away from the posts, the optical fiber itself will be almost completely out of the boundary layer, increasing the validity of the present model and the assumption of a uniform force distribution along the entire length of the optical fiber. Three-dimensional numerical simulations were performed in FLUENT to

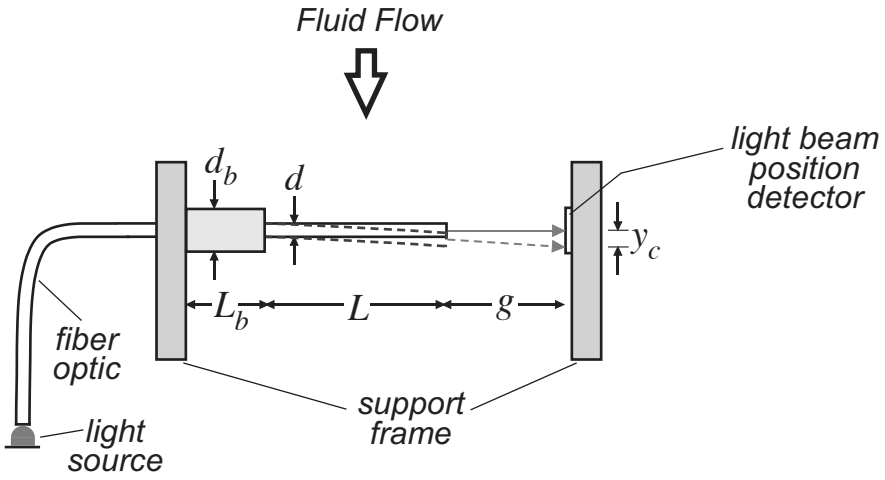

Figure 2.10. Schematic of the configuration including the hypodermic tubing at the clamped end of the fiber.

examine the aerodynamic drag force along the fiber both with and without the tubing. Simulations of flow over a cylinder with a step increase in diameter were compared to simulations of flow over a uniform diameter cylinder. The aerodynamic shell was not included in these simulations. The computational grid was refined twice to ensure that grid convergence had been obtained. The initial grid spacing in the vicinity of the optical fiber was 0.1mm. Subsequent refinements yielded grid spacing in the vicinity of the optical fiber of 0.05 mm and 0.025 mm. The drag force acting on the optical fiber was computed for all cases; the results are in Table 2.7. The drag force with the hypodermic tubing inserted is about 0.24 percent higher than the drag force without the tubing. Therefore at least for ratios $d/d_b < 0.5$, use of the tubing is not expected to adversely affect the performance of the velocity probe.

2.4.1.2 Fluid Structure Interaction

Fluid structure interaction (FSI) between the fiber and the air is the principle upon which the velocity probe is based. Two-dimensional numerical simulations were performed to examine the unsteady interaction between the air and the optical fiber, without the presence of the aerodynamic shell. Dynamic mesh capabilities in FLUENT along with user defined functions (UDF) programming were used to model the FSI problem. To simplify the numerics, a two-dimensional solver was utilized. Although this greatly reduced computational time and coding, the cost trade off was that realistic boundary conditions were difficult to reproduce. The velocity probe operates in a three-dimensional environment and fluid motion in the

Table 2.7. Difference between the force along a bare optical fiber and an optical fiber with tubing attached to it. Two grid refinements were performed to ensure grid independence

Grid Spacing (mm)	Bare Fiber (N)	With Tubing (N)	Percent Difference
0.1	4.26e-4	4.26e-4	0.01
0.05	4.60e-4	4.62e-4	0.34
0.025	4.49e-4	4.50e-4	0.23

third direction clearly cannot be captured in a two dimensional simulation. Another problem with the FSI simulation relates to the fact that the two-dimensional solver assumes the shape to be rectangular, whereas the actual optical fiber is circular. Because the flow does not move in the third direction the flow does not match the flow over the cylinder.

The custom written UDF was used to calculate beam deflection, and control the motion of the beam using the dynamic mesh feature in FLUENT (The appendix contains a custom tutorial that was developed to document this procedure). The procedure for performing the FSI simulations was as follows. First, the steady-state laminar flow over the undeflected beam (oriented with its longitudinal axis perpendicular to the flow) was obtained. From this solution, the equivalent distributed load, f on the beam was calculated by integrating the normal stresses acting on the beam. The subsequent deflection as a function of distance along the beam is then calculated from the static beam equation.

$$y(\ell) = \left(\frac{f\,L^4}{24\,E\,I}\right)\left[(\ell/L)^4 - 4\,(\ell/L)^3 + 6\,(\ell/L)^2\right]. \tag{2.6}$$

The solid boundaries defining the beam are moved accordingly; and, the mesh in a neighborhood surrounding the deflected beam is redrawn dynamically. This process is repeated for each time step. Note, the actual value of the time step used in these simulations was arbitrary because the deflection equation being used in the UDF represents that for a steady load. More complicated simulations including additional drag force from the movement of the beam itself were not attempted. Figure 2.11 illustrates the temporal behavior of y_c for two separate cases using an inlet of velocity of 2 m/s and 8 m/s. The data reveal that the end of the optical fiber oscillates around an average of 0.0165 mm and 0.221 mm, respectively. These values are 49% and 31% different than those from equation (2.1) using the empirical curve in Figure 2.2, which yielded deflections of 0.324 mm and 0.0323 mm respectively for $U_\infty = 2$ m/s and 8 m/s. Figure 2.12 displays the data compared to the empirical curve fit.

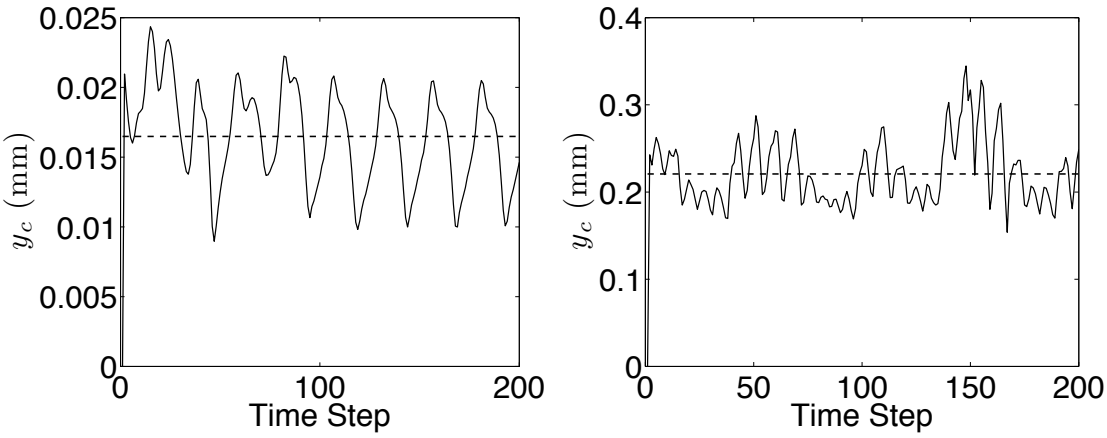

Figure 2.11. Results from the FSI numerical simulations:(top) inlet velocity of 2 m/s (bottom) inlet of 8 m/s. The dashed lines indicate the corresponding time averaged deflection.

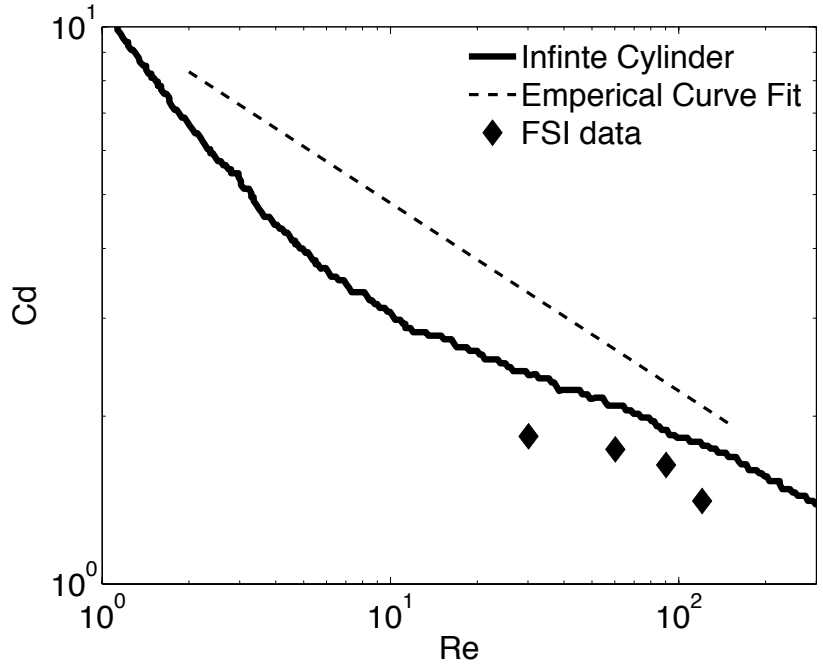

Figure 2.12. Cd versus Re data from the FSI numerical simulations compared to the Cd versus Re curve for flow over a cylinder and for the data obtained from Swope (2009).

CHAPTER 3

PROBE CHARACTERIZATION AND TESTING

3.1 Natural Frequency Verification

Verifying the natural frequency of the optical fiber serves two purposes. First it verifies the design equation used to optimize the velocity probe; and, second, it verifies the physical properties of the optical fiber. To accomplish this a free vibration experiment was performed. The optical fiber tested was the same SuperEska fiber as that listed in row 8 of Table 2.2, except with a length $L = 17.7$mm. In the experiments the free end of the optical fiber was pulled back, held at a fixed position, and then released. During this procedure the output signal of the PSD was recorded at a frequency of 1.5 kHz.

The natural frequency of the optical fiber was subsequently determined using a logarithmic decrement analysis. The logarithmic decrement is defined as (Thomson, 1972)

$$\delta = \ln \frac{y_1}{y_2}, \tag{3.1}$$

where y_1 and y_2 are the amplitudes of two successive peaks in the free vibration response. The decrement is used to determine the damping factor, ζ, and the natural frequency, ω_n. The damping factor is related to the logarithmic decrement as follows

$$\zeta = \frac{1}{\sqrt{1 + \left(\frac{2\pi}{\delta}\right)^2}}. \tag{3.2}$$

The time period between the two successive peaks is called the damped period, T. The natural frequency is related to the damping factor (ζ) and damped period (T) by

$$\omega_n = \frac{2\pi}{T\sqrt{1-\zeta^2}}. \tag{3.3}$$

The logarithmic decrement analysis was performed using 8 successive amplitude peaks. The experimental data, displayed in Figure 3.1, yielded measured values of $T = 4.7$ ms and $\delta = 0.203$. Substituting these values in (3.2) and (3.3) results in values of $\zeta = 0.03$ and $\omega_n = 1340$ rad/s. Another method for determining the natural frequency of the optical fiber is to perform a discrete Fourier transform of the experimental data. Figure 3.1 shows the results of the Fourier analysis. The dominant spike occurs at a frequency of 213 Hz, which translates into a natural frequency of 1337 rad/s, identical to the result obtained from the logarithmic decrement analysis.

Note, the predicted natural frequency from Table 2.3 is 1300 rad/s. The difference between the predicted and actual is about 2.9%, an acceptable agreement given the uncertainties in the length of the fiber, and its physical properties. The experimental results are important because they verify the mathematical model along with the material/physical properties of the fiber.

3.2 Velocity Probe Calibration

The velocity probe was calibrated by placing it near the exit plane of a slot jet calibration facility and comparing the output of signal to the average velocity measured using a pitot-static tube connected to a high precision differential pressure transducer. The slot jet facility is described in Metzger (2002). The approach flow velocity was controlled by adjusting the voltage of the power supply used to drive the axial fans mounted at one end of the jet facility. The output of the PSD and pressure transducer was sampled with an analog-to-digital converter at 1.5 kHz for 15 seconds for each velocity setting. The raw data were then averaged to obtain a mean value and standard deviation at each flow velocity. It was observed that as the flow speed increased the optical fiber oscillated with a higher amplitude, resulting in a larger standard deviation with velocity. Figure 3.2 displays the static calibration data in Table 3.1 compared to the prediction for y_c obtained from equation 2.1 using the material and geometric properties in Table 2.4 along with the C_d versus

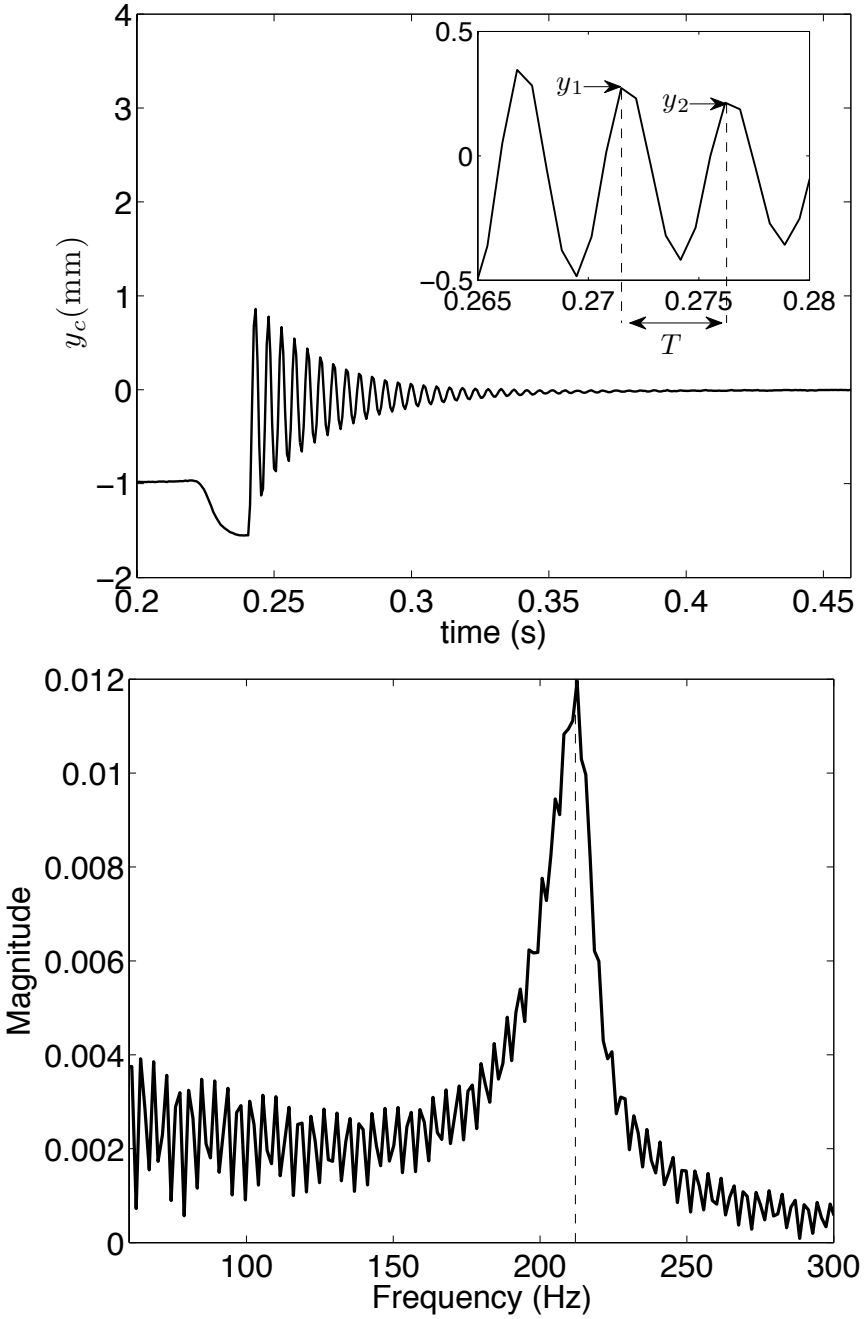

Figure 3.1. Free vibration response of the optical fiber. The actual data (top) provide information for the logarithmic decrement analysis. The inset plot shows an enlarged view of the oscillations with labels corresponding to verification equations. The variables y_1 and y_2 represent two successive amplitudes and T represents the damped period. The Fourier transform data (bottom) display the dominant frequency. The dotted line indicates the dominant frequency of 212.8 Hz.

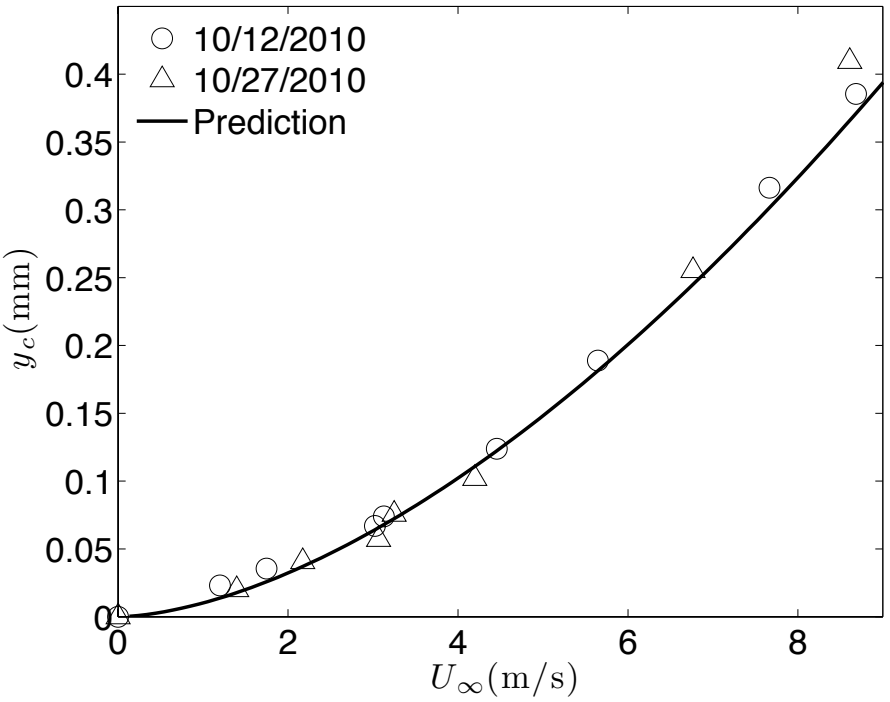

Figure 3.2. Calibration data displayed with theoretical predictions from data for flow over an infinite cylinder and the corrected prediction from section 2.3.3.

Table 3.1. Calibration data for calibration tests on October 12, 2010 and October 27, 2010 displayed with average deflection ($\bar{y_c}$) and standard deviation (σ_{y_c}).

10/12/2010 Test			10/27/2010 Test		
U_∞ (m/s)	$\bar{y_c}$ (mm)	σ_{y_c} (mm)	U_∞ (m/s)	$\bar{y_c}$ (mm)	σ_{y_c} (mm)
1.20	0.02	2.51e-6	1.40	0.02	2.04e-6
1.75	0.04	2.45e-6	2.17	0.04	2.34e-6
3.02	0.07	2.66e-6	3.06	0.06	1.96e-6
3.13	0.07	2.99e-6	3.25	0.07	2.89e-6
4.46	0.12	3.37e-6	4.20	0.10	2.46e-6
7.67	0.32	4.34e-6	6.77	0.26	4.61e-6
8.69	0.39	5.53e-6	8.61	0.41	8.55e-6

Re curve provided by Swope (2009) as shown in Figure 2.2.The data displayed in Figure 3.2 were used to create a calibration curve using a least squares regression fit to a second order polynomial. The regression analysis produced the relationship,

$$y_c = \left(4.40 \times 10^{-6}\right) U_\infty^2 + \left(7.51 \times 10^{-6}\right) U_\infty + 2.49 \times 10^{-6}. \tag{3.4}$$

Using the quadratic formula to solve (3.4) for U_∞ as a function of optical fiber deflection results in

$$U_\infty = \frac{(-7.51 \times 10^{-6}) + \sqrt{1.25 \times 10^{-11} + 1.76 \times 10^{-5} y_c}}{8.80 \times 10^{-6}}. \tag{3.5}$$

Figure 3.3 displays the data with the calibration curve generated from equation 3.5.

3.3 Uncertainty Analysis

The uncertainty of the output can be estimated through an analysis similar to the sensitivity analysis provided previously (details given in the Appendix). To

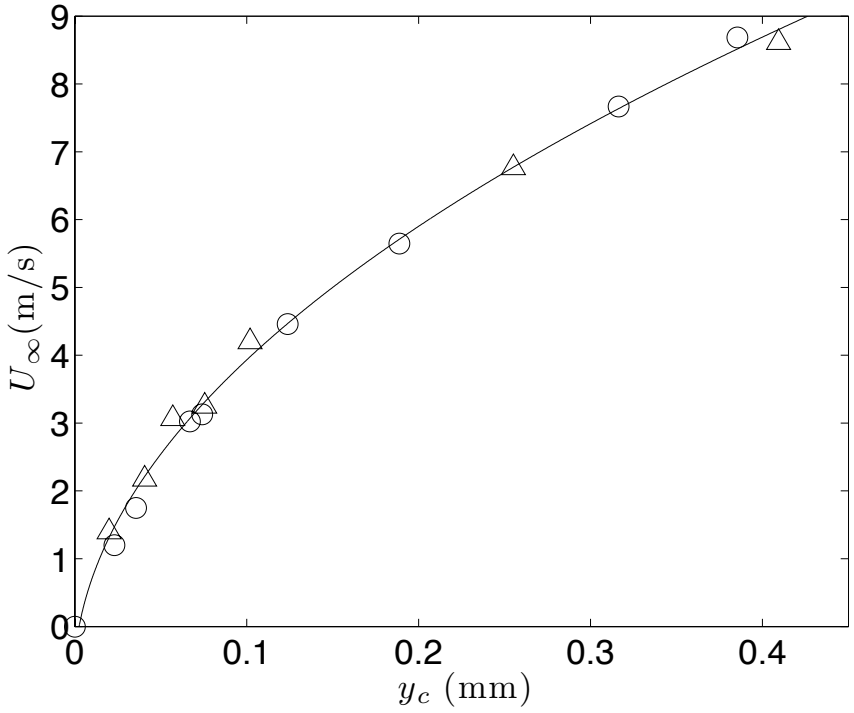

Figure 3.3. Calibration data along with the regression curve in equation 3.5 The data correspond to the data in Figure 3.2

determine the uncertainty in velocity measurements recorded by the velocity probe equation (2.1) is rearranged to solve for U_∞, resulting in

$$U_\infty = \left(\frac{16 y_c EI}{C_d \rho_a d L^4} \left(1 + \frac{4g}{3L} \right) \right)^{1/2}. \tag{3.6}$$

Performing the same differential analysis on equation (3.6)(details given in the Appendix) to obtain the uncertainty of U_∞ measurements based on deflection measurement only is denoted by Δ_{U_∞}, and given as

$$\Delta_{U_\infty} = \frac{1}{2} \frac{\Delta_{y_c}}{y_c} U_\infty. \tag{3.7}$$

The uncertainty of U_∞ based only on the uncertainty of the PSD measurements decreases slightly as U_∞ increases. Figure 3.4 shows the prediction curve along with expected error bars. The uncertainty corresponding to 1.05 m/s and 8.03 m/s are $\Delta_{U_\infty} = \pm 0.47$ m/s (45%) and $\Delta_{U_\infty} = \pm 0.12$ m/s (1.5%), respectively.

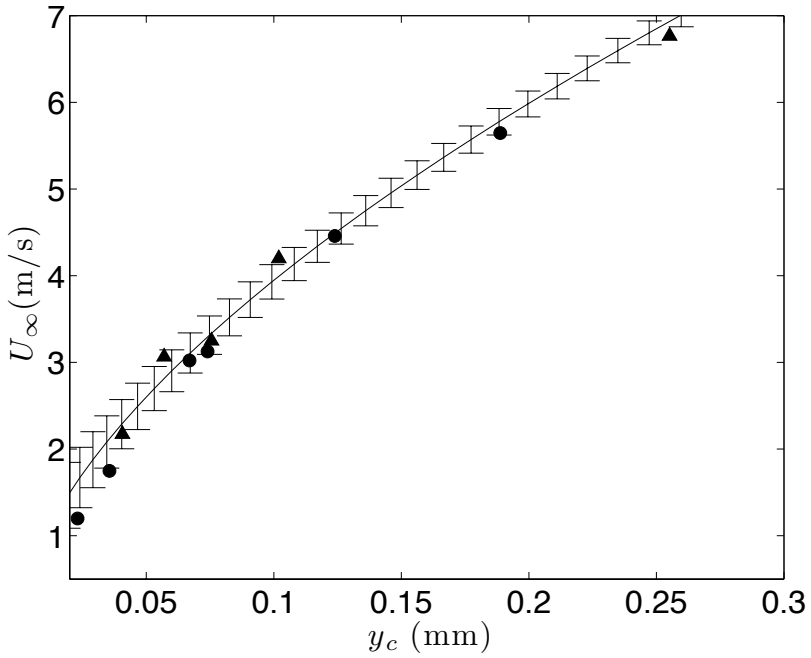

Figure 3.4. Expected uncertainty in velocity measurements due to the uncertainty of the PSD chip. The data points correspond to the calibration data in Figures 3.2 and 3.3. The errorbars represent the expected uncertainty in the velocity measurements.

3.4 Turbulence Testing

The velocity probe is specifically designed for turbulence measurements in airflow. The same slot jet facility used for calibration was also used to evaluate the turbulence measurement capability of the velocity probe in comparison to a typical hot-wire probe, which has superior spatiotemporal resolution. The velocity probe was placed such that the optical fiber was located in the central core of the jet and $1.9h$ downstream from the jet exit plane, where h denotes the height of the jet orifice. Data were collected at three different flow speeds over a time span of 1 minute each, with a sampling frequency of 5 kHz. Data from a hot-wire probe (TSI 2073) were simultaneously recorded at the same sampling rate and from the same location, albeit slightly offset in the transverse direction. Table 3.2 displays the statistical properties of the flow as recorded by each probe. The mean flow speed recorded by each probe has a maximum difference of 1.48%. As the flow speed increases the standard deviation of the velocity probe increases at a greater rate than the hot-wire probe. For example the hot-wire measured a turbulence intensity of 5.6% at $U_\infty = 8.7$m/s while the velocity probe measured a turbulence intensity of 9.2%. This discrepancy may be attributed to resonance of the optical fiber, as described further below.

An additional test was performed in which the optical fiber was located in the shear layer along the edge of the jet at $1.4h$ down stream of the jet orifice and $1.9h$ above the centerline. Data were recorded at two flow velocities; the statistics are presented in Table 3.3. Note, the mean velocities recorded by the hot-wire at this location were close to or less than 1 m/s. As previously mentioned the velocity

Table 3.2. Statistical results of turbulence data taken inside the jet core at $1.9h$ down stream.

	$U_j = 5.65$ m/s		$U_j = 7.66$ m/s		$U_j = 8.71$ m/s	
	Probe	Hot-wire	Probe	Hot-wire	Probe	Hot-wire
Mean (m/s)	5.83	5.92	7.69	7.75	8.54	8.66
Std (m/s)	0.34	0.38	0.60	0.48	0.79	0.49
Skewness	-0.31	0.16	-0.41	0.27	-0.36	0.32
Kurtosis	3.22	3.04	3.22	3.10	3.27	3.21

Table 3.3. Statistical results of turbulence data near edgeof jet at $1.4h$ down stream and $1.9h$ above the jet centerline.

	$U_j = 4.39$ m/s		$U_j = 8.63$ m/s	
	Probe	Hot-wire	Probe	Hot-wire
Mean (m/s)	0.53	0.41	2.08	1.12
Std (m/s)	0.42	0.23	0.48	0.64
Skewness	0.56	0.91	0.22	0.74
Kurtosis	3.03	3.50	2.46	3.12

probe is designed for flow speeds above 1 m/s. Hence, only turbulent motions with characteristic velocities greater than 1 m/s are accurately captured by the velocity probe, leaving the motions with smaller velocities completely neglected. This necessarily biases the measurements toward higher mean values. This effect is likely exacerbated by the poor spatial resolution experienced by the velocity probe in this particular flow, i.e. the length of the optical fiber measures only slightly less than the width of the jet. Therefore, turbulent motions with length scales less than h will not be accurately captured by the velocity probe. At the edge of the jet, these motions also likely have smaller velocities.

The corresponding spectra from the turbulence tests are displayed in Figure 3.5. Note, the area under each spectral curve represents the measured variance. In all cases, the spectra produced from the data collected with the velocity probe show a spike at a frequency near the natural frequency (207 Hz). This spike represents additional energy due to resonance. Below the natural, or resonate frequency, the velocity probe performs well in terms of capturing the same spectra energy of the turbulence compared to the hot-wire. This holds true for each of the five cases examined. In some instances a slight offset between the hotwire and velocity probe spectra may be observed. This is due to differences in the variance measured between the two sensors; recall that the spectra were normalized by the variance. Additional energy at the resonant frequency causes a bias on the variance of the velocity probe toward higher values.

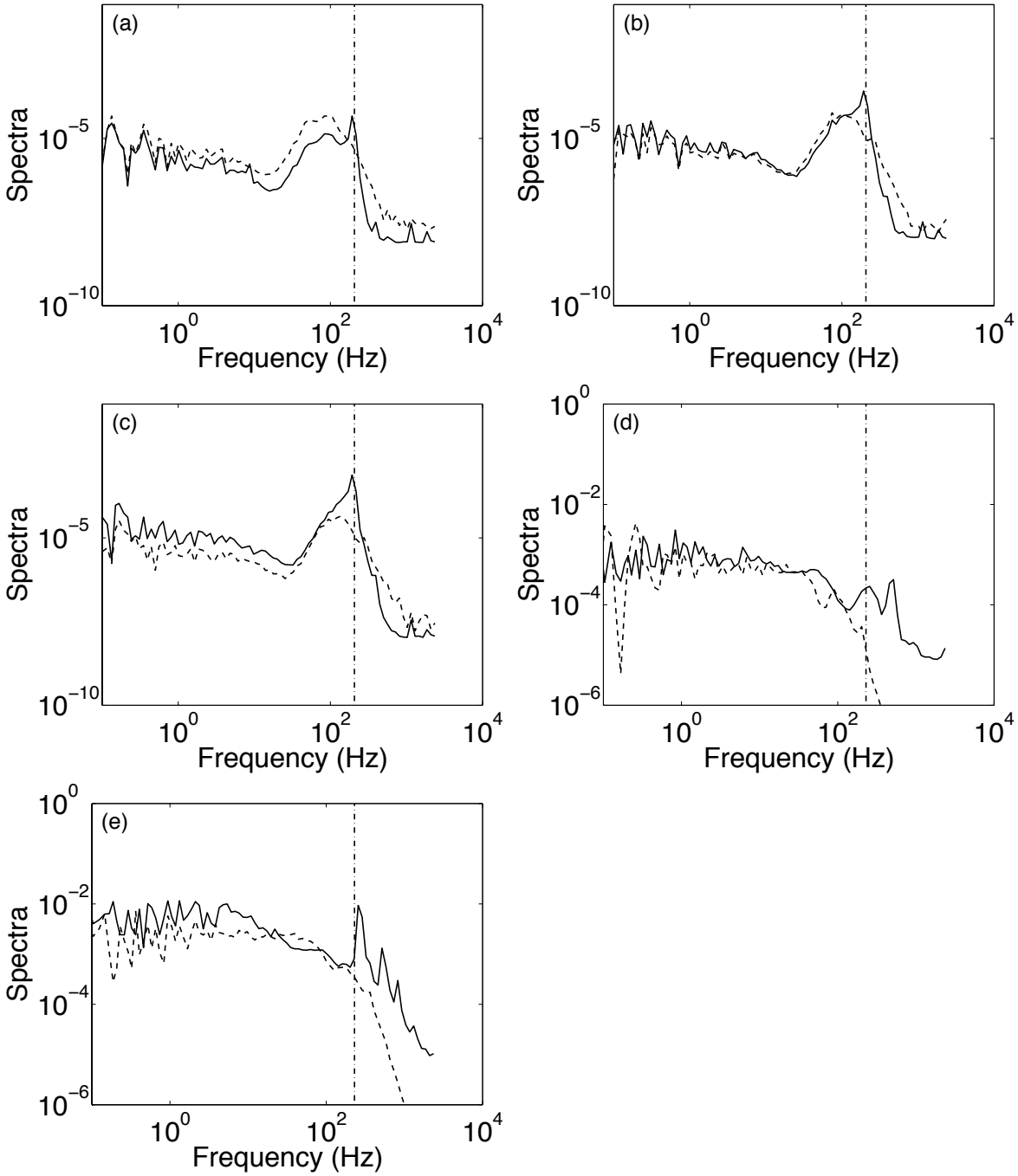

Figure 3.5. Spectra plots of turbulence data. — velocity probe, −− hot-wire probe. Inside jet core: (a) $U_j = 5.6$ m/s, (b) $U_j = 7.7$ m/s, (c) $U_j = 8.7$ m/s. Near edge of jet: (d) $U_j = 4.4$ m/s, (e) $U_j = 8.6$ m/s. The vertical lines denote the natural frequency of the fiber.

CHAPTER 4

SUMMARY

The MOBV probe fills the gap between the sonic anemometers and hot-wire anemometers by obtaining a frequency response of 207 Hz and being more robust than a hotwire. It differs from these and other anemometers through its mode of capturing wind velocity and velocity fluctuations. A single mode plastic optical fiber is cantilevered perpendicular to an oncoming flow. A vertical cavity surface emitting laser (VCSEL) illuminates the clamped end of the fiber, which transmits light through to a position sensitive detector (PSD). The fiber deflects from the drag force created by the oncoming flow and the position of the light beam is detected by the PSD. The output of the PSD is recorded using a digital to analog converter and through minimal post processing the flow velocity and its fluctuations can be determined.

The probe was developed using a theory-based design approach. A sensitivity analysis of the two design equations describing optical fiber deflection (y_c) and natural frequency (ω_n) showed that the probe's performance depends significantly on the geometric properties of the optical fiber. Using this analysis it was determined that the optimal fiber length was 17.7 mm. Numerical simulations provided information about the flow field in the area of the optical fiber. Boundary layers that form along the posts of the aerodynamic shell grew to a maximum of 2mm for the target velocity range; therefore the gap between the free end of the fiber and the PSD was determined to be 2mm. To avoid a potentially costly redesign of the aerodynamic shell, hypodermic tubing was utilized to extend the clamped-end of the fiber away from one of the posts. This addition not only shortened the length of the optical fiber to 17.7 mm, but also moved the clamped end of the fiber out of the boundary

layer. With the gap set at 2 mm and the hypodermic tubing extending the clamped end out of the boundary layer, the entire exposed portion of fiber was subject to a uniform drag force, making the current mathematical model more valid. Additional numerical simulations were used to show basic fluid-structure interaction between the fiber and flow. The simulations demonstrated the oscillatory behavior of the fiber. Because the simulations were very simple, however, they did not accurately predict the actual deflection or behavior of the fiber in real time.

Once the probe design was complete calibration and testing was possible. Tests using a slot jet calibration facility were used to calibrate the probe. The data collected showed that the probe behaved as the mathematic model predicted, with only slight variation. The natural frequency of the optical fiber was tested and also shown to be 212 Hz, which is within 3% of the expected value of 207 predicted by the mathematical model. Turbulence testing utilizing the same slot jet calibration facility was also completed along side of a hot-wire probe. The velocity probe data was compared to the hot-wire data and shown to match when airflow is within the range specified for the probe. The calibration and turbulence data demonstrated the viability of using the probe for velocity and turbulence data collection.

4.1 Future Work

Though substantial progress was made in terms of fabricating a working prototype, all of the desired characteristics for the velocity probe were not met. Future work and development can be done to yet improve upon the current design. A few suggestions are given here.

Improvements in the electronic circuitry of the probe are necessary to increase the usability and performance of the sensor. An op-amp failure in the custom electronics caused a variety of problems including a delay in testing. Therefore, effort needs to be focused on a more robust circuit design.

Including a wireless data acquisition (DAQ) system would greatly increase the sensor's versatility. If data could be collected wirelessly, setting up sensors in various locations would become almost trivial. Wireless DAQ would also facilitate

experiments utilizing very large arrays of sensors. One of the greatest motivations for designing the velocity probe was to produce an inexpensive sensor that could easily be deployed in large numbers.

Another improvement that would facilitate large sensor arrays would be an external, removable battery pack that can be attached directly to the aerodynamic shell of the probe. This would allow for the use of the probe remotely. Being removable it would accommodate the use of other power sources as well.

If a battery pack were to be used, it would be advantages to reduce the power consumption. One method to lower power consumption is to strobe the VCSEL laser. Strobing the laser at a low duty cycle will decrease power consumption proportionally without affecting the output, especially if the VCSEL is strobed at a frequency higher than the natural frequency of the optical fiber.

The current probe only measures velocity in one direction thereby significantly restricting its application. Incorporating two-dimensional velocity readings would permit direct measurement momentum flux and allow for a more diverse set of experimental scenarios. Current PSD technology limits this because the two-dimensional PSDs have twice the absolute error as the one-dimensional PSDs. As PSD technology advances, the capabilities of the velocity probe will also advance accordingly.

Finally, incorporating a fast-response temperature sensor (such as a fire wire thermocouple) would allow for heat flux measurements, which is of particular interest in the atmospheric sciences especially for purposes of examining the surface energy budget.

APPENDIX A

DERIVATION OF DESIGN EQUATIONS

This section provides the derivation of the two design equations characterizing deflection and natural frequency.

A.1 Deflection Equation

The mathematical model used to describe the deflection (y_c) of the optical fiber assumes that it acts as a cantilever beam under a uniformly distributed load. The governing equation is (Thomson, 1972),

$$\frac{\partial^2}{\partial \ell^2}\left(E\,I\,\frac{\partial^2 y}{\partial \ell^2}\right) + \rho\,A\,\frac{\partial^2 y}{\partial t^2} = f, \tag{A.1}$$

where l denotes the distance along the fiber, f denotes the distributed load along the fiber, A is the cross-sectional area of the fiber, E is the modulus of elasticity of the fiber, ρ is the optical fiber's density and I is the area moment of inertial of the optical fiber. The boundary conditions are zero deflection and zero rotation at the mounted end of the optical fiber and zero shear and zero moment at the free end of the fiber:

$$y(\ell = 0, t) = 0, \quad \left.\frac{\partial y}{\partial \ell}\right|_{(\ell=0,t)} = 0, \quad \left.\frac{\partial^2 y}{\partial \ell^2}\right|_{(\ell=L,t)} = 0, \quad \text{and} \quad \left.\frac{\partial^3 y}{\partial \ell^3}\right|_{(\ell=L,t)} = 0. \tag{A.2}$$

The distributed force, f is determined using data for the coefficient of drag for flow over a cylinder. The total force can be calculated based on the definition for the coefficient of drag,

$$F_D = \tfrac{1}{2}\,C_d\,\rho_a\,U_\infty^2\,A_f, \tag{A.3}$$

where C_d denotes the coefficient of drag, A_f ($\equiv\ dL$) is the frontal area, ρ_a is the air density, and U_∞ is the mean approach flow speed. Dividing by the length of the fiber to get an expression of force per unit length results in,

$$f = \tfrac{1}{2}\, C_d\, \rho_a\, d\, U_\infty^2. \tag{A.4}$$

The steady-state solution of (A.1), i.e., the solution assuming $\frac{dy}{dt}$ is

$$y(\ell) = \left(\frac{f\, L^4}{24\, E\, I}\right) \left[(\ell/L)^4 - 4\, (\ell/L)^3 + 6\, (\ell/L)^2\right]. \tag{A.5}$$

The maximum deflection (y_m) occurs at the end of the optical fiber ($l = L$), i.e.,

$$y_m = y(\ell{=}L) = \frac{f\, L^4}{8\, E\, I}. \tag{A.6}$$

Combining equations A.4 and A.6 results in,

$$y_m = \frac{C_d\, \rho_a\, d\, L^4\, U_\infty^2}{16\, E\, I}. \tag{A.7}$$

Because of the gap, however, the position of the light beam on the PSD will be different than y_m. The coordinate y_c defines the location of the light beam on the PSD, as shown in Figure A.1, and can be calculated as follows

$$y_c = y_m + \underbrace{\left(\frac{dy}{d\ell}\Big|_{\ell=L}\right) g}_{y_g}. \tag{A.8}$$

The additional displacement y_g due to the gap is as follows,

$$y_g = \left(\frac{dy}{d\ell}\Big|_{\ell=L}\right) g = \left(\frac{C_d\, \rho_a\, d\, U_\infty^2\, L^3}{12\, E\, I}\right) g = \frac{4\, g\, y_m}{3\, L}. \tag{A.9}$$

Substituting equations A.7 and A.9 into equation A.8 produces an equation for the position of the light beam as a function of the approach flow speed as well as the geometric and material properties of the fiber as follows

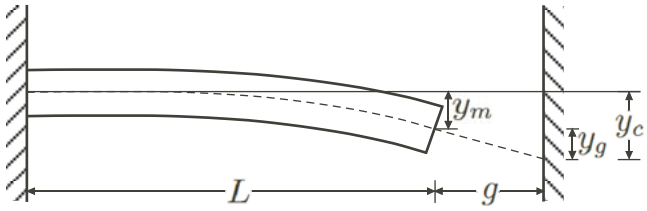

Figure A.1. Schematic illustrating the different deflection measurements y_m, y_g and y_c.

$$y_c = \frac{C_d\,\rho_a\,d\,U_\infty^2\,L^4}{16\,E\,I}\left[1+\frac{4\,g}{3\,L}\right]. \tag{A.10}$$

A.2 Natural Freqency Equation

The natural frequency(ω_n) of the optical fiber is calculated from the free-vibration response of the system, obtained by setting $f = 0$, in equation(A.1)

$$\frac{\partial^2}{\partial \ell^2}\left(E\,I\,\frac{\partial^2 y}{\partial \ell^2}\right) + \rho\,A\,\frac{\partial^2 y}{\partial t^2} = 0. \tag{A.11}$$

By assuming harmonic motion the solution takes the form,

$$y = -\alpha\,e^{\imath\,\omega\,t}. \tag{A.12}$$

The second derivative with respect to time of (A.12) is,

$$\frac{\partial^2 y}{\partial t^2} = \alpha\,\omega^2\,e^{\imath\,\omega\,t} = -\omega^2\,y. \tag{A.13}$$

Substituting (A.13) into (A.11) and assuming constant material properties of the optical fiber results in,

$$\frac{\partial^4 y}{\partial \ell^4} - \left(\frac{\rho\,A}{E\,I}\,\omega^2\right)^4 y = 0. \tag{A.14}$$

The general solution to (A.13) is

$$y = A\,\cosh\beta\ell + B\,\sinh\beta\ell + C\,\cos\beta\ell + D\,\sin\beta\ell, \tag{A.15}$$

where

$$\beta^4 = \frac{\rho\,A}{E\,I}\,\omega^2. \tag{A.16}$$

Applying the boundary condtions into the general solution results in,

$$(y)_{\ell=0} = A + C, \qquad \therefore A = -C \tag{A.17}$$

$$\left(\frac{dy}{dx}\right)_{\ell=0} = \beta\,\left[A\,\sinh\beta\,\ell + B\cosh\beta\,\ell - C\sin\beta\,\ell + D\cos\beta\,\ell\right]_{\ell=0} = 0$$

$$\beta\,[B+D] = 0, \qquad \therefore B = -D \tag{A.18}$$

$$\left(\frac{d^2y}{dx^2}\right)_{\ell=1} = \beta^2\,[A\cosh\beta\,L + B\sinh\beta\,L - C\cos\beta\,L - D\,\sin\beta\,L] = 0$$

$$A\,(\cosh\beta\,L + \cos\beta\,L) + B\,(\sinh\beta\,L + \sin\beta\,L) = 0 \tag{A.19}$$

$$\left(\frac{d^3y}{dx^3}\right)_{\ell=1} = \beta^3\left[A\sinh\beta L + B\cosh\beta L + C\sin\beta L - D\cos\beta L\right] = 0$$
$$A\left(\sinh\beta L - \sin\beta L\right) + B\left(\cosh\beta L + \cos\beta L\right) = 0 \tag{A.20}$$

Dividing (A.19) by (A.20) results in,

$$\frac{\cosh\beta L + \cos\beta L}{\sinh\beta L - \sin\beta L} = \frac{\sinh\beta L + \sin\beta L}{\cosh\beta L + \cos\beta L}, \tag{A.21}$$

which reduces to

$$\cosh\beta L\,\cos\beta L + 1 = 0. \tag{A.22}$$

Equation A.22 is satisfied by a number of values of βL corresponding to each normal mode of oscillation. The first three normal modes are $\beta L = 1.875$, $\beta L = 4.733$, and $\beta L = 7.85$ respectively. The natural frequency is determined from the first or fundamental mode of oscillation. Substituting this relationship in to equation A.16 gives an equation for the natural frequency, based on geometric and material properties of the fiber, as follows

$$\omega_n = \frac{1.875^2}{L^2}\sqrt{\frac{E\,I}{\rho\,A}}. \tag{A.23}$$

APPENDIX B

SENSITIVITY AND UNCERTAINTY ANALYSIS

This section outlines the Taylor series expansion used in the sensitivity and uncertainty analysis. Results from the analysis provide insight into how sensitive the equations are to each parameter. For the general case where r is a function of J variables X_i for $i = 1, ..., j$,i.e,

$$r = r\left(X_1, X_2, ...X_j\right), \tag{B.1}$$

A first order Taylor series expansion provides an estimate of r at $X_i + \Delta X_i$ for $i = 1, ..., j$,

$$r\left(X_i + \Delta X_i\right) = r\left(X_i\right) + \frac{\partial r}{\partial X_i}\Delta X_i, \tag{B.2}$$

where $r(X + \Delta X) = r(X_i) + \Delta r(X_i)$. Solving for Δr yields

$$\Delta r = \frac{\partial r}{\partial X_1}\Delta X_1 + ... + \frac{\partial r}{\partial X}\Delta X_j. \tag{B.3}$$

The best estimate for the uncertainty in r is (Coleman & Steele, 1989)

$$\sigma_r = \left[\left(\frac{\partial r}{\partial X_1}\Delta_{X_1}\right)^2 + \left(\frac{\partial r}{\partial X_2}\Delta_{X_2}\right)^2 + ... + \left(\frac{\partial r}{\partial X_J}\Delta_{X_j}\right)^2\right]^{1/2}. \tag{B.4}$$

For the sensitivity analysis, the partial derivatives in equation (B.4) represent the sensitivity coefficients and quantify how sensitive r is to each variable.

B.1 Deflection Equation Analysis

Beginning with the design equation for deflection,

$$y_c = \frac{C_d\,\rho_a\,d\,U_\infty^2\,L^4}{16\,E\,I}\left[1 + \frac{4\,g}{3\,L}\right], \tag{B.5}$$

where

$$I = \frac{\pi\, d^4}{64}, \tag{B.6}$$

the general expression for uncertainty becomes,

$$\Delta_{y_c} = \frac{\partial\, y_c}{\partial\, C_d}\,\Delta_{C_d} + \frac{\partial\, y_c}{\partial\, \rho_a}\,\Delta_{\rho_a} + \frac{\partial\, y_c}{\partial\, d}\,\Delta_d + \frac{\partial\, y_c}{\partial\, U_\infty}\,\Delta_{U_\infty} + \frac{\partial\, y_c}{\partial\, L}\,\Delta_L + \frac{\partial\, y_c}{\partial\, g}\,\Delta_g + \frac{\partial\, y_c}{\partial\, E}\,\Delta_E \tag{B.7}$$

The partial derivatives are:

$$\frac{\partial\, yc}{\partial\, C_d} = \frac{\rho_a\, d\, U_\infty^2\, L^4}{16\, E\, I}\left[1 + \frac{4\, g}{3\, L}\right] = \frac{y_c}{C_d}, \tag{B.8}$$

$$\frac{\partial\, y_c}{\partial\, \rho_a} = \frac{C_d\, d\, U_\infty^2\, L^4}{16\, E\, I}\left[1 + \frac{4\, g}{3\, L}\right] = \frac{y_c}{\rho_a}, \tag{B.9}$$

$$\frac{\partial\, y_c}{\partial\, d} = -3\frac{C_d\, \rho_a\, U_\infty^2\, L^4}{16\, E\, I}\left[1 + \frac{4\, g}{3\, L}\right] = -3\frac{y_c}{d}, \tag{B.10}$$

$$\frac{\partial\, y_c}{\partial\, U_\infty} = 2\frac{C_d\, \rho_a\, d\, U_\infty\, L^4}{16\, E\, I}\left[1 + \frac{4\, g}{3\, L}\right] = 2\frac{y_c}{U_\infty}, \tag{B.11}$$

$$\frac{\partial\, y_c}{\partial\, L} = 12\frac{L+g}{3L+4g}\frac{C_d\, \rho_a\, d\, U_\infty^2\, L^4}{16\, E\, I}\left[1 + \frac{4\, g}{3\, L}\right] = \left(12\frac{L+g}{3L+4g}\right)\frac{y_c}{L}, \tag{B.12}$$

$$\frac{\partial\, y_c}{\partial\, L} = 4\frac{g}{3L+4g}\frac{C_d\, \rho_a\, d\, U_\infty^2\, L^4}{16\, E\, I}\left[1 + \frac{4\, g}{3\, L}\right] = \left(4\frac{g}{3L+4g}\right)\frac{y_c}{g}, \tag{B.13}$$

$$\frac{\partial\, y_c}{\partial\, E} = -\frac{C_d\, d\, U_\infty^2\, L^4}{16\, E^2\, I}\left[1 + \frac{4\, g}{3\, L}\right] = -\frac{y_c}{E}. \tag{B.14}$$

Substituting the partial derivatives back into (B.7) results in,

$$\Delta_{y_c} = \frac{y_c}{C_d}\,\Delta_{C_d} + \frac{y_c}{\rho_a}\,\Delta_{\rho_a} + -3\frac{y_c}{d}\,\Delta_d + 2\frac{y_c}{U_\infty}\,\Delta_{U_\infty} + \left(12\frac{L+g}{3L+4g}\right)\frac{y_c}{L}\,\Delta_L + \left(4\frac{g}{3L+4g}\right)\frac{y_c}{g}\,\Delta_g - \frac{y_c}{E}\Delta_E. \tag{B.15}$$

The best estimate for the uncertainty in y_c is derived from taking the square root of the sum of the squares (Coleman & Steele, 1989). Dividing each side of equation B.15 by y_c and taking the square root of the sum of the squares results in,

$$\sigma_{y_c} = \left[\left(\frac{\Delta C_d}{C_d} \right)^2 + \left(\frac{\Delta \rho_a}{\rho_a} \right)^2 + \left(-3 \frac{\Delta d}{d} \right)^2 + \left(2 \frac{\Delta U_\infty}{U_\infty} \right)^2 + \left(\frac{\Delta E}{E} \right)^2 + \left(12 \frac{L+g}{3L+4g} \right)^2 \left(\frac{\Delta L}{L} \right)^2 + \left(4 \frac{g}{3L+4g} \right)^2 \left(\frac{\Delta g}{g} \right)^2 \right]^{1/2}, \quad \text{(B.16)}$$

where

$$\sigma_{y_c} = \frac{\Delta_{y_c}}{y_c}. \quad \text{(B.17)}$$

.

B.2 Natural Frequency Analysis

Beginning with the design equation for the natural frequency,

$$\omega_n = \frac{1.875^2}{L^2} \sqrt{\frac{E\,I}{\rho\,A}}, \quad \text{(B.18)}$$

where

$$I = \frac{\pi\,d^4}{64}, \quad \text{(B.19)}$$

and

$$A = \frac{\pi\,d^2}{4}, \quad \text{(B.20)}$$

and following the same procedure in the previous section, the general expression for the uncertainty in the natural frequency is given by,

$$\Delta_{\omega_n} = \frac{\partial\,\omega_n}{\partial\,L}\,\Delta_L + \frac{\partial\,\omega_n}{\partial\,E}\,\Delta_E + \frac{\partial\,\omega_n}{\partial\,d}\,\Delta_d + \frac{\partial\,\omega_n}{\partial\,\rho}\,\Delta_\rho. \quad \text{(B.21)}$$

The partial derivatives are

$$\frac{\partial\,\omega_n}{\partial\,L} = -2\frac{1.875^2}{L^3}\sqrt{\frac{E\,I}{\rho\,A}} = -2\frac{\omega_n}{L}, \quad \text{(B.22)}$$

$$\frac{\partial\,\omega_n}{\partial\,E} = \frac{1}{2}\frac{1.875^2}{L^2}\sqrt{\frac{E\,I}{\rho\,A}} = \frac{1}{2}\frac{\omega_n}{E}, \quad \text{(B.23)}$$

$$\frac{\partial\,\omega_n}{\partial\,d} = \frac{1.875^2}{4\,L^2}\sqrt{\frac{E}{\rho}} = \frac{\omega_n}{d}, \quad \text{(B.24)}$$

$$\frac{\partial\,\omega_n}{\partial\,\rho} = -\frac{1}{2}\frac{1.875^2}{L^2}\sqrt{\frac{E\,I}{\rho^3\,A}} = -\frac{1}{2}\frac{\omega_n}{\rho}. \quad \text{(B.25)}$$

Substituting the partial derivatives back into (B.21) results in,

$$\Delta_{\omega_n} = -2\frac{\omega_n}{L}\,\Delta_L + \frac{1}{2}\frac{\omega_n}{E}\,\Delta_E + \frac{\omega_n}{d}, \Delta_d + -\frac{1}{2}\frac{\omega_n}{\rho}\,\Delta_\rho.4 \tag{B.26}$$

The best estimate for the uncertainty in ω_n is derived from taking the square root of the sum of the squares. Dividing each side of equation B.26 by ω_n and taking the square root of the sum of the squares, of the right hand side, results in,

$$\sigma_{\omega_n} = \left[4\left(\frac{\Delta L}{L}\right)^2 + \frac{1}{4}\left(\frac{\Delta E}{E}\right)^2 + \frac{1}{4}\left(\frac{\Delta \rho}{\rho}\right)^2 + \left(\frac{\Delta d}{d}\right)\right]^{1/2}, \tag{B.27}$$

where

$$\sigma_{\omega_n} = \frac{\Delta_{\omega_n}}{\omega_n}. \tag{B.28}$$

B.3 Uncertainty of U_∞ Due To Uncertainty in the PSD Chip

Beginning with the design equation for deflection

$$y_c = \frac{C_d\,\rho_a\,d\,U_\infty^2\,L^4}{16\,E\,I}\left[1 + \frac{4\,g}{3\,L}\right], \tag{B.29}$$

where

$$I = \frac{\pi\,d^4}{64}, \tag{B.30}$$

and rearranging to solve for U_∞ results in

$$U_\infty = \left(\frac{16 y_c E I}{C_d \rho_a d L^4}\left(1 + \frac{4g}{3L}\right)\right)^{1/2}. \tag{B.31}$$

Following the same procedure in the previous section, the general expression for the uncertainty in measurements of U_∞ is given by,

$$\Delta_{U_\infty} = \frac{\partial\,U_\infty}{\partial\,y_c}\,\Delta_{y_c} + \frac{\partial\,U_\infty}{\partial\,C_d}\,\Delta_{C_d} + \frac{\partial\,U_\infty}{\partial\,\rho_a}\,\Delta_{\rho_a} + \frac{\partial\,U_\infty}{\partial\,d}\,\Delta_d + \frac{\partial\,U_\infty}{\partial\,L}\,\Delta_L + \frac{\partial\,U_\infty}{\partial\,g}\,\Delta_g + \frac{\partial\,U_\infty}{\partial\,E}\,\Delta_E. \tag{B.32}$$

Assuming that only the uncertainty in the PSD measurement (y_c) is relevant (B.32) reduces to

$$\Delta_{U_\infty} = \frac{\partial\,U_\infty}{\partial\,y_c}\,\Delta_{y_c}. \tag{B.33}$$

The partial derivative is

$$\frac{\partial U_\infty}{\partial y_c} = \frac{1}{2}\left(\frac{16 y_c EI}{C_d \rho_a d L^4}\left(1+\frac{4g}{3L}\right)\right)^{-1/2}\left(\frac{16EI}{C_d \rho_a d L^4}\frac{1}{\left(1+\frac{4g}{3L}\right)}\right), \tag{B.34}$$

which reduces to

$$\frac{\partial U_\infty}{\partial y_c} = \frac{1}{2}\frac{U_\infty}{y_c}. \tag{B.35}$$

Substituting the partial derivative back into (B.33) results in,

$$\Delta_{U_\infty} = \frac{1}{2}\frac{\Delta_{y_c}}{y_c}U_\infty, \tag{B.36}$$

an equation for the uncertainty of U_∞ measurements as a result of the uncertainty in the PSD chip.

APPENDIX C

DESIGN TABLES

This section contains the design tables used to determine the optimal optical fiber for the velocity probe.

Table C.1. Complete design table for single mode optical fibers. (y_c is the deflction of optical fiber)

Fiber Type	Modulus (GPa)	Length (mm)	Diameter (mm)	y_c (mm) U_∞= 1 m/s	y_c (mm) U_∞= 8 m/s	ω_n (rad/s)
Silicone	70	15	0.125	3.11e-3	9.87e-2	2.53e3
Silicone	70	15	0.245	3.29e-4	1.04e-2	4.97e3
SuperEska	4	15	0.25	5.38e-3	1.71e-1	1.81e3
SuperEska	4	15	0.5	5.33e-4	1.69e-2	3.61e3
Silicone	70	17.5	0.125	5.63e-3-2	1.69e-1	1.86e3
Silicone	70	17.5	0.245	5.96e-4	1.89e-2	1.43e3
SuperEska	4	17.5	0.25	9.76e-3	3.10e-1	1.33e3
SuperEska	4	17.5	0.5	9.66e-4	3.07e-2	2.56e3
Silicone	70	20	0.125	9.45e-3	3.0e-1	1.43e3
Silicone	70	20	0.245	1.0-3	3.18e-2	2.79e3
SuperEska	4	20	0.25	1.64e-2	5.20e-1	1.02e3
SuperEska	4	20	0.5	1.62e-3	5.140e-2	2.03e3

Table C.2. Complete design table for multimode optical fibers. (y_c is the deflection of optical fiber)

Fiber Type	Modulus (GPa)	Length (mm)	Diameter (mm)	y_c (mm) U_∞= 1 m/s	y_c (mm) U_∞= 8 m/s	ω_n (rad/s)
Silicone	70	15	0.125	3.11e-3	9.87e-2	2.53e3
Silicone	70	15	0.22	4.71e-4	1.5e-2	4.46e3
Silicone	70	15	.23	4.06e-4	1.29e-2	4.66e3
Silicone	70	15	.26	2.7e-4	8.57e-3	5.27e3
Silicone	70	15	.33	1.22e-4	3.87e-3	6.69e3
Silicone	70	15	.425	5.24e-5	1.66e-3	8.61e3
Silicone	70	15	.43	5.03e-5	1.6e-3	8.72e3
Silicone	70	15	.63	1.41e-5	4.47e-4	1.28e4
Silicone	70	15	.73	8.61e-6	2.73e-4	1.48e4
Silicone	70	15	1.24	1.47e-6	4.67e-5	2.51e4
Silicone	70	15	1.55	6.98e-7	2.22e-5	3.14e4
Silicone	70	17.5	.125	5.63e-3	1.79e-1	1.86e3
Silicone	70	17.5	.22	8.54e-4	2.71e-2	3.28e3
Silicone	70	17.5	.23	7.36e-4	2.34e-2	3.42e3
Silicone	70	17.5	.26	4.89e-4	1.55e-2	3.87e3
Silicone	70	17.5	.33	2.21e-4	7.01e-3	4.91e3
Silicone	70	17.5	.425	9.49e-5	3.01e-3	6.33e3
Silicone	70	17.5	.43e	9.13e-5	2.9e-3	6.4e3
Silicone	70	17.5	.63	2.55e-5	8.10e-4	9.38e3
Silicone	70	17.5	.73	1.56e-5	4.95e-4	1.09e4
Silicone	70	17.5	1.24	2.66e-6	8.46e-5	1.85e4
Silicone	70	17.5	1.55	1.26e-6	4.02e-5	2.31e4
Silicone	70	20	.125	9.45e-3	3.0e-1	1.43e3
Silicone	70	20	.22	1.43e-3	4.55e-2	2.51e3
Silicone	70	20	.23	1.24e-3	3.92e-2	2.62e3
Silicone	70	20	.26	8.21e-4	2.61e-2	2.96e3
Silicone	70	20	.33	3.7e-4	1.18e-2	3.76e3
Silicone	70	20	.425	1.59e-4	5.06e-3	4.85e3
Silicone	70	20	.43	1.53e-4	4.86e-3	4.9e3
Silicone	70	20	.63	4.28e-5	1.36-3	7.18e3
Silicone	70	20	.73	2.62e-5	8.313e-4	8.32e3
Silicone	70	20	1.24	4.47e-6	1.42e-4	1.41e4
Silicone	70	20	1.55	2.12e-6	6.47e-5	1.77e4

APPENDIX D

FLUENT AND GAMBIT TUTORIALS

Creating A Geometry and Mesh for Fluid Structure Interaction of a Cantilever Beam in a water channel.

Introduction

The purpose of this tutorial is to demonstrate geometry and grid generation for the use of the dynamic mesh capabilities in fluent..

This tutorial demonstrates the following:

- Creating simple geometry.
- Creating multiple faces for use with dynamic mesh.
- Specifying Boundary Conditions and Continuum types.
- Exporting a mesh file.

Prerequisites

This tutorial assumes that you have some experience with Gambit and have some familiarity with the interface. This tutorial uses the graphical user interface (GUI). The numbers associated with the different vertices, edges, and faces are contingent on following the tutorial exactly. See Appendix A for figures containing the vertex numbers, edge numbers and face numbers.

Problem Description

Consider a thin aluminum plate placed in a water channel perpendicular to the flow. The plate spans the entire width of the water channel but its ends are free from the walls to allow for it to deflect due to the forces caused by the on coming flow. The water channel width is 1m. This will allow us to solve the problem with a 2d solver in FLUENT because the assumed depth is one meter. The sheet of aluminum is 1/16" thick. See figure 1 for a schematic of the problem. This tutorial can be used in conjunction with the "Fluid Structure Interaction: Cantilever Beam" tutorial.

Preparation

1. Open Gambit
    a. If you are in the CADE lab type "gambit –driver x11" into the command window.

Create Geometry

Step 1: Create Vertices

1. Create a vertex by selecting the command buttons in the following order.

   GEOMETRY  **→ VERTEX**  **→ CREATE VERTEX** 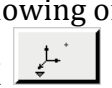

   a. Enter the coordinates for a vertex at (-1000,0,0) and click the **Apply** button.

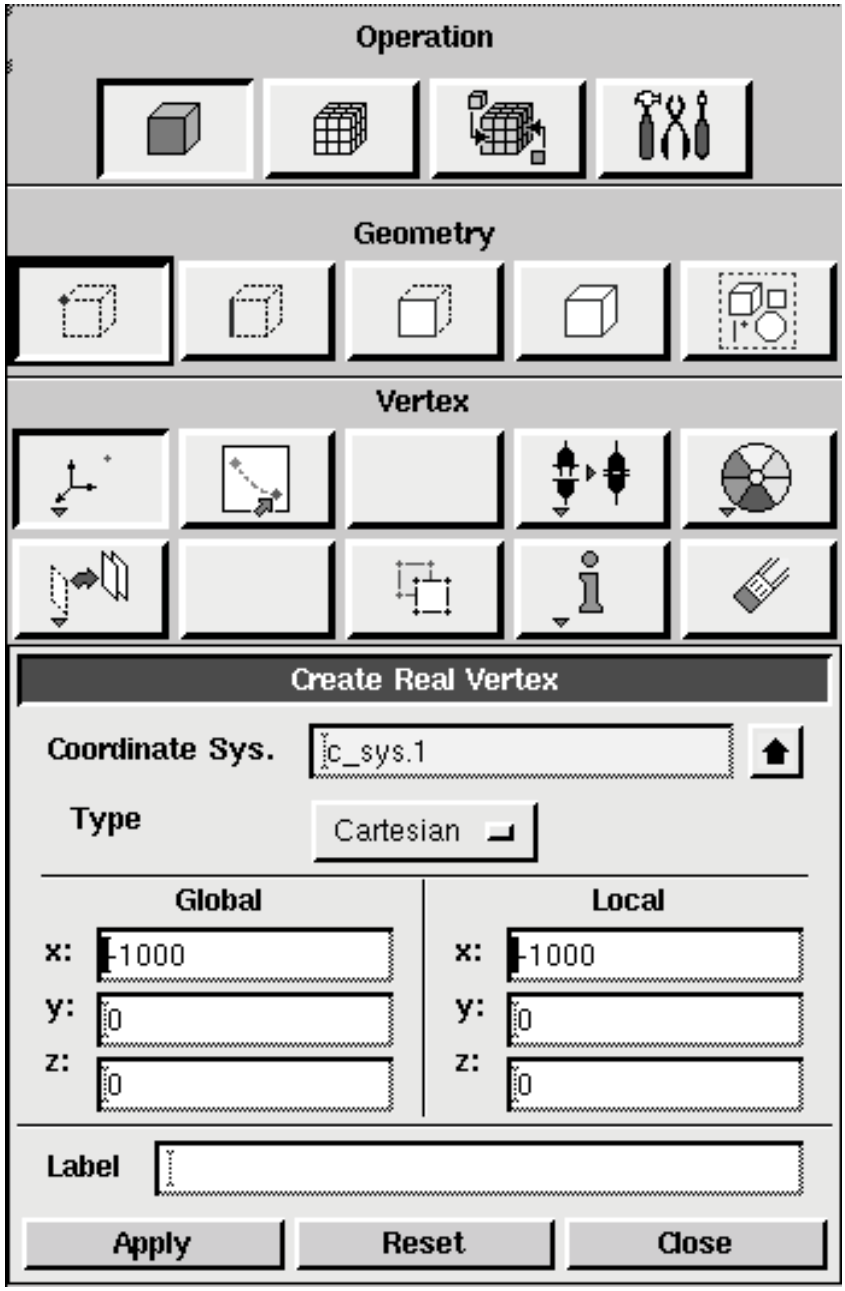

2. Create all of the vertices in the table below.

Vertex	x(mm)	y(mm)	z(mm)
1	-1000	0	0
2	-1000	500	0
3	1000	500	0
4	1000	0	0
5	60	0	0
6	60	300	0
7	-60	300	0
8	-60	0	0
9	-0.79375	0	0
10	-0.79375	200	0
11	0.79375	200	0
12	0.79375	0	0

Click the **Fit To Window**  command button to view all vertices.

Step 2: Create Edges

2. Create an edge by selecting the command buttons in the following order.

   GEOMETRY  **→ EDGE**  **→ CREATE EDGE** 

   a. Click on the Black Arrow next to the yellow selection box to choose vertices.

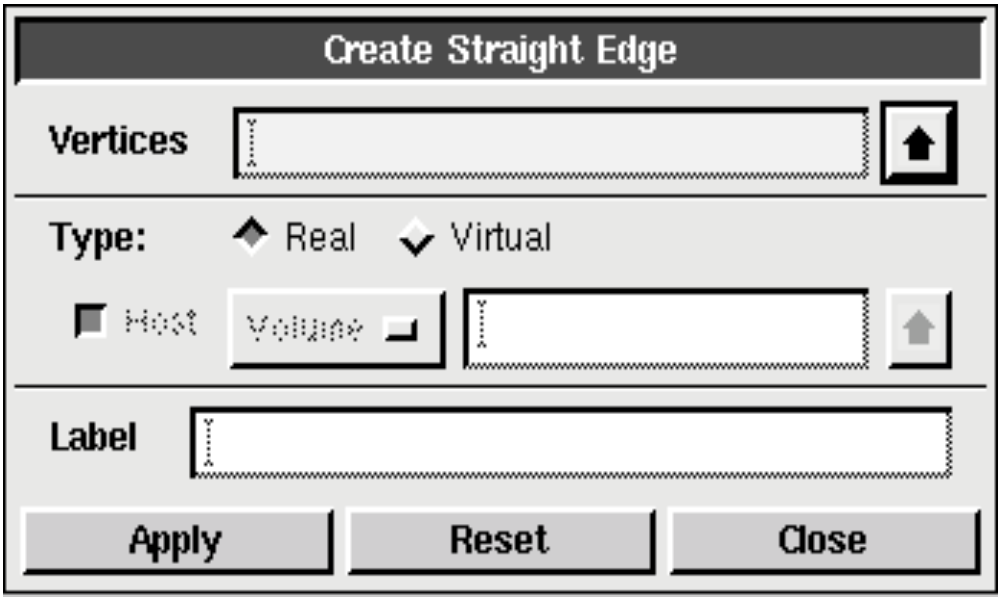

   b. Select vertex.1 and vertex.2 from the **Vertex List** and click the **Apply** button.

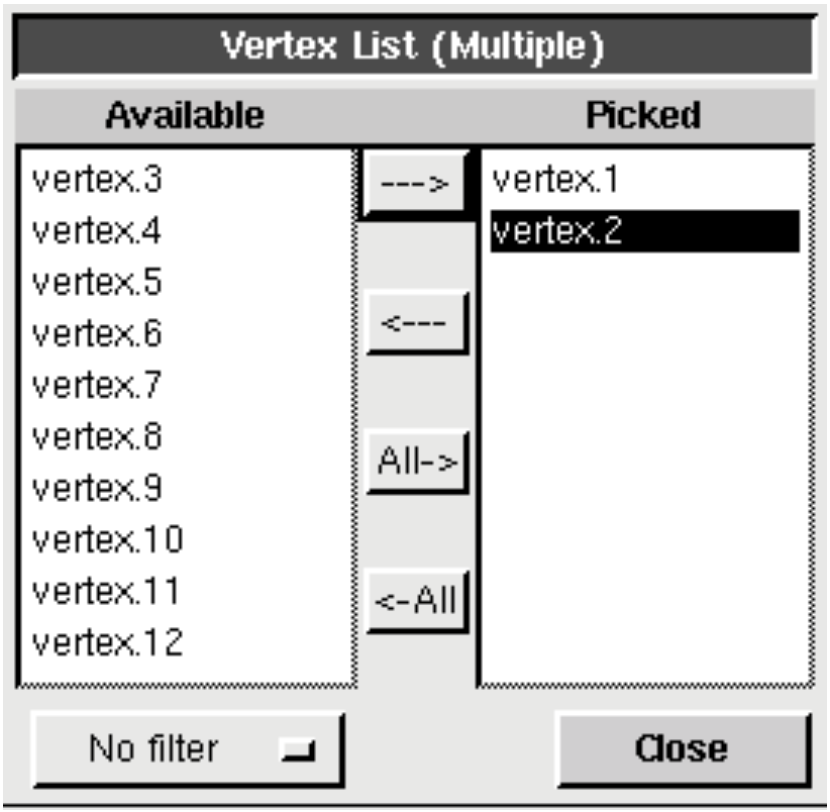

3. Create all 13 edges in the table below.

Edge	Vertex 1	Vertex 2
1	1	2
2	2	3
3	3	4
4	4	5
5	5	6
6	6	7
7	7	8
8	8	1
9	8	9
10	9	10
11	10	11
12	11	12
13	12	5

1. View all edges.
2. Close the edges window

Step 3: Create Faces

1. Create a face by selecting the command buttons in the following order.

   GEOMETRY  **→ FACE**  **→ FORM FACE** 

   a. Click on the Black Arrow next to the yellow selection box to choose edges.

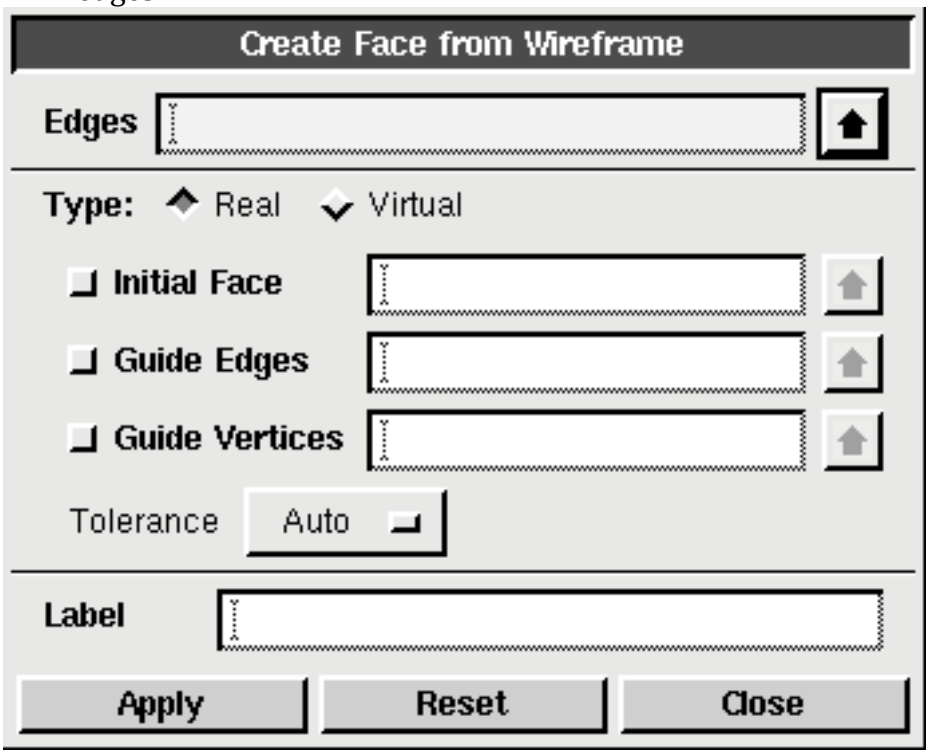

Select edges.1 through edge.8 from the **Edge List** and click **Apply**.

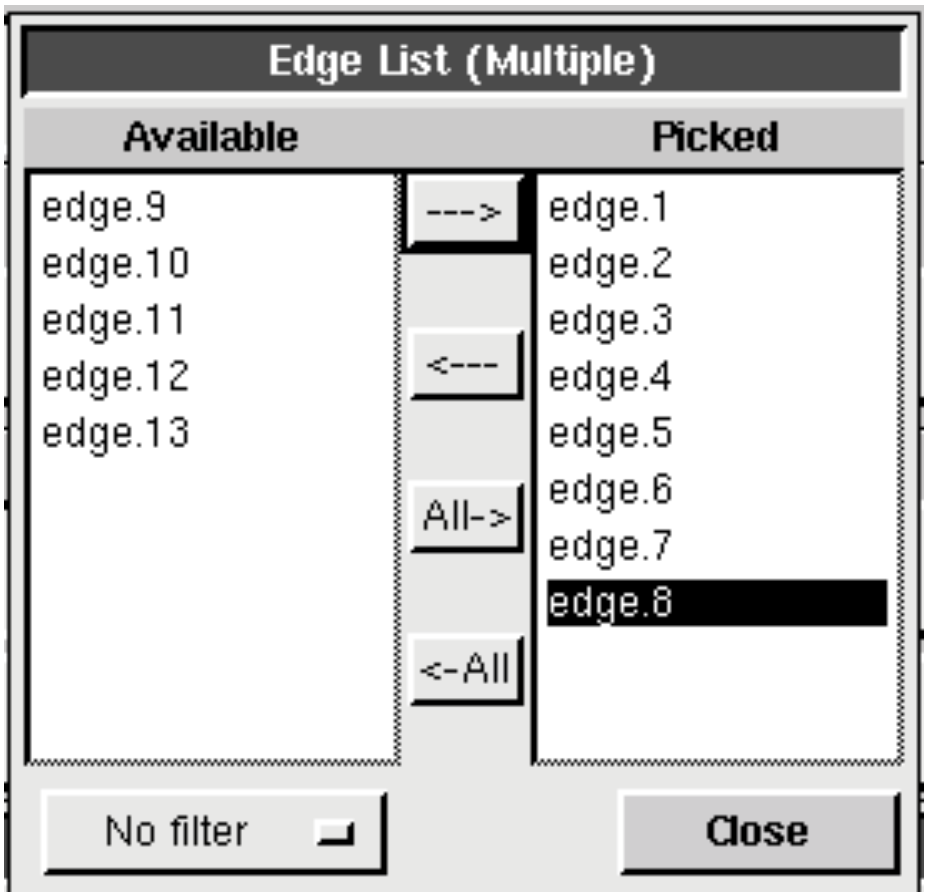

1. Create a second face by selecting edge.5 through edge.7 and edge.9 through edge.13
2. Save your work.
3. Create Mesh

Step 1: Specify Nodes on the Beam

1. Specify Nodes on an edge by selecting the command buttons in the following order.

   MESH  **→ EDGE**  **→ MESH EDGE** 

   a. Click on the Black Arrow next to the yellow selection box to choose edges.

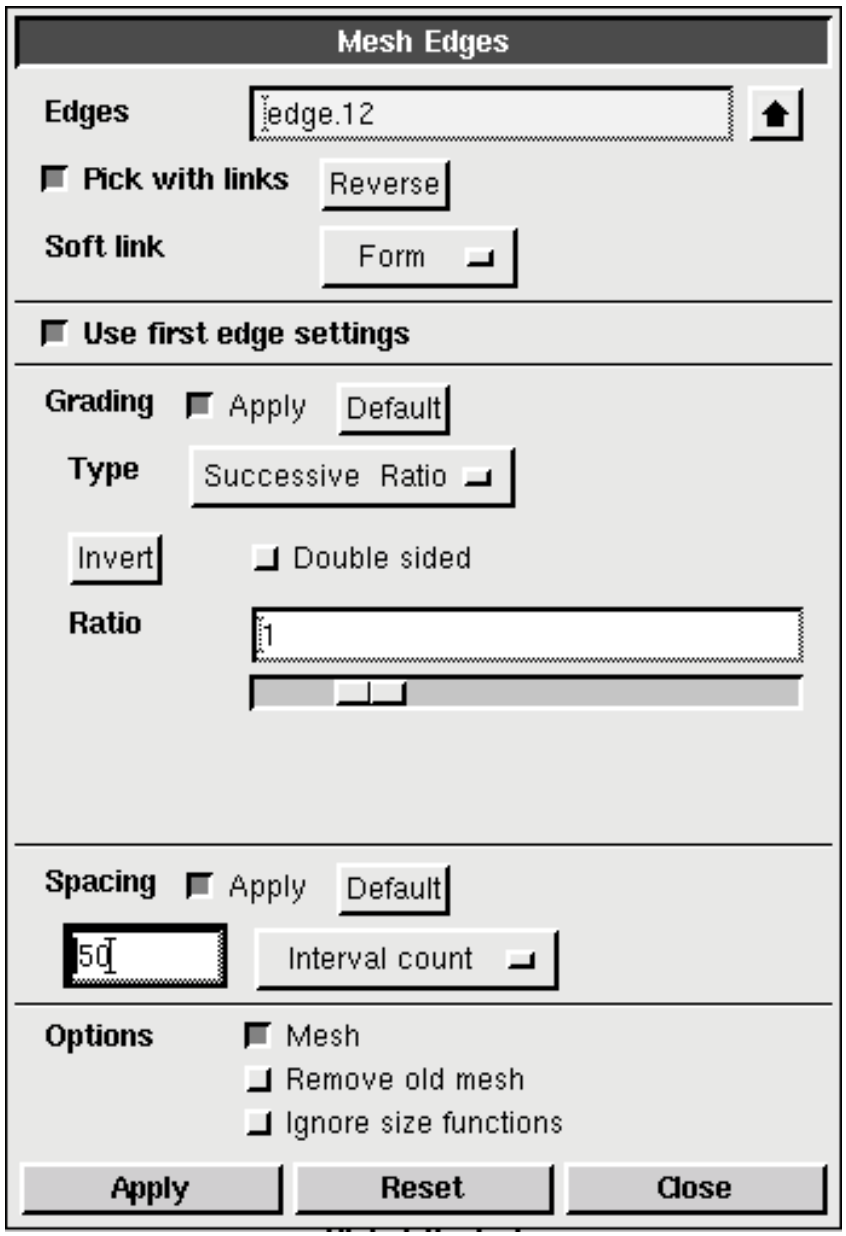

i. In the **Edge List** select edge.10 and edge.12.
ii. In the **Spacing** sub menu choose **Interval count** from the drop down menu.
iii. Enter 50 for the spacing and click the **Apply** button.

b. Select edge 11 from the **Edge List**
   i. Enter 1 for the spacing and click the **Apply** button.

Step 2: Specify Nodes Along The Deforming Domain Edges

1. Select Edges 5 and 7 From the **Edge List**.
   a. Enter 25 for the spacing and click the **Apply** button.
2. Select edge.6 from the Edge List.
   a. Enter 10 for the spacing and click the **Apply** button.
3. Select edge.9 and edge.13 from the **Edge List**

a. Enter 7 for the spacing and click the **Apply** button.

Step 3: Create Mesh For The Deforming Domain

1. Create a mesh for a face by selecting the command buttons in the following order.

MESH  **→ FACE**  **→ MESH FACES** 

a. Click on the Black Arrow next to the yellow selection box.

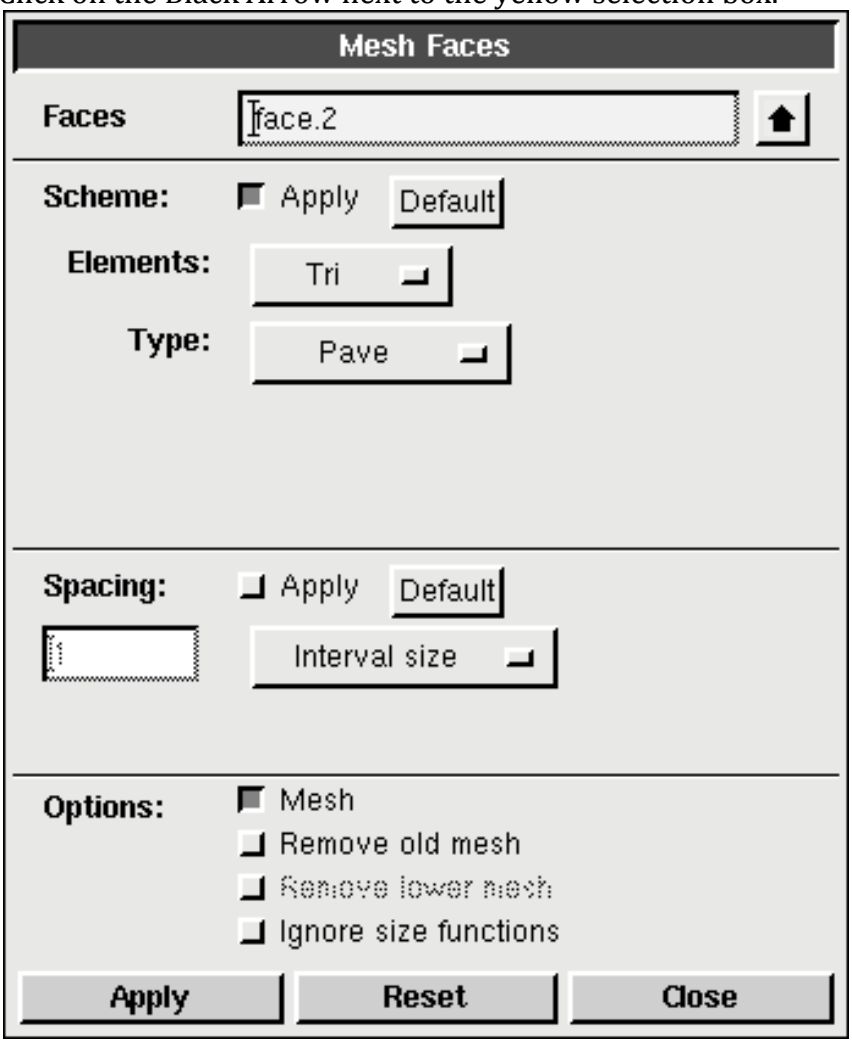

b. Select face.2 from the **Face List**.
c. Select **Tri** from the **Elements** drop down list.
d. Select **Pave** from the **Type** drop down list.
e. In the **Spacing** sub menu unselect the **Apply** option.
f. Click the **Apply** button.

Step 4: Specify Nodes Along the Stationary Domain Edges.

MESH  **→ EDGE**  **→ MESH EDGE** 

1. Select edge.1 through edge.4 and edge.8 from the **edges list**
   a. In the **Spacing** sub menu select **Interval size** from the drop down list.
   b. Enter 25 in for the spacing and click the **Apply** button.

Step 5: Create Mesh For the Stationary Domain

MESH  **→ FACE**  **→ MESH FACES** 

1. Select face.1 from the **Face List**.
   a. Select **Tri** from the **Elements** drop down list.
   b. Select **Pave** from the **Type** drop down list.
   c. In the **Spacing** sub menu unselect the **Apply** option.
   d. Click the **Apply** button.
2. Save your work.

Specify Boundaries and Zones

1. Specify boundary types by selecting the command buttons in the following order.

   ZONES  **→ SPECIFY BOUNDARY TYPES** 

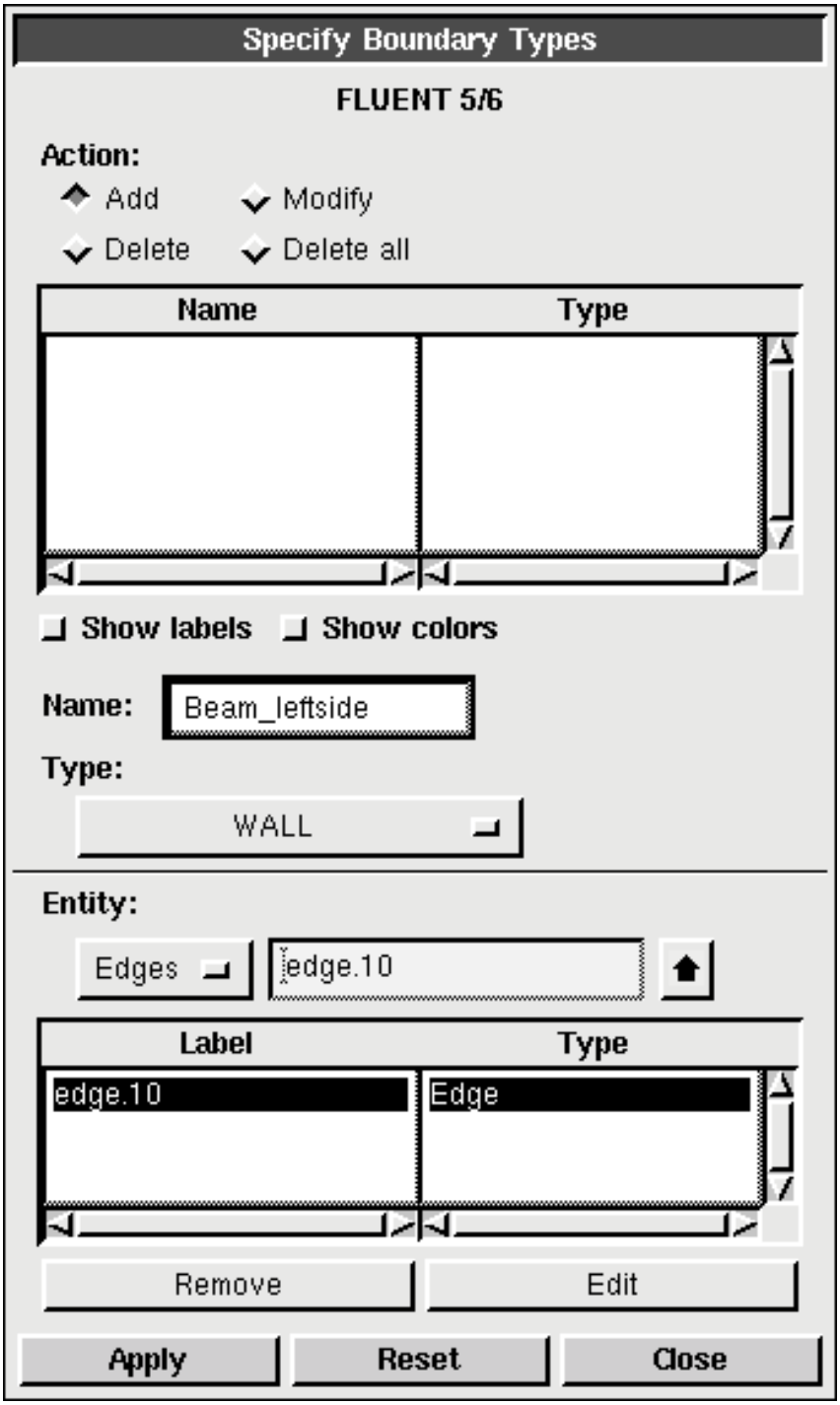

Step1: Specify Boundaries on the Beam.

1. Select edge.10 from the **Edge List**.
   a. Select **WALL** from the **Type** drop down list.
   b. Enter **Beam_leftside** for the name and click the Apply button.
2. Select edge.12 from the **Edge List**.
   a. Select **WALL**from the **Type** drop down list.
   b. Enter **Beam_rigthside** for the name and click the Apply button.

3. Select edge.11 from the **Edge List**.
   a. Select **WALL** from the **Type** drop down list.
   b. Enter **Beam_end** for the name and click the Apply button.

Step 2: Specify Other Boundary Conditions

1. Select edge.1 from the **Edge List**.
   a. Select **VELOCITY INLET** from the Type drop down list.
   b. Enter **Inlet** for the name and click the Apply button.
2. Select edge.2 from the **Edge List**.
   a. Select **SYMMETRY** from the Type drop down list.
   b. Enter **Top** for the name and click the Apply button.
3. Select edge.3 from the **Edge List**.
   a. Select **PRESSURE OUTLET**from the **Type** drop down list.
   b. Enter **Outlet** for the name and click the **Apply** button.
4. Select edge.8 and edge.4 from the **Edge List.**
   a. Select **WALL** from the Type drop down list
   b. Enter **stat_wall** for the name and click the **Apply** button.
5. Select edge.9 and edge.13 and from the **Edge List**.
   a. Select **WALL** from the **Type** drop down list
   b. Enter **def_wall** for the name and click the **Apply** button.

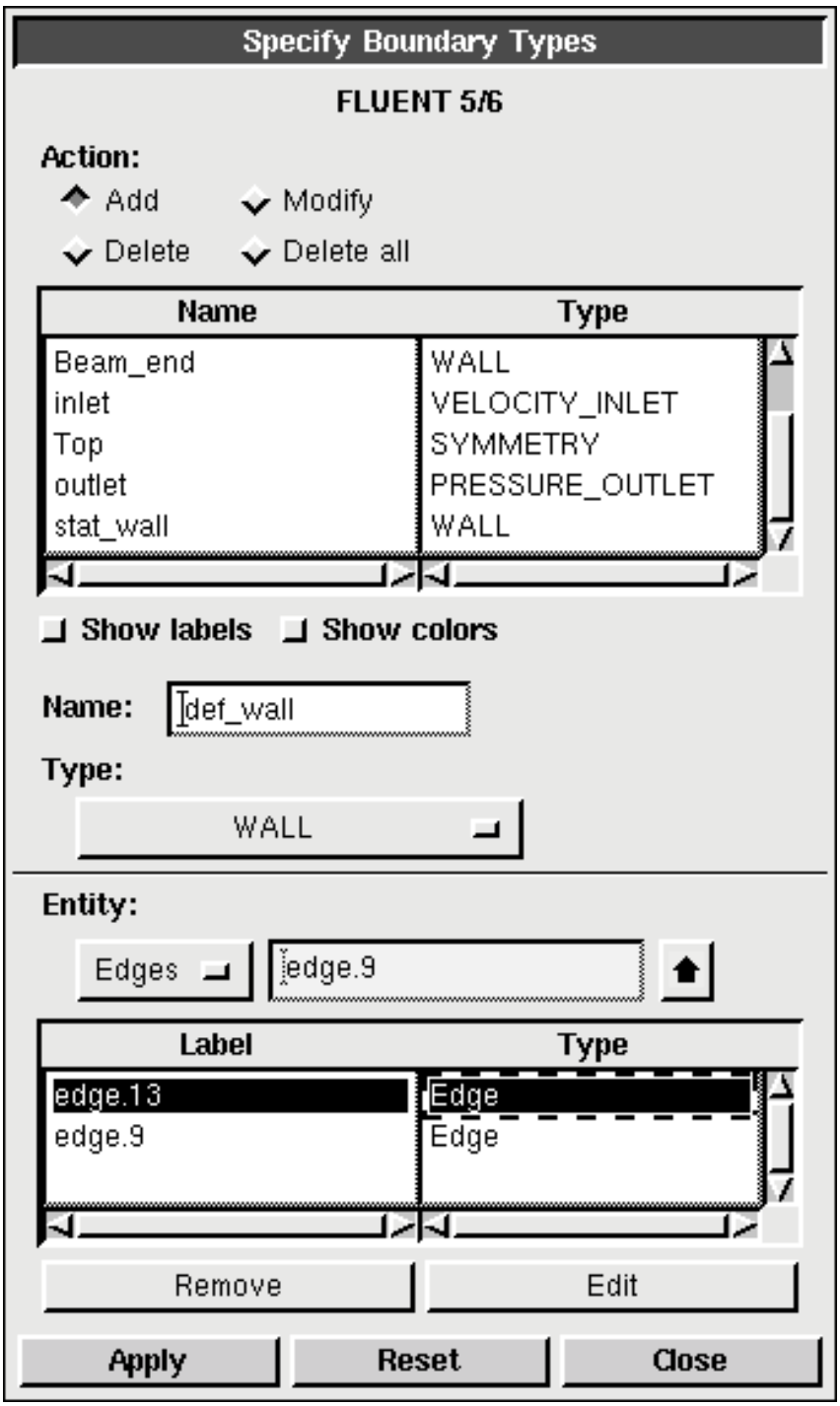

Step 3: Specify Zones

1. Specify Zone by selecting the command buttons in the following order.
2. **ZONES** → **SPECIFY CONTINUUM TYPES**

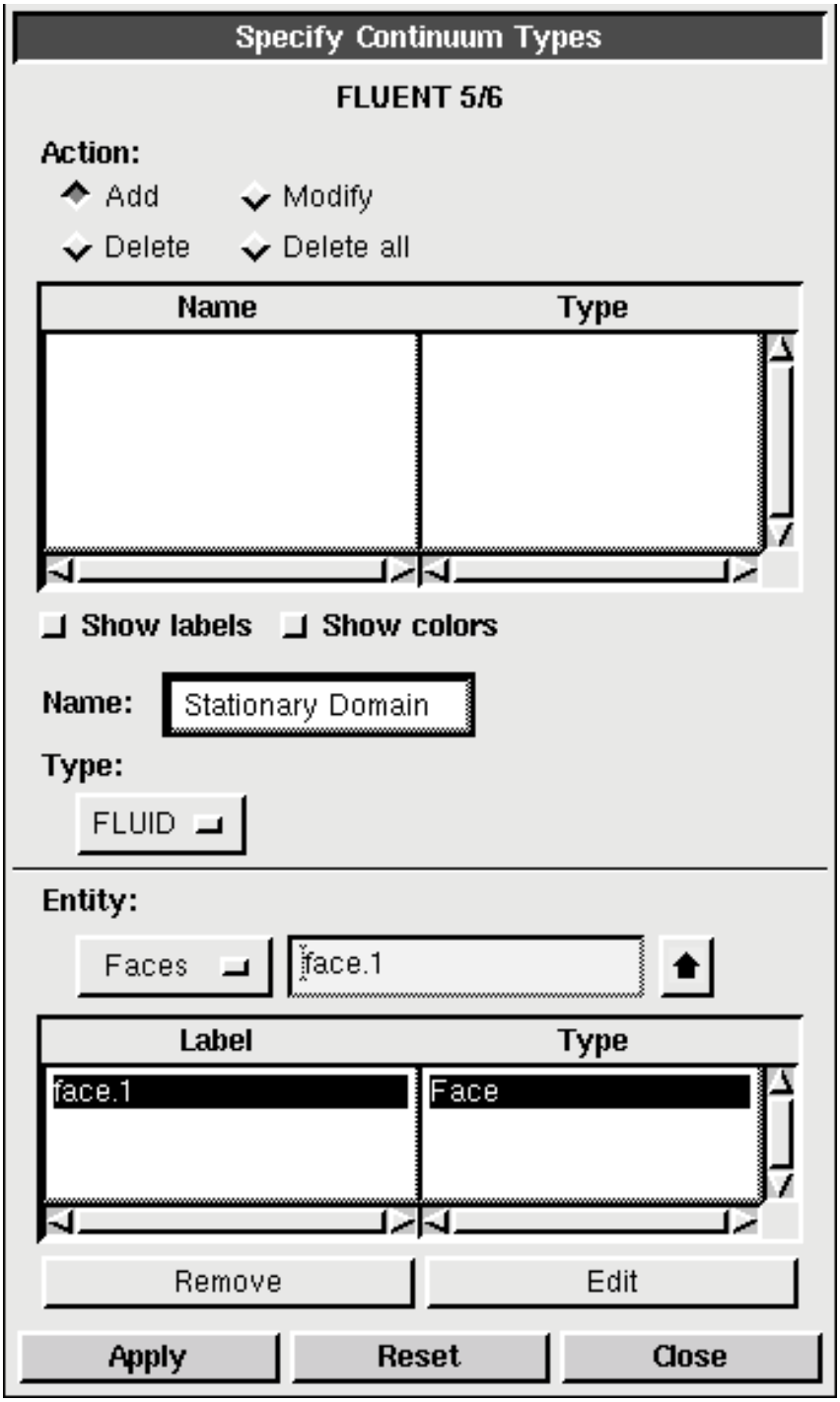

a. Select Face 1 from the Face List.
b. Select **FLUID** from the **Type** drop down list.
c. Enter **Stationary_Domain** for the name and click the **Apply** button.

3. Select Face 2 from the face list.
   a. Select **FLUID** from the **Type** drop down list.
   b. Enter **Deforming_Domain** for the name and click the **Apply** button.

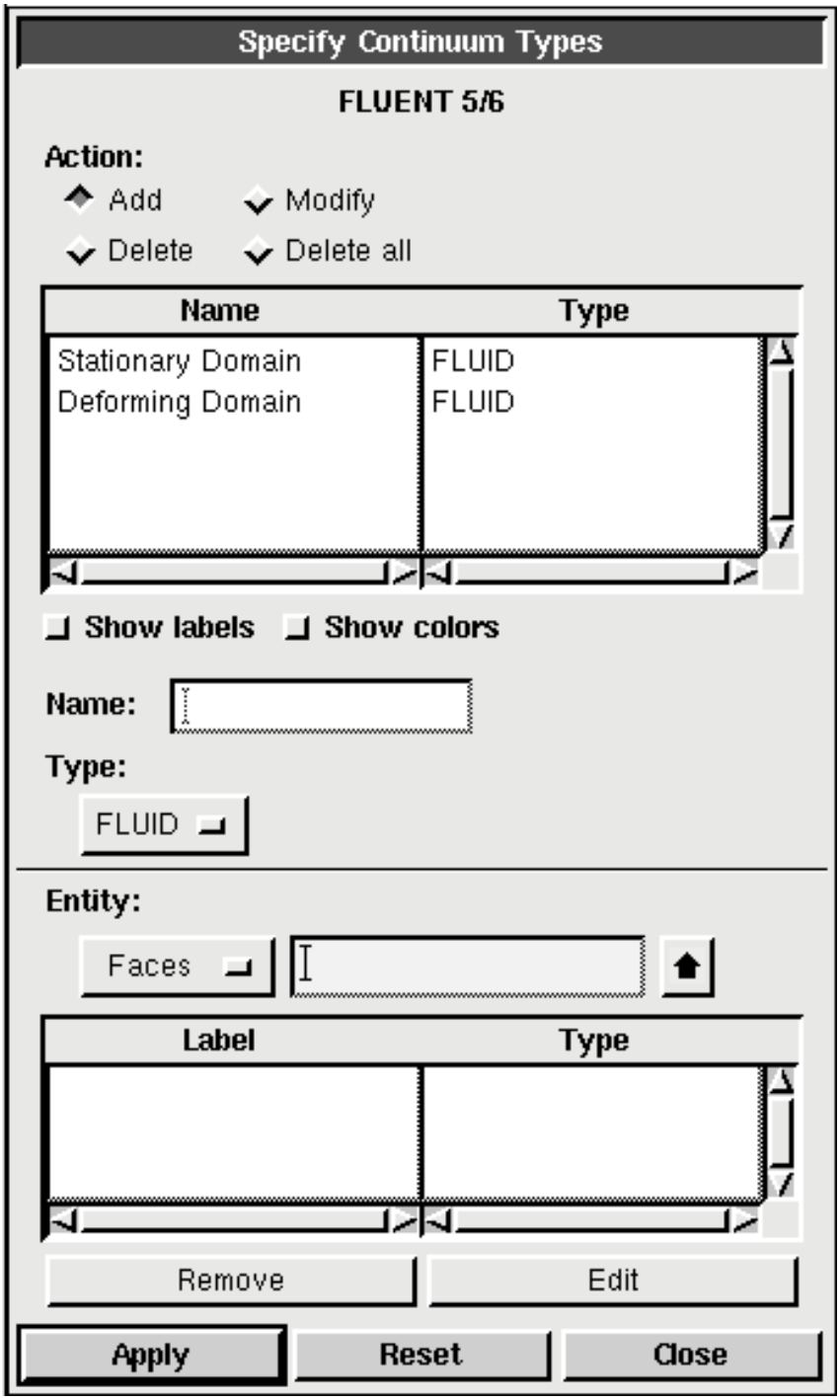

4. Save your work.

Export Mesh

1. **File** → **Export** → **Mesh**…
2. Select the Export 2-D (X-Y) Mesh option.

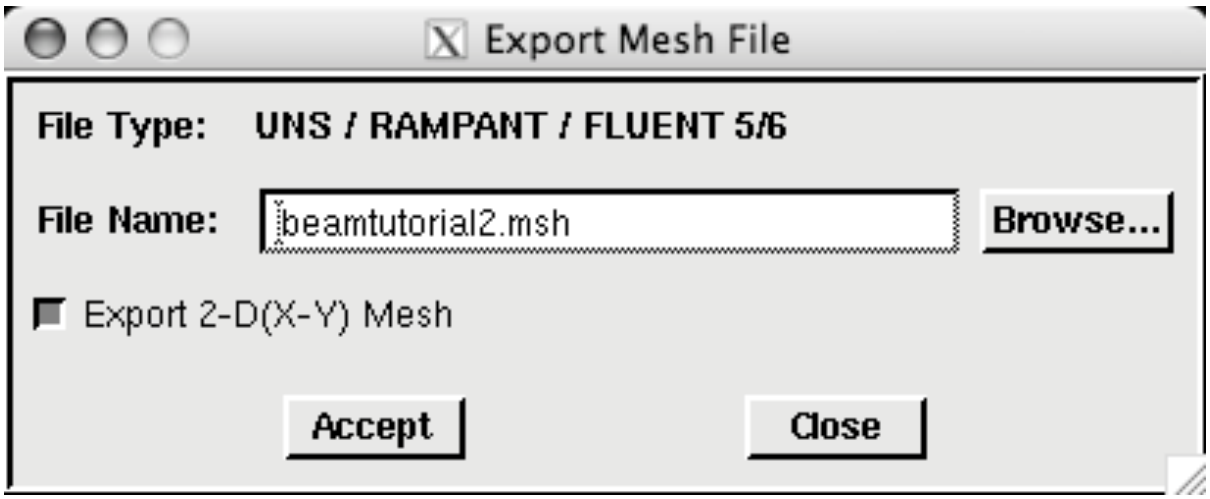

3. Click **Accept**.

Conclusion

This Mesh file is ready to import into Fluent for simulation. See beamtutorial.docx for directions UDF and dynamic mesh instructions.

Schematics

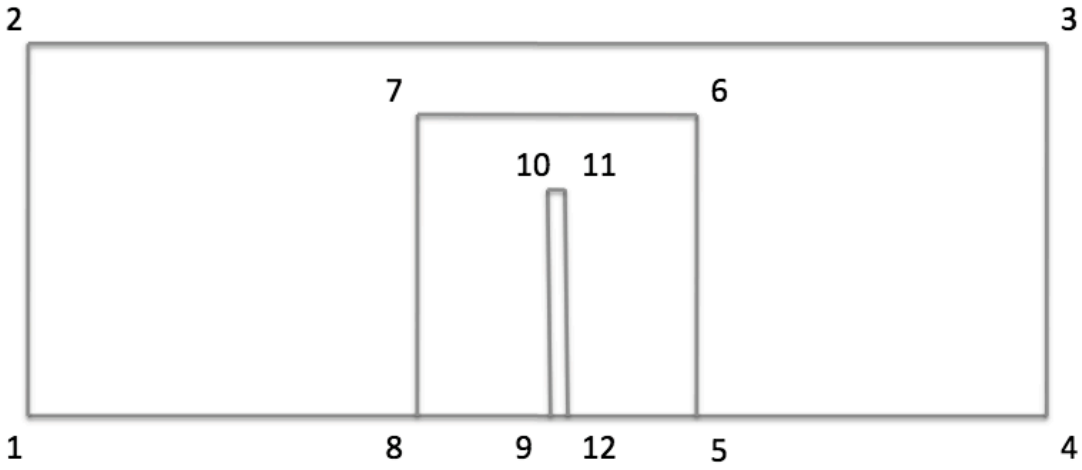

Node Numbers

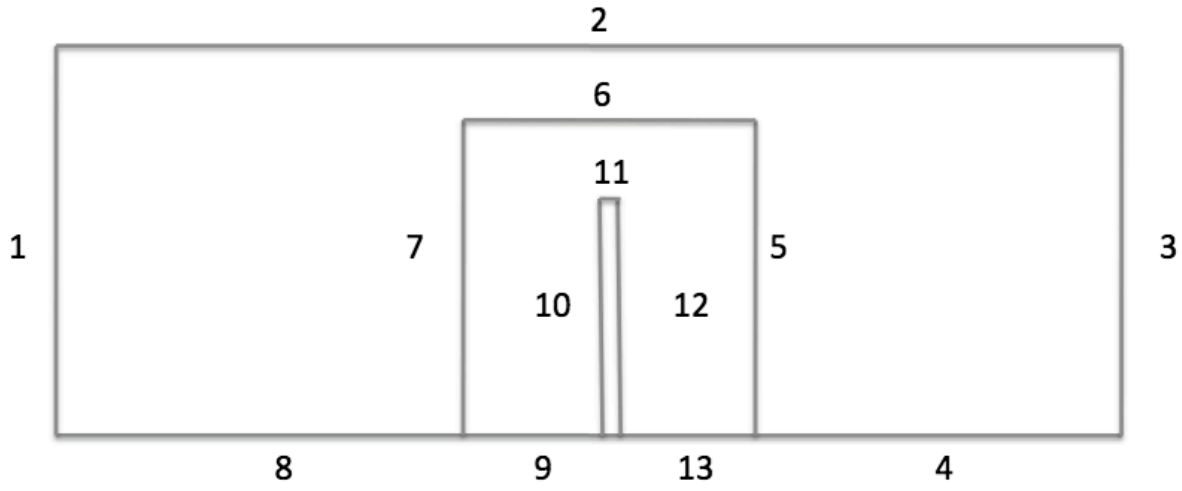

Edge Numbers

Fluid Structure Interaction: Cantilever Beam

Introduction

The purpose of this tutorial is to introduce and demonstrate the use of User Defined Functions (UDFs) for simple Fluid Structure Interaction.

This tutorial demonstrates the following:

- Read an exiting mesh file in FLUENT.
- Verify the grid for dimensions and quality.
- Add a new material from materials database.
- Define solver settings.
- Define dynamic mesh properties.
- Define dynamic mesh zones.
- Write a simple UDF file.
- Compile a UDF.
- Visualize the fluid structure interaction.

Prerequisites

This tutorial assumes that you have some experience with FLUENT and have some familiarity with the interface. It also assumes no experience with UDFs.

Problem Description

Consider a thin aluminum plate placed in a water channel perpendicular to the flow. The plate spans the entire width of the water channel but its ends are free from the walls to allow for it to deflect due to the forces caused by the on coming flow. The water channel width is 1m. This will allow us to solve the problem with a 2d solver because the assumed depth is one meter. The sheet of aluminum is 1/16" thick. See figure 1 for a schematic of the problem.

This tutorial assumes you are working in the CADE lab. If you are working in the Engman lab you will be prompted to choose your working directory. Also there are problems in the Windows lab when you get to Step 6 when you compile the UDF. I recommend doing everything from step 6 onward in the CADE lab.

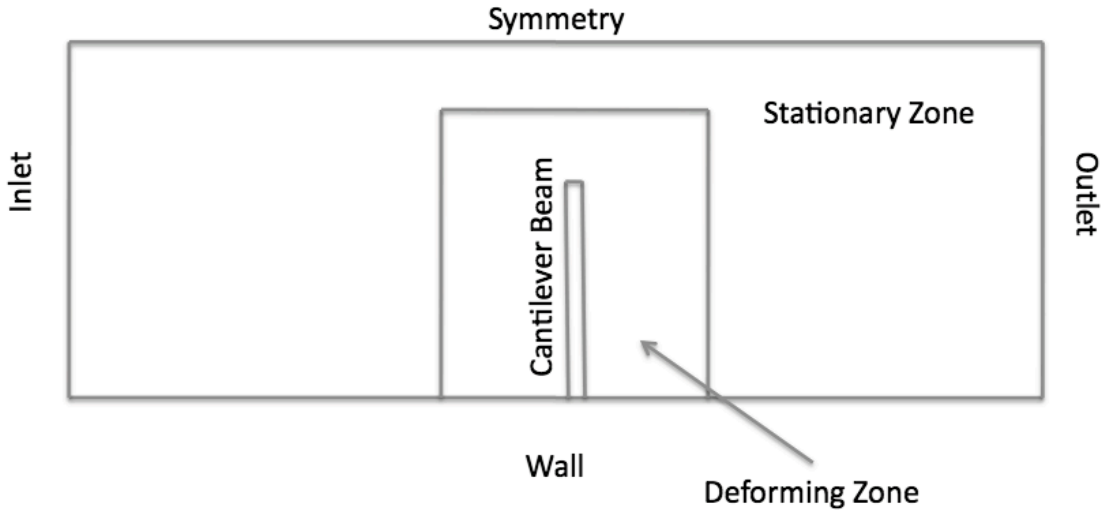

Schematic

Preparation

1. Copy the files beamtutorial.msh and beamUDF.c to your working folder.
2. Start the 2d solver of Fluent
    a. If you are in the CADE lab type “fluent 2d –driver x11” into the command window
3. Create a folder called tiff_files in your working directory.

Setup and Solution

Step 1: Grid

1. Read the grid file beamtutorial.msh

File → **Read** → **Case**…

FLUENT will read the mesh file and report the progress in the console.

2. Check the grid

Grid → **Check**

This procedure checks the integrity of the mesh. Make sure the reported minimum volume is a positive number.

3. Scale the grid

Grid → **Scale**…

   a. This grid was created in mm so under the scroll menu **Grid Was Created In** choose **mm** and click **Scale**. Be sure to only press scale once. To unscale press "Unscale."
   b. Close the **Scale Grid** panel.

4. Display the grid

Display → **Grid**…

   a. Click **Display**
   b. Close the **Grid Display** panel.

Step 2: Models

1. Modify solver settings.

Define → **Models** → **Solver**…

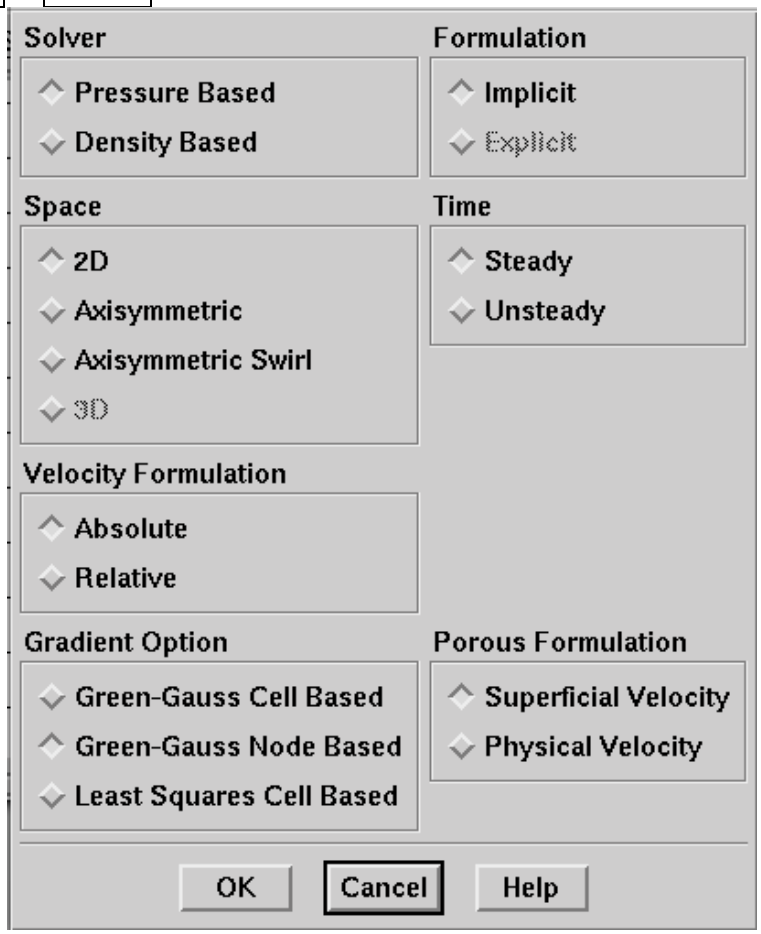

   a. Use the **Green-Gauss Node Based** Gradient option.

Later we will change solver to unsteady for fluid structure interaction.

2. Use the laminar model

Define → **Models** → **Viscous**…

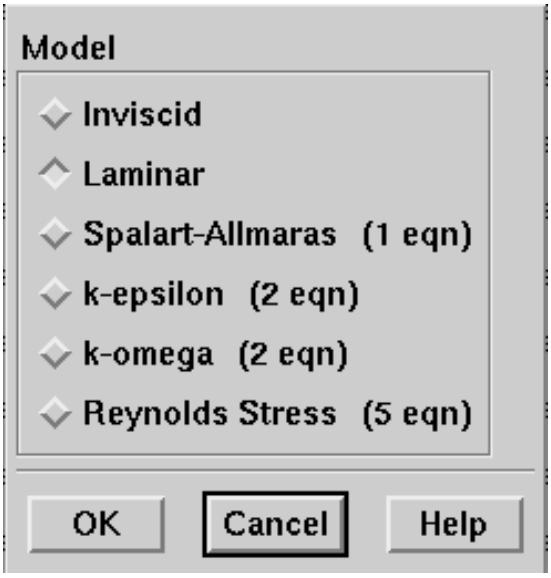

a. Use laminar model.

Step 3: Materials

1. Copy water-liquid ($h2_0$ <l>) from the FLUENT data base
Define → **Materials**…

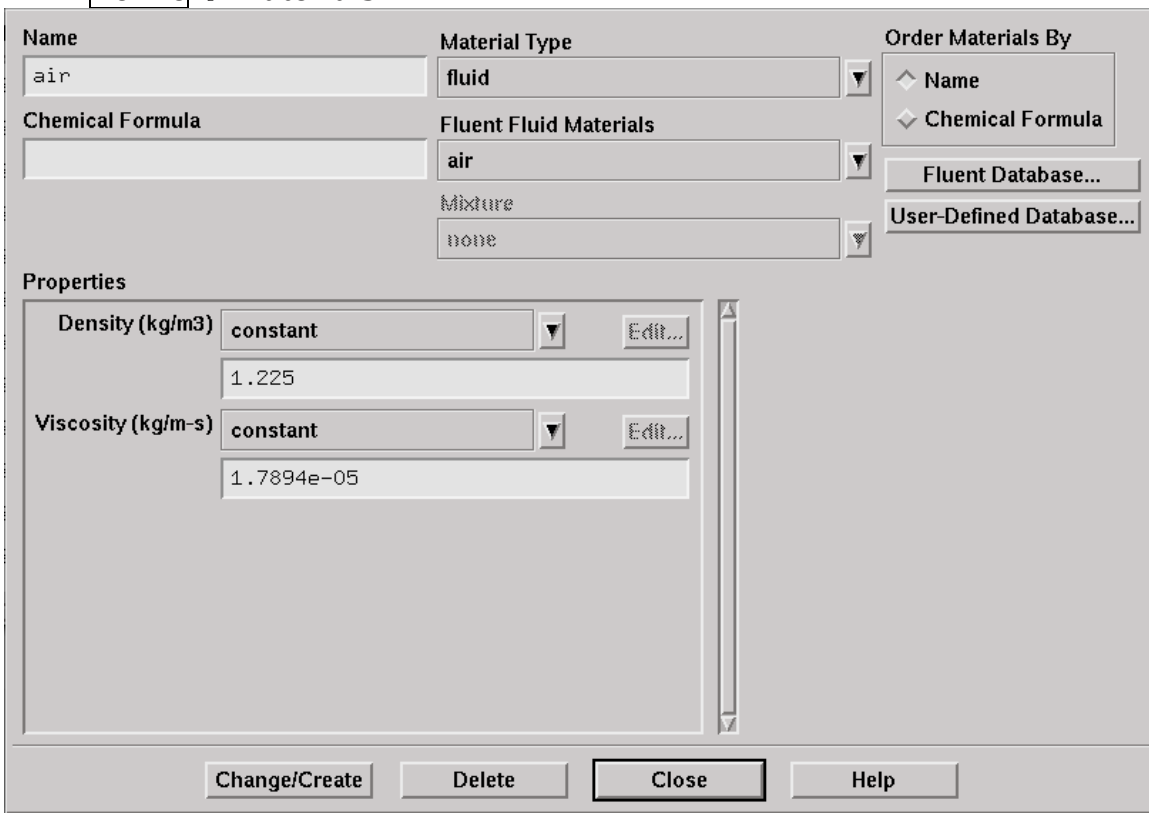

a. Click the **Fluent Database**… button to open the **Fluent Database Materials** panel

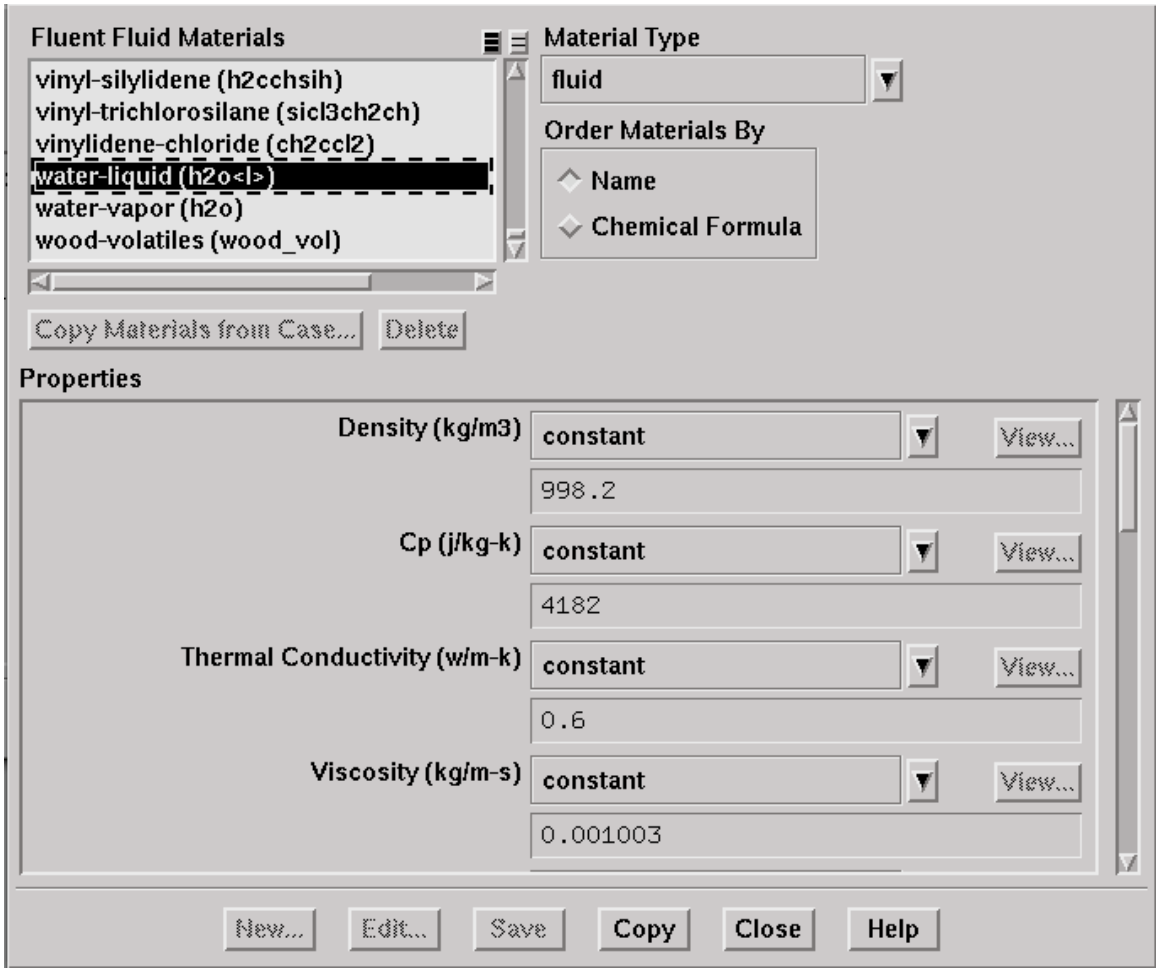

i. Select water-liquid (h2o <l>) from the **Fluent Fluid Materials** selection list.
This will display the default settings for water-liquid.

ii. Click **Copy** and **Close** the **Fluent Database Materials** panel.
The **Materials** *panel will now display the copied information of the water.*

b. Click **Change/Create** and close the **Materials** panel.

Step 4: Boundary Conditions

1. Set the boundary conditions for fluid

Define → **Boundary Conditions**…

a. Select **deforming_domain** from the **Zone** selection list
The **Type** *will be reported as fluid*.

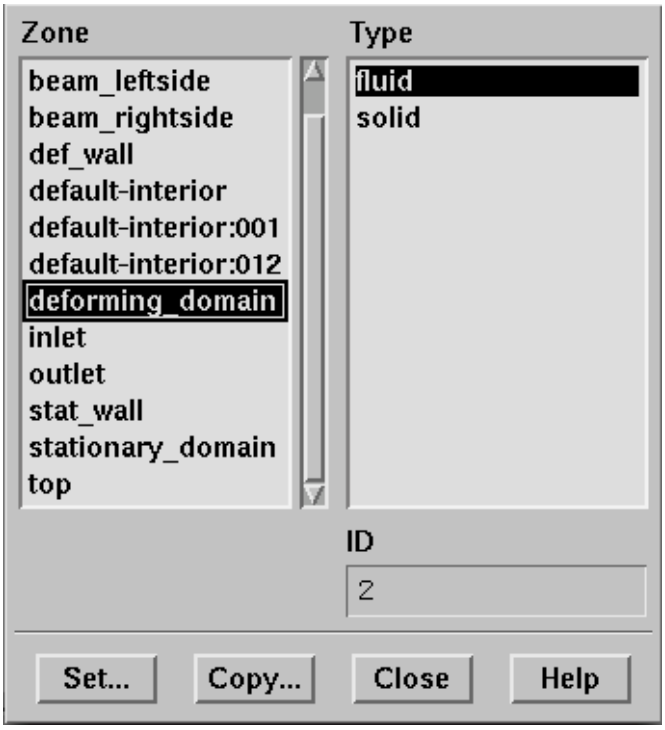

b. Click **Set...** button to open the **Fluid** panel

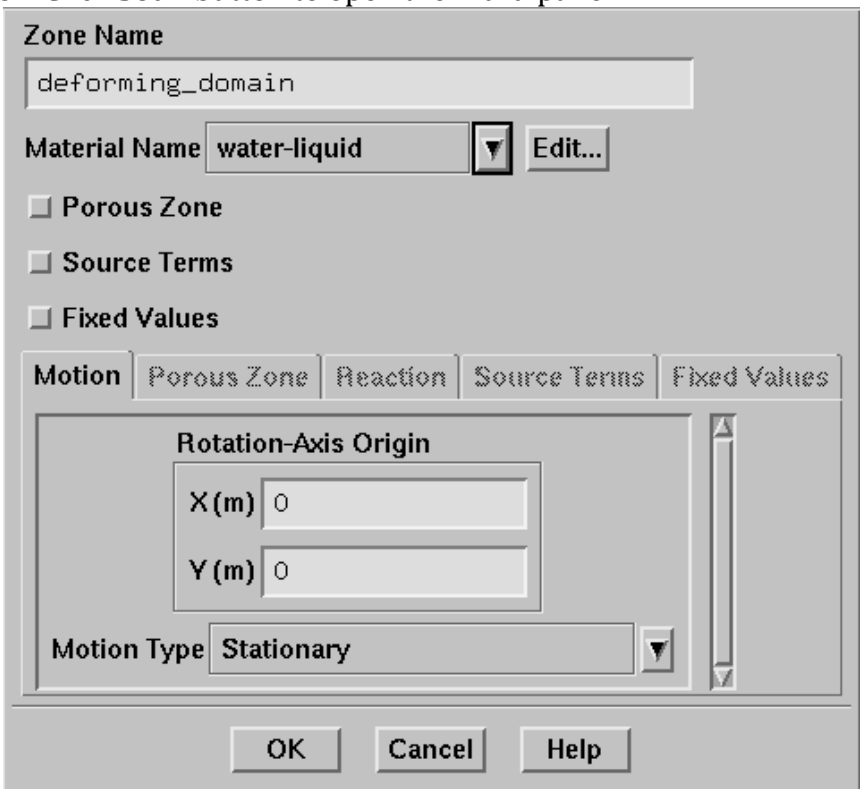

i. Select **water-liquid** from the **Material Name** drop-down list.
ii. Click **OK** to close the **Fluid** panel.

c. Repeat previous step for **stationary_domain**.

2. Set the boundary conditions for the inlet.

a. Select inlet from the **Zone** selection list.
b. Click the **Set**… button to open the **Velocity Inlet** panel.

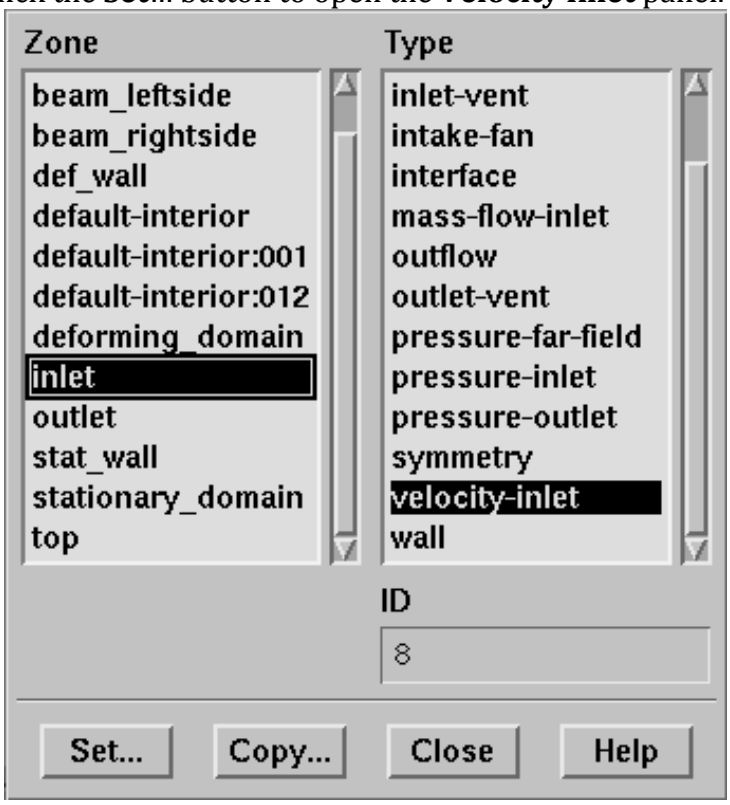

i. Enter 1 m/s for **Velocity Magnitude**.
ii. Click **OK** to close the **Velocity Inlet** panel.

3. Close the **Boundary Conditions** panel.

Step 5: Steady State Solution

1. Set the Solution controls.

Solve → **Controls** → **Solution**…

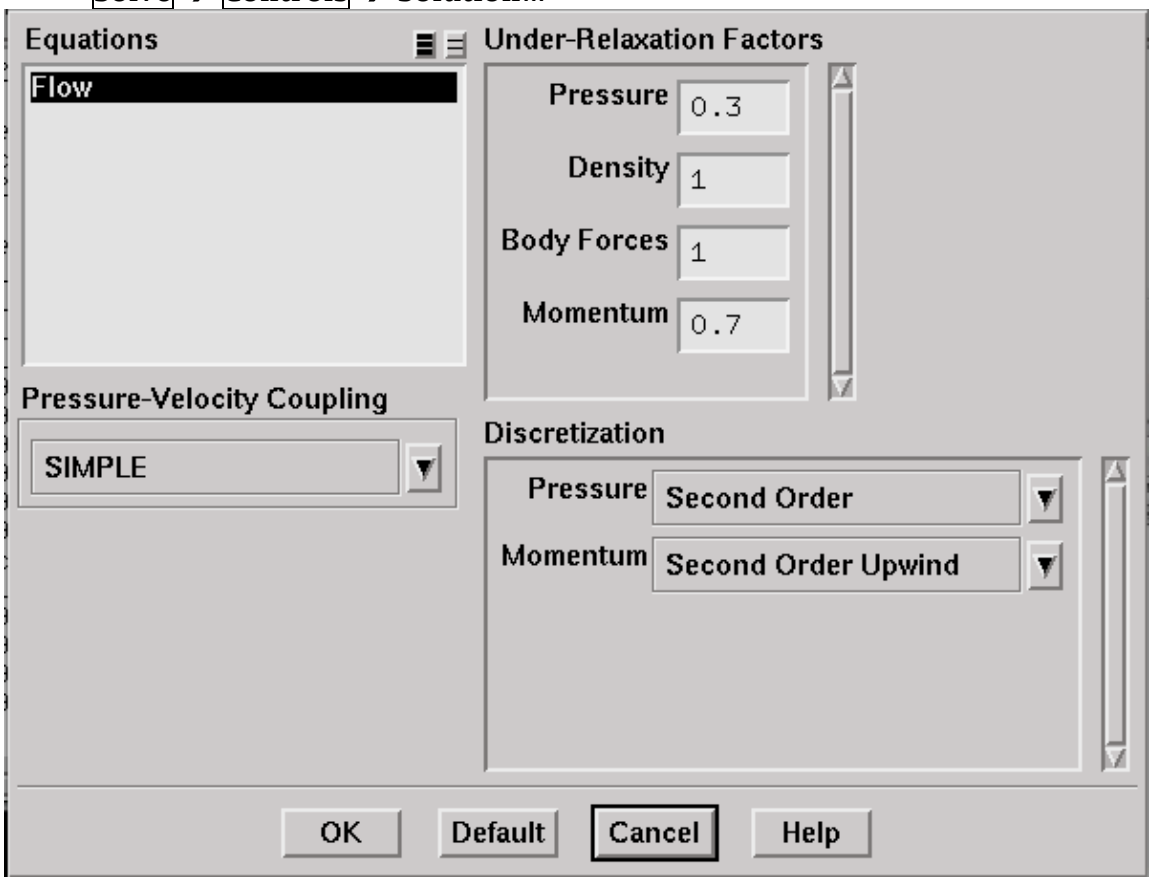

a. Select Second Order from the **Pressure**, and **Momentum** drop-down lists.
b. Click **OK** to close the **Solution Controls** panel.

2. Initialize the flow.

Solve → **Initialize** → **Initialize**…

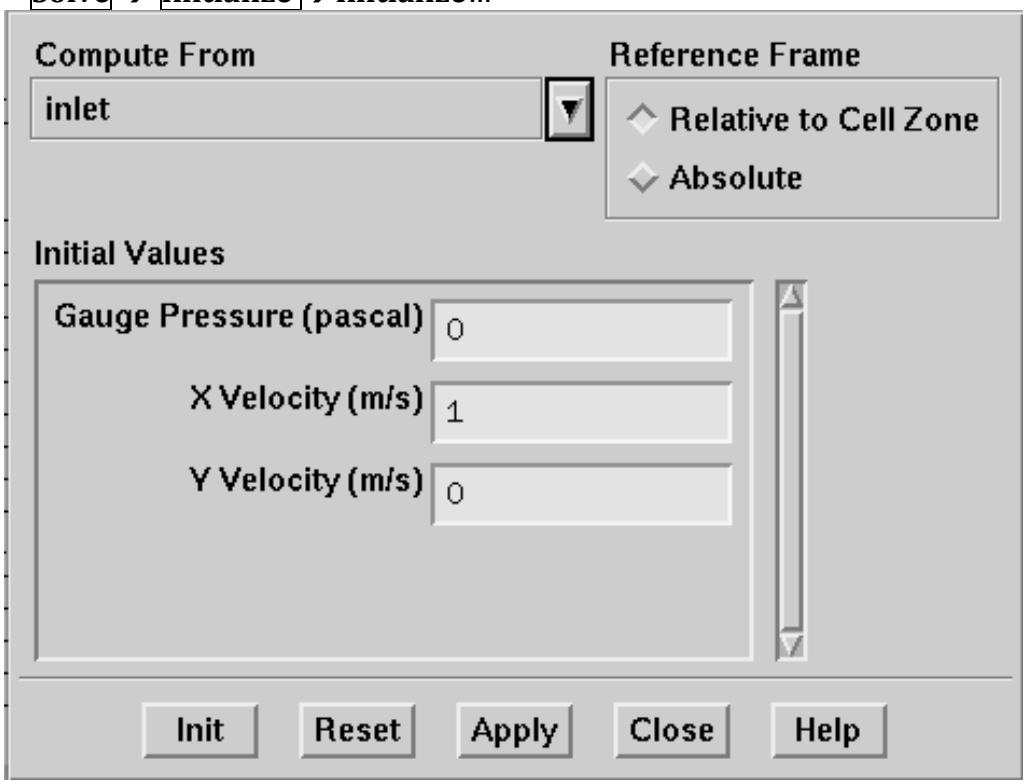

a. Select **inlet** from the **Compute From** drop-down list.
b. Click **Init** and **close** the **Solution Initialization** panel.

3. Enable plotting of residuals during calculation.

Solve → **Monitors** → **Residual**…

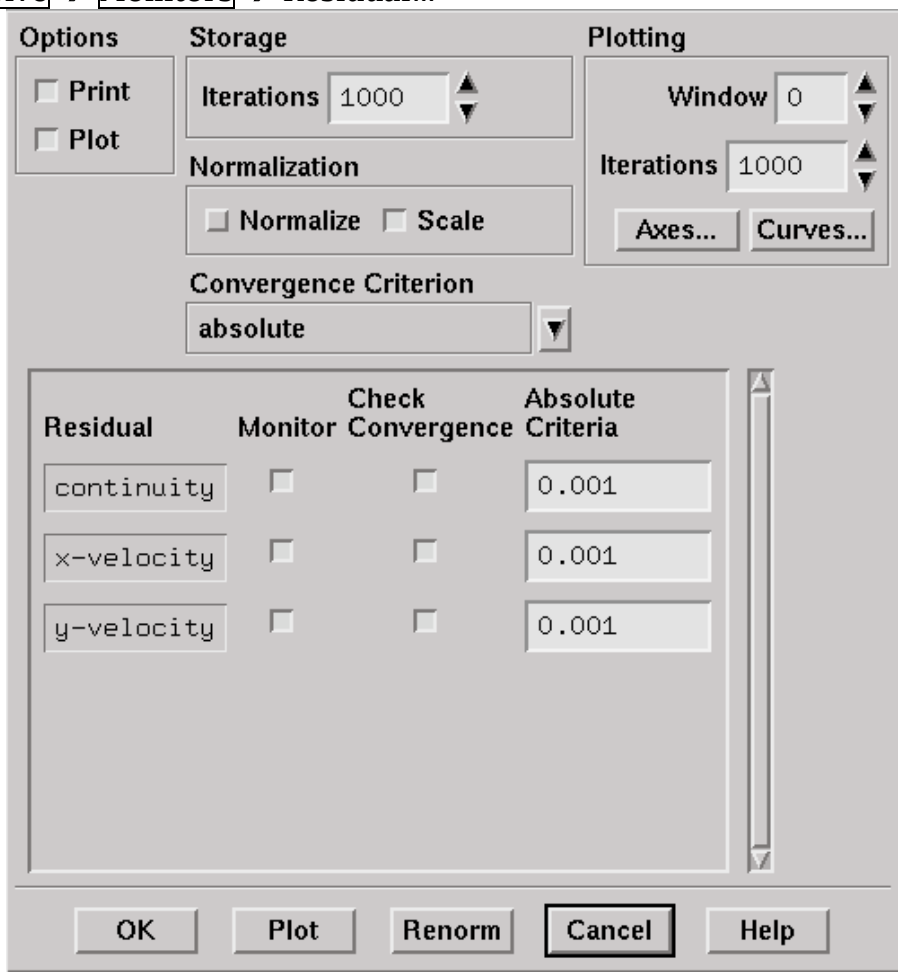

   a. Enable **Plot** in the **Options** group box.
   b. Click **OK** to close the **Residual Monitors** panel.

4. Save the case file (beam.cas.gz).

File → **Write** → **Case**...

Adding ***.gz*** *to the file will save it as a zipped file that will work on both Windows and Linux platforms.*

5. Iterate the solution.

Solve → **Iterate**…

   a. Set **Number of Iterations** to 500.
   b. Click **Iterate** to start the calculation.
   c. Close the **Iterate** panel after iterations are complete.

6. Display filled pressure contours
7. **Display** → **Contours**…

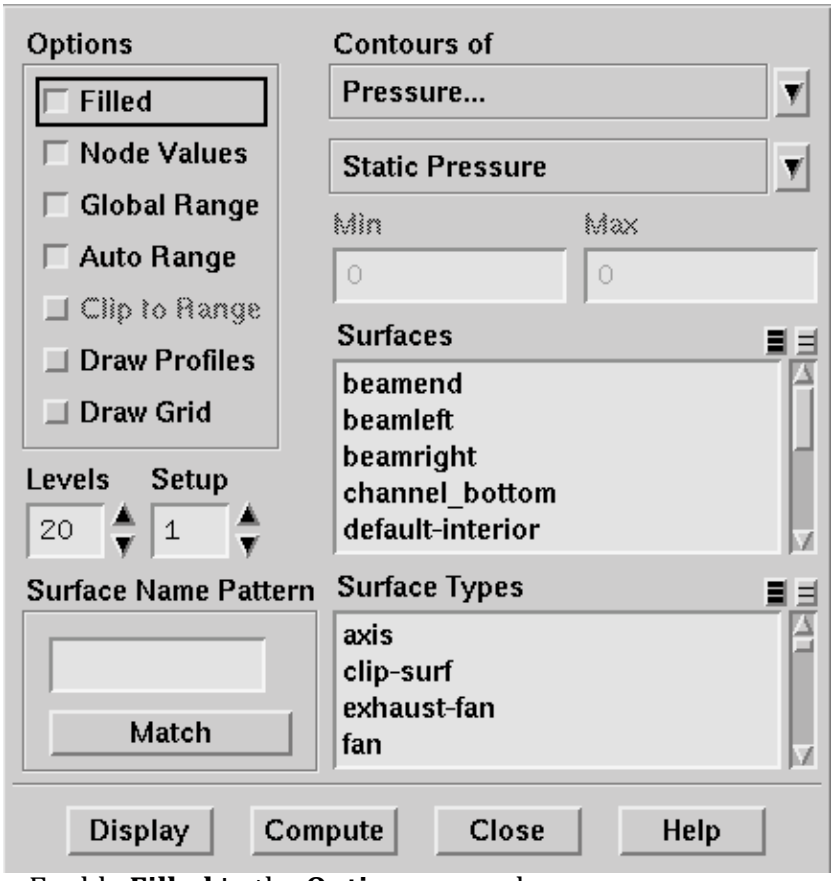

a. Enable **Filled** in the **Options** group box.
b. Click **Display**

c. Close **Contours** panel.

8. Save case and Data file (beam_steady.cas.gz).
File → **Write** → **Case and Data**...

Step 6: Setup Dynamic Mesh

1. Compile UDF.
Define → **User-Defined** → **Functions** → **Compiled**…

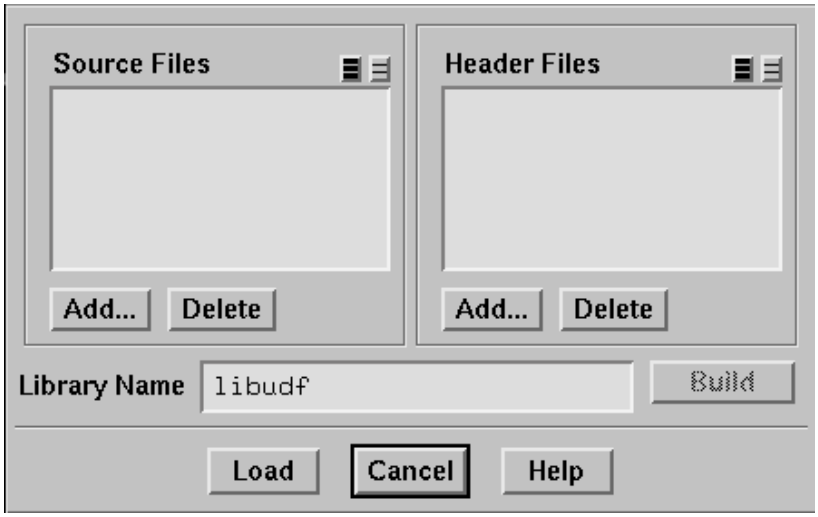

a. Under **Source Files** click **Add.**

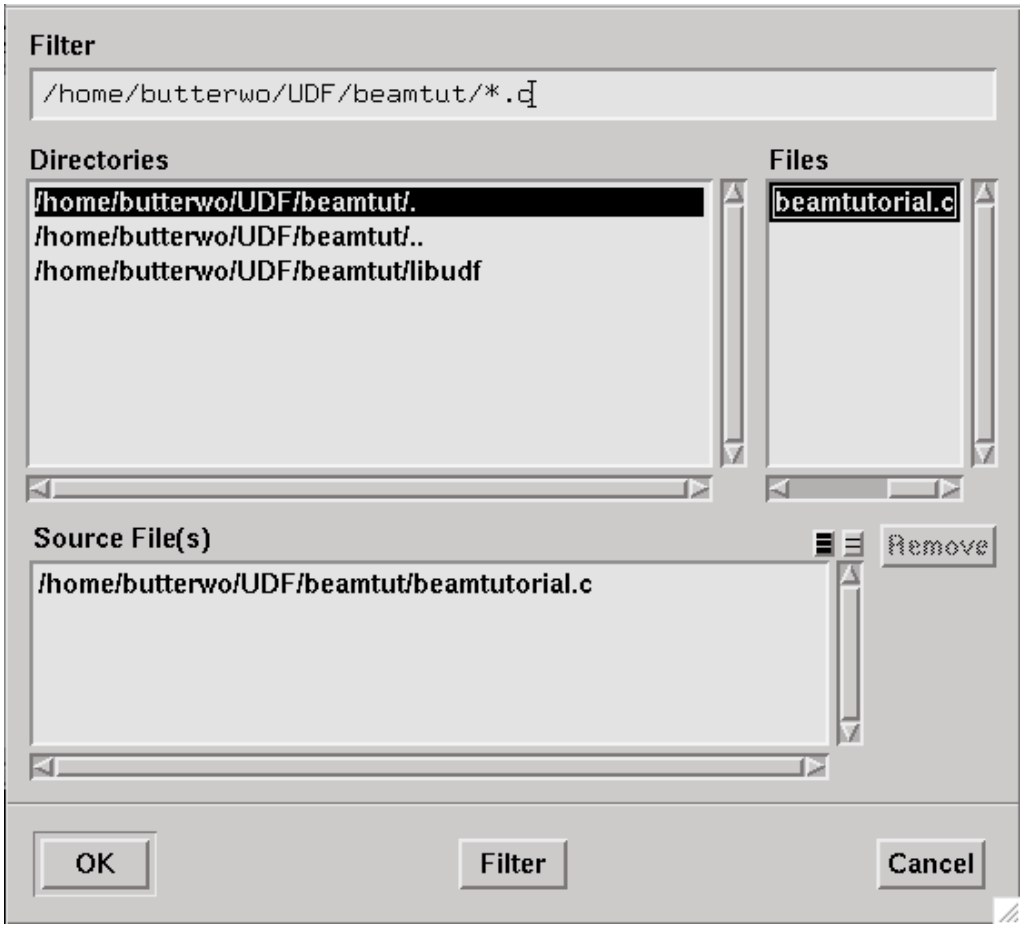

i. Select beamtutorial.c and click **OK**.

b. In the **Compiled UDFs** panel click **Build**
FLUENT *will prompt you to make sure that the source file is in the working directory. Make sure that it is. FLUENT will compile the source code and display the progress on the screen. It may take a few moments.*

c. In the **Compiled UDFs** panel click **Load**.
If you get an error message then there were errors in the source code and the file did not compile.

2. Set dynamic mesh parameter.

Define → **Dynamic Mesh** → **Parameters**…

a. Enable **Dynamic Mesh** from the **Models** List.

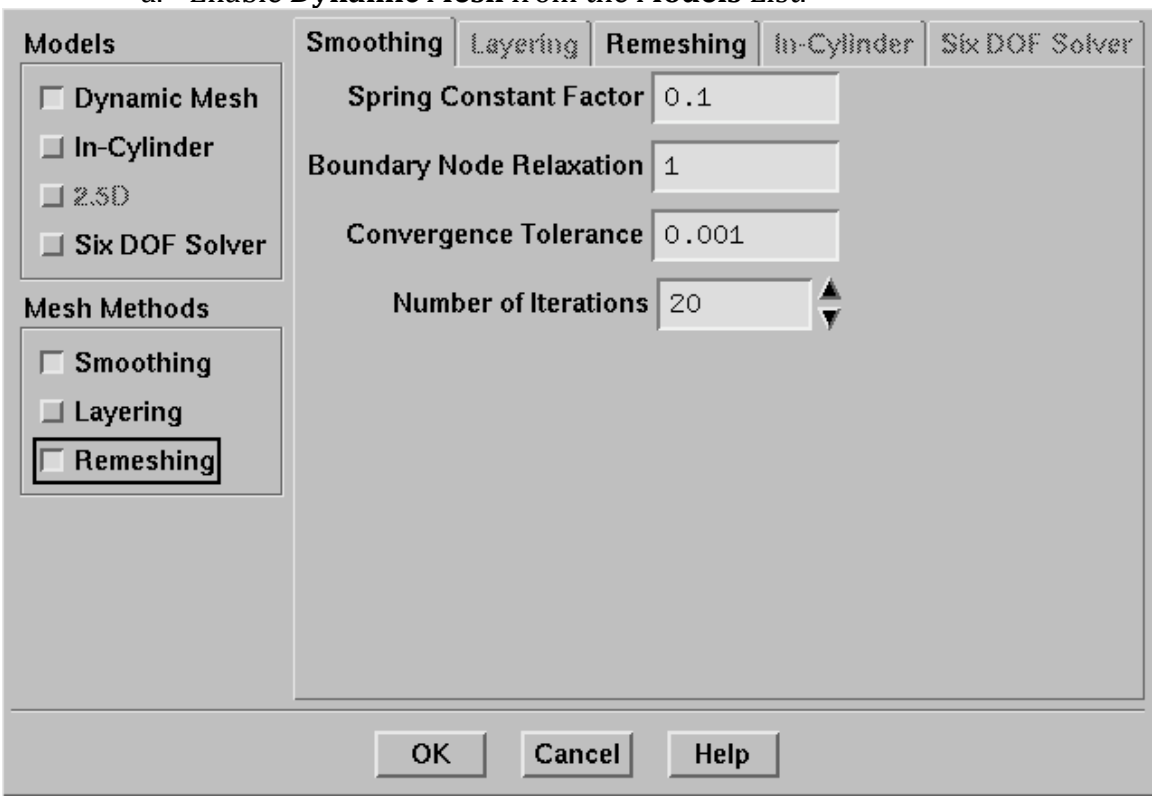

i. Enable **Smoothing** and **Remeshing** from the **Mesh Methods** list.

ii. Enter **0.1** for the **Spring Constant Factor**.

b. Click the Remeshing tab and set the remeshing parameters.

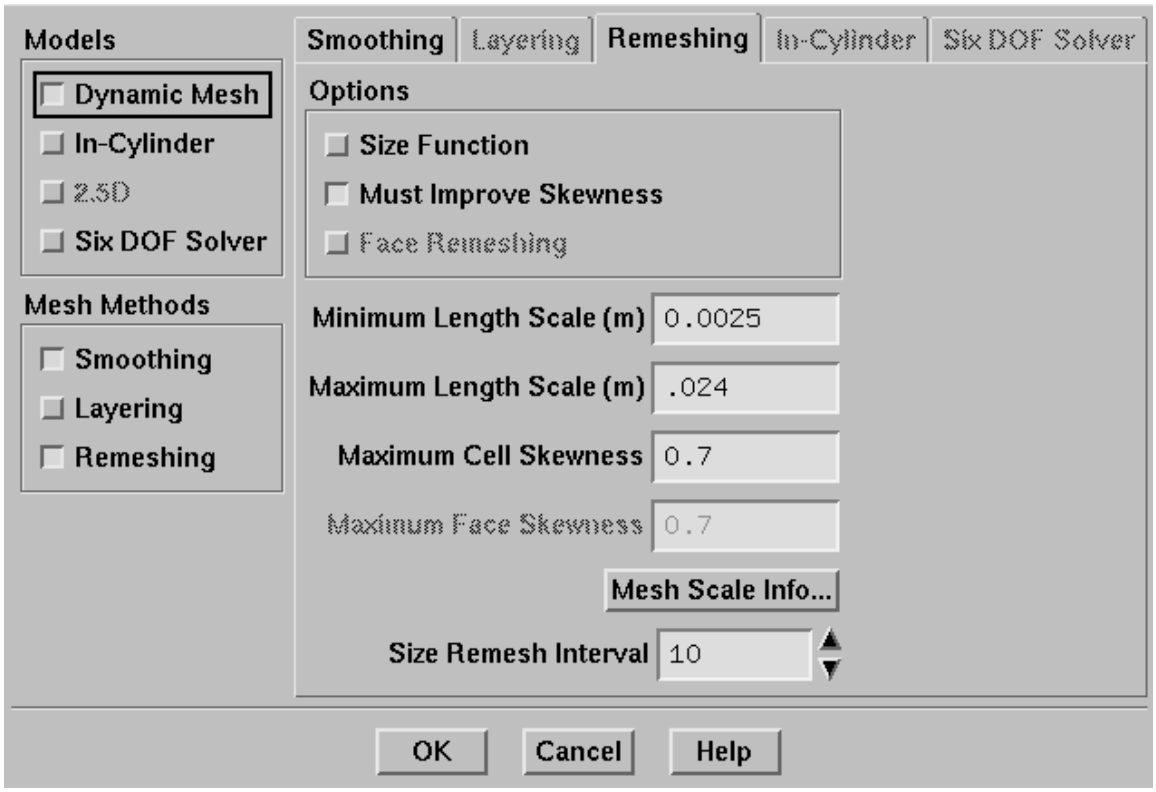

i. Click the Mesh Scale Info… tab to get the length scales of the grid.

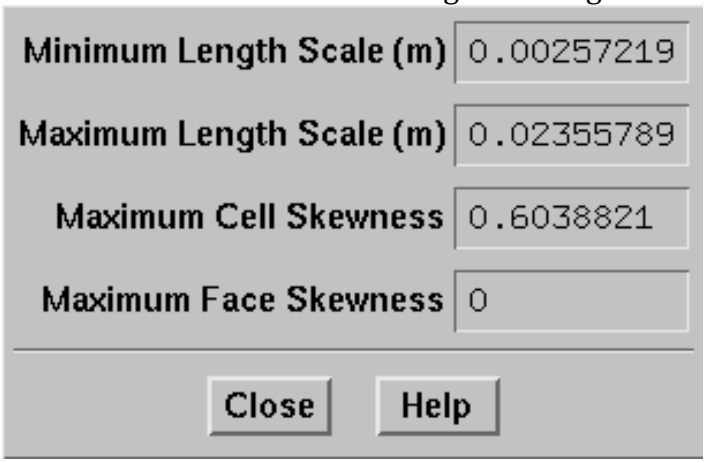

ii. Enter the values porvied from the Mesh Scale Info window.

c. Click **OK** to close the **Dynamic Mesh Parameters** panel.

3. Set up the moving zones.

Define → **Dynamic Mesh** → **Zones**…

a. Create the dynamic zone, Beam_rightside.

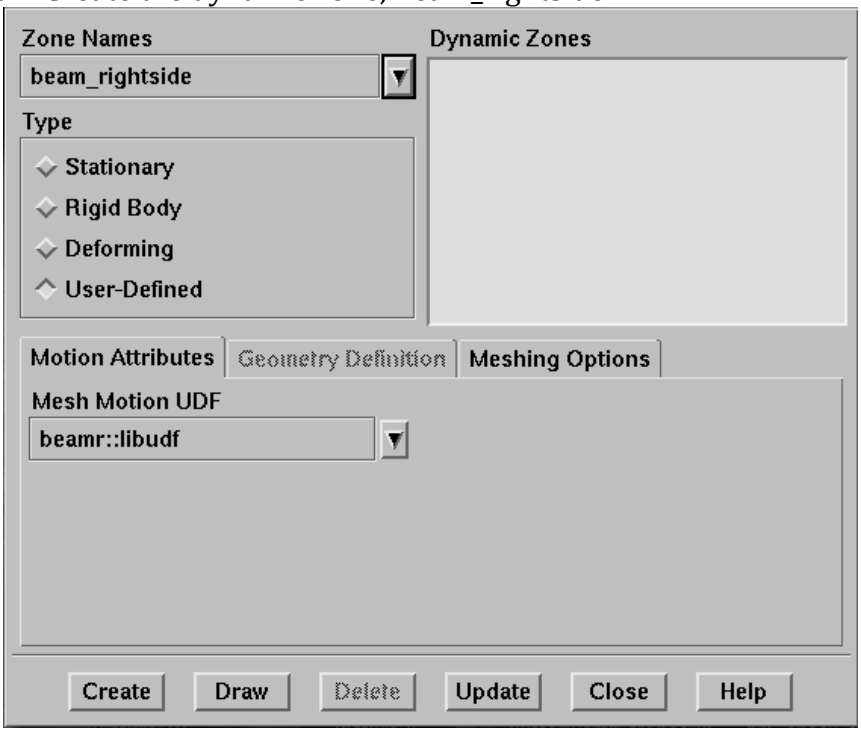

i. Select beam_rightside from the **Zone Names** drop-down list.
ii. Select **User-Defined** from the **Type** group box.
iii. In the **Motion Attributes** tab select beamr::libudf from the **Mesh Motion UDF** drop-down list.

The dynamic zone for the right side of the beam has been specified.

iv. In the **Meshing Options** tab set Cell Height to 0.004 and click create.

b. Similarly create the dynamic zone, Beam_leftside.
   i. Same process as previous zone except choose beaml::libudf in the **Motion Attributes** tab.

c. Create the dynamic zone, moving fluid.
   i. Select **deforming_domain** from the **Zone Names** drop-down list.
   ii. Select **Deforming** in the **Type** group box.

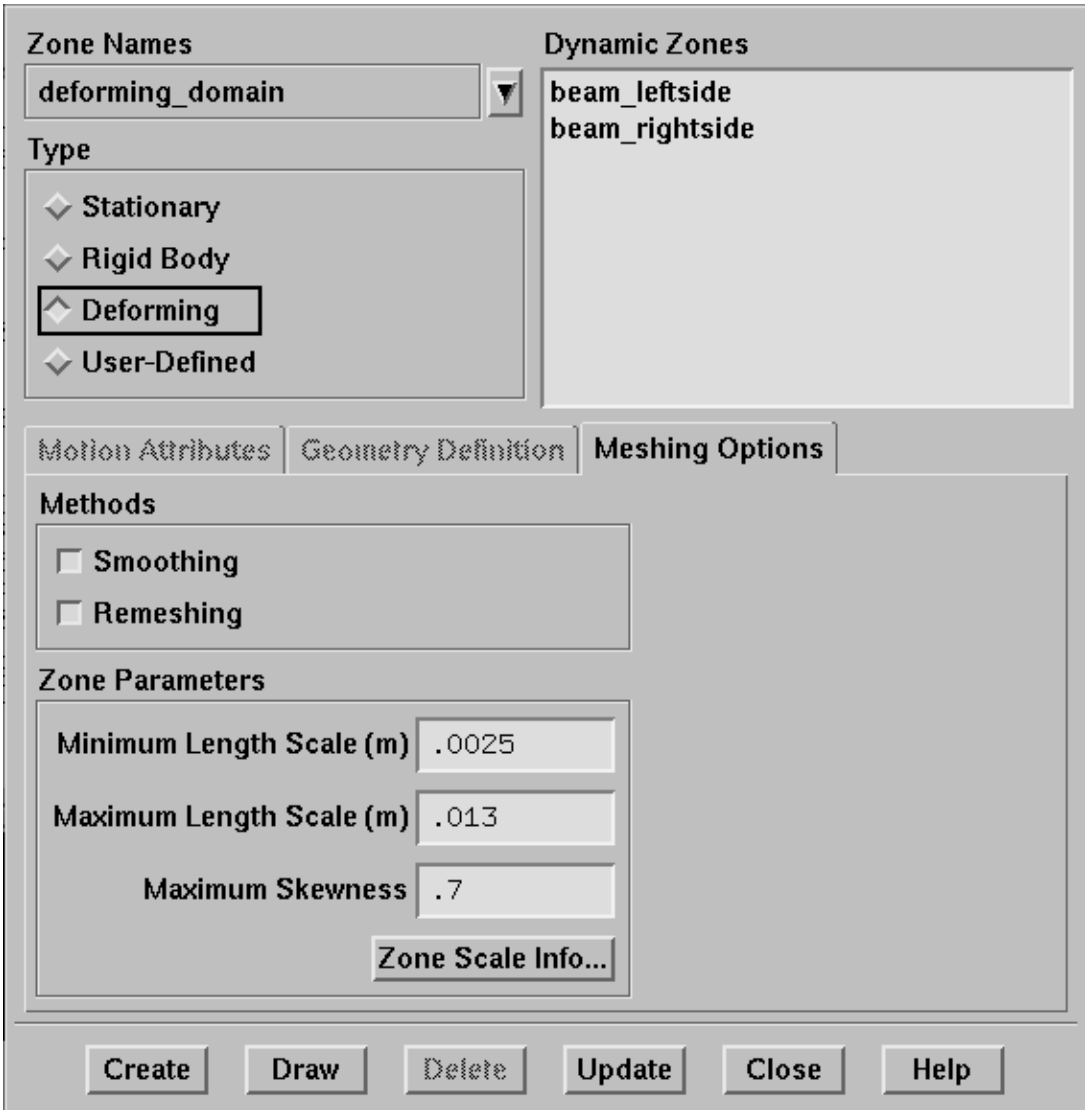

iii. Click the **Zone Scale Info** button to get zone information.

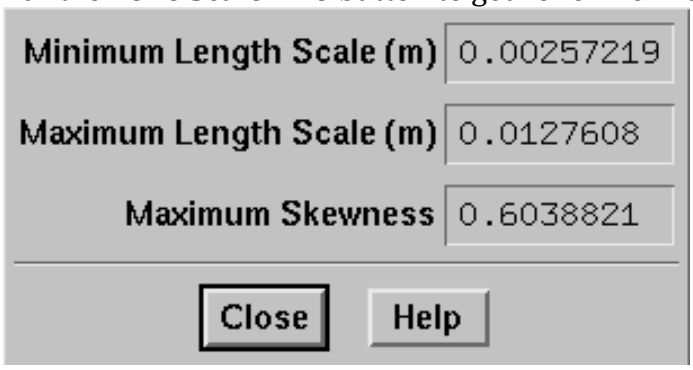

iv. Under **Zone parameters** enter the values obtained from the **Zone Scale** Window.
v. Click Create

d. Close the Dynamic Mesh Zones panel.

4. Hook UDF file to **FLUENT**

Define → **User-Defined** → **Function Hooks**…

a. Click **Edit** next to the **Execute at End Function Hook**.

i. Select Calculate_Force::libudf and Click **Add**.

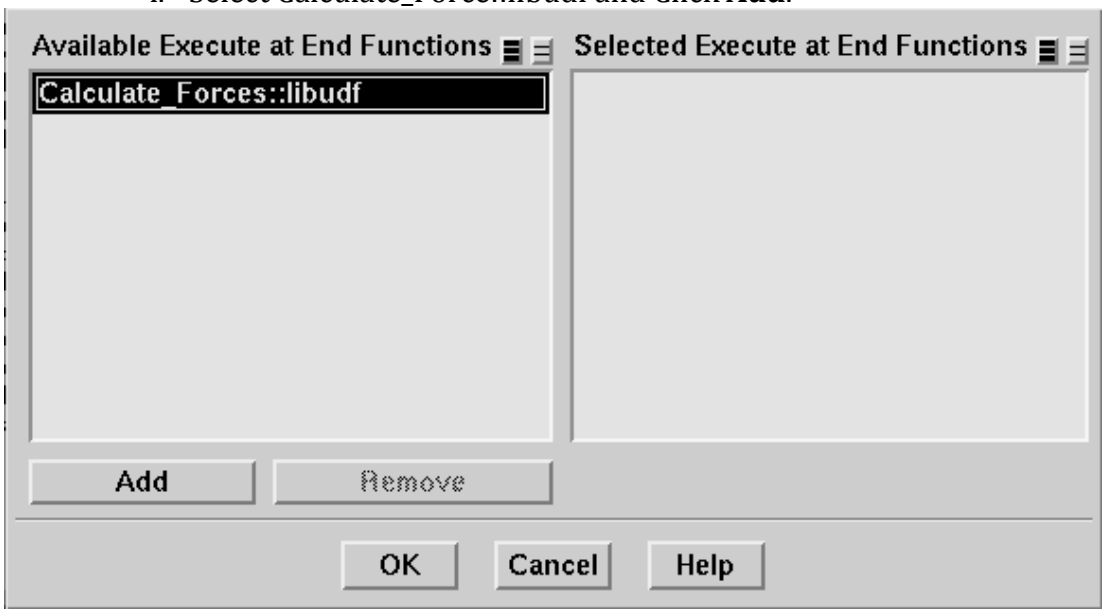

ii. Click **OK** to exit the **Execute at End Functions** panel.

b. Click **OK** to exit **User-Defined Function Hooks** panel.

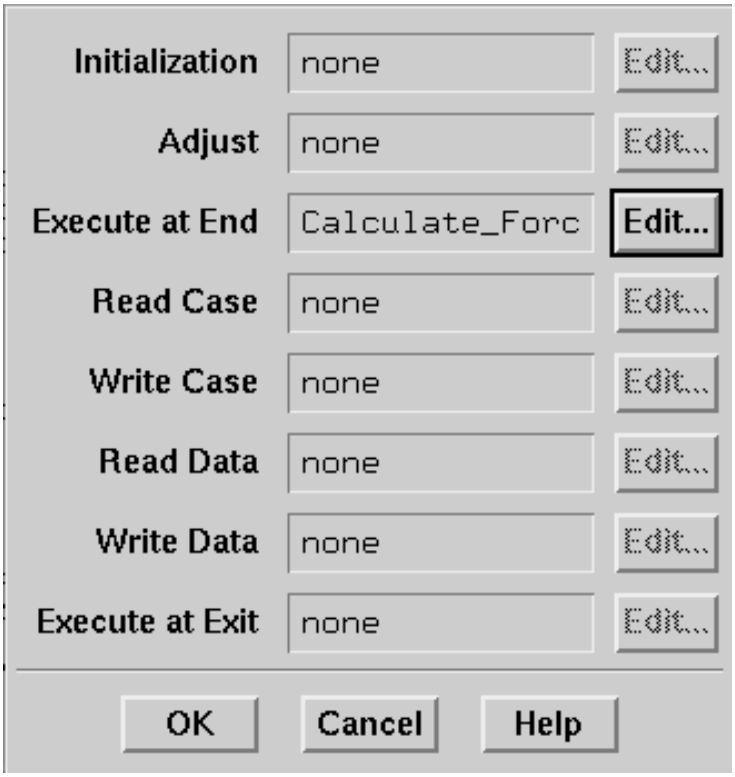
Initialization
none
Edit...
Adjust
none
Edit...
Execute at End
Calculate_Forc
Edit...
Read Case
none
Edit...
Write Case
none
Edit...
Read Data
none
Edit...
Write Data
none
Edit...
Execute at Exit
none
Edit...
OK
Cancel
Help

Step 7: Unsteady Model

1. Specify Unsteady Solver

Define → **Models** → **Solver…**

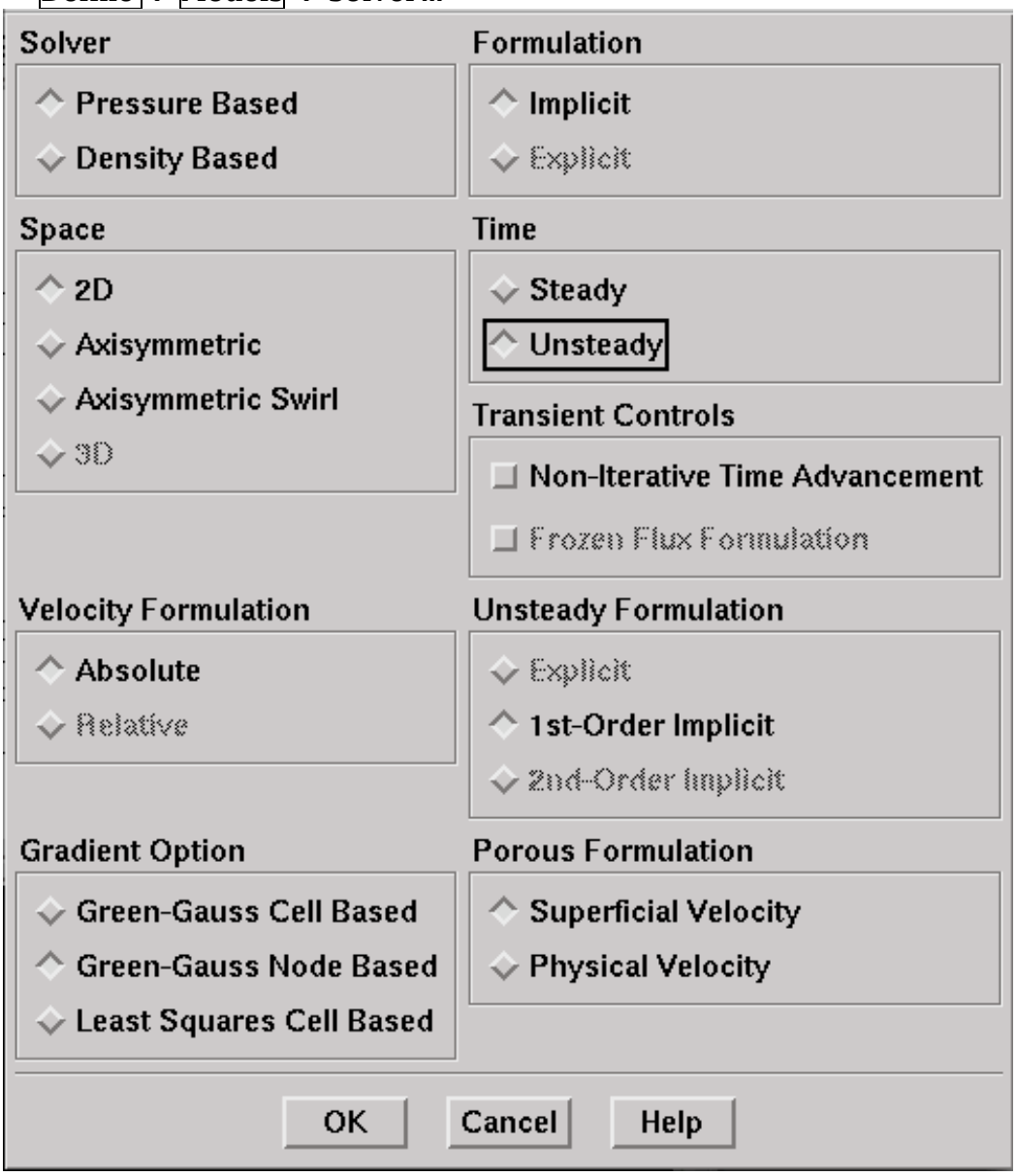

   a. Select **Unsteady Solver** from menu

REFERENCES

Auweter, H., Horn, D. & Lueddecke 1987 Fiber-optical doppler anemometer. *Tech. Rep.* U.S. patent no. 4637716. BASF Aktiengesellschaft, Germany.

Bobb, L., White, B., Davis, J. & Samouris, A. 1992 Optical ber sensor for measuring physical properties of uids. *Tech. Rep.* U.S. patent no. 5115127. The United States of America as represented by the Secretary of the Navy, Washington, DC.

Bruel, C. & Combe, H. 2005 Laser anemometer. *Tech. Rep.* U.S. patent no. 6847437. THALES, Paris, France.

Cauwenberghe, V. & Motycka, J. 1986 Force-balance drag anemometer. *Tech. Rep.* U.S. patent no. 4631958. Canadian Patents and Development Limited, Ottawa, CA.

Coleman, H. & Steele, W. 1989 *Experimentation and uncertainty analysis for engineers*. John Wiley and Sons.

Crane, R. & Fischer, E. 1991 Embedded ber optic beam displacement sensor. *Tech. Rep.* U.S. patent no. 5023845. The United States of America as represented by the Secretary of the Navy, Washington, DC.

DeLucia, M. & Manfrida, G. 1989 Development and experimental testing of a prototype miniature drag-force anemometer. *Fluids Measurements and Instrumentation Forum* **77**, 11–14.

Dyott, R. B. 1989 Fiber optic doppler anemometer. *Tech. Rep.* U.S. patent no. 4818071. Andrew Corporation, Orland, IL.

Fagan, J., Jr., J. S., Hassell, J., Mears, B., Beason, R., Wilkinson, S., Lear, T. & Tan, K. 1996 System for characterizing ow pattern, pressure and movement of a uid. *Tech. Rep.* U.S. patent no. 5488224. Gas Research Institute, Chicago, IL.

Fralick, G. 1980 Dynamic behavior of a beam drag-force anemometer. *Tech. Rep.* NASA TP 1687. National Aeronautics and Space Administration.

Hara, E. 1980 Clear air turbulence detector. *Tech. Rep.* U.S. patent no. 4195931. The United States of America as represented by the Secretary of the Army, Washington, DC.

Hartmann, K. & Siersch, W. 1980 Gas velocity meter. *Tech. Rep.* U.S. patent no. 4201467. Erwin Sick Gesellschaft mit beschrankter Haftung Optik-Elektronik, Waldkirch, Germany.

Hatton, A. & Plawsky, J. 1987 Fiber optic probe and system for particle size and velocity measurement. *Tech. Rep.* U.S. patent no. 4662749. Massachusetts Institute of Technology, Cambridge, MA.

Henderson, T. 1997 Fluid sensing apparatus with a rotatable member utilizing different length light pipes for alternately transmitting a light beam. *Tech. Rep.* U.S. patent no. 5638174. Xerox Corporation, Stamford, CT.

Ismailov, M. M. 2003 Flow meter. *Tech. Rep.* U.S. patent no. 6510842. Ismailov, Fernandiana Beach, FL.

Ismailov, M. M. 2005 Flow meter. *Tech. Rep.* U.S. patent no. 6874480. Combustion Dynamics Corp., New York, NY.

John, K. & Olldag, P. 1986 Laser-doppler-anemometer. *Tech. Rep.* U.S. patent no. 4575238. Disa Elektronik A/S, Skovlunde Denmark.

Kleinerman, M. 1991 Remote measurement of physical bariables with fiber optic systems. *Tech. Rep.* U.S. patent no. 5004913. Kleinerman, Southbridge, MA.

Krause, L. & Fralick, G. 1982 Miniature drag-force anemometer. *ISA Transactions* **21** (1), 37–44.

Metzger, M. 2002 Scalar dispersion in high Reynolds number turbulent boundary layers. PhD thesis, University of Utah, Salt Lake City, Utah.

Metzger, M. & King, C. 2010 Miniature opto-mechanical anemometer. *Tech. Rep.* U.S. patent no. 7742153. University of Utah Research Foundation, Salt Lake City, UT.

Phillips, S. R. 1986 Fiber optic thermal anemometer. *Tech. Rep.* U.S. patent no. 4621929. Luextron Corporation, Skovlunde Denmark.

Roshko, A. 1954 On the development of turbulent wakes from vortex streets. *Tech. Rep.* NACA Report 1191. National Advisory Committee for Aeronautics.

Schlichting, H. 1979 *Boundary Layer Theory*, 7th edn. New York, New York: McGraw-Hill.

Simundich, T. 1999 Laser-based forward scatter liquid ow meter. *Tech. Rep.* U.S. patent no. 5865871. Laser Metric, Inc., Villa Park, CA.

Small, J. 1992 Optoelectronic motion and uid ow sensor with resilient member deected by uid ow. *Tech. Rep.* U.S. patent no. 5120951. Hughes Aircraft Company, Los Angeles, CA.

Spalart, P. & Allmaras, S. 1992 A one-equation turbulence model for aerodynamic flows. *Tech. Rep.* AIAA Paper 92–0439. American Institute of Aeronautics and Astronautics.

Swope, J. 2009 Design of a miniature mechano-optical anemometer. Master's thesis, University of Utah, Salt Lake City, Utah.

Thomson, W. 1972 *Theory of Vibration with Applications*. Englewood Cliffs, NJ: Prentice-Hall, Inc.

Tjin, S. C. 2000 Fiber optic catheter for accurate ow measurements. *Tech. Rep.* U.S. patent no. 6166806. Tjin, Singapore.